Structural characteristics of the core region of T-PARC Typhoon Sinlaku in a vertically sheared environment

Strukturelle Merkmale der Kernregion des T-PARC Taifuns Sinlaku in vertikal gescherter Umgebung

Diplomarbeit im Fach Physik
vorgelegt von

Annette Förster

17. Oktober 2011

Referent: Univ.-Prof. Dr. Sarah Jones
Korreferent: Univ.-Prof. Dr. Klaus Dieter Beheng

Institut für Meteorologie und Klimaforschung
Karlsruher Institut für Technologie

Zusammenfassung

Die Struktur und Intensität tropischer Wirbelstürme wird von einer Vielzahl von Faktoren beeinflusst, zum Beispiel von der Meeresoberflächentemperatur, der Umgebungsströmung oder der Wechselwirkung mit anderen Wettersystemen. Die Umgebung eines tropischen Wirbelsturms wird umso komplexer je weiter er sich in Richtung der mittleren Breiten bewegt und somit ist auch die Vorhersage seiner Entwicklung zu diesem späten Zeitpunkt im Lebenszyklus sehr kompliziert. Ein wichtiger Ansatz um die Vorhersage zu verbessern ist deswegen ein versessertes Verständnis der physikalischen Prozesse, die die Struktur des Wirbelsturms beeinflussen.
Dieses verbesserte Verständnis war eines der Hauptziele der 2008 durchgeführten Messkampagne T-PARC (THORPEX Pacific Asian Regional Campaign), in deren Rahmen auch die Entwicklung von Taifun Sinlaku detailliert untersucht wurde. Um die physikalischen Mechanismen, die für die Entwicklung von Sinlaku maßgeblich waren, zu identifizieren, muss zuerst die Struktur des Taifun genau untersucht werden. Solch eine strukturelle Analyse wurde im Rahmen der vorliegenden Diplomarbeit durchgeführt. Der Zeitpunkt der Untersuchung konzentriert sich auf einen späten Zeitpunkt im Lebenszyklus von Sinlaku, als er den Einfluss der mittleren Breiten schon deutlich spürte. Entgegen der Erwartungen unterbrach Sinlaku seine außertropische Umwandlung und verstärkte sich kurzzeitig wieder bis auf Taifunstärke. Der Zeitpunkt der Untersuchung liegt kurz nach dieser Reintensivierungsphase und konzentriert sich auf die Kernregion des Taifuns. Die Untersuchung stützt sich hauptsächlich auf Radardaten, die von einem flugzeuggetragenen Doppler-Radar gemessen wurden. Ergänzt werden die Radardaten von Dropsondendaten, Messungen die auf Flughöhe durchgeführt wurden, Windgeschwindigkeiten, die anhand von Satellitenbildern berechnet wurden (sogenannte AMVs) und operationellen Analysen des Europäischen Zentrums für mittelfristige Wettervorhersage (EZMW). Dieser Datensatz ermöglicht einen einzigartigen Einblick in die Struktur der Kernregion eines Taifuns zu diesem Zeitpunkt nach der Reintensivierung. Es stellte allerdings auch eine sehr große Herausforderung dar, diesen Datensatz zu analysieren. Vor allem die starke Krümmung des Flugbahn des Flugzeuges, auf

dem das Doppler-Radar montiert war, erzeugte Schwierigkeiten bei der Auswertung, weil sie die Genauigkeit der Vertikalgeschwindigkeit drastisch reduzierte. Der gesamte Datensatz wurde mit Hilfe einer neuen Daten-Assimilations-Methode namens SAMURAI (Bell et al., 2012) auf ein kartesisches Gitter gebracht. Die resultierende Analyse zeigt, dass die Kernregion von Sinlaku eine sehr stark asymmetrische Struktur aufweist.

Im Nordosten der Eyewall befinden sich die höchsten Radarreflektivitätswerte und die Region ist von großflächigem Aufsteigen geprägt. Außerdem zeigt sich das typische Strömungsmuster eines Taifuns: bodennahes Einströmen der Luft, Aufsteigen im Gebiet der Eyewall und Ausströmen in größeren Höhen. Im Nordwesten finden sich zwar auch hohe Radarreflektivitäten wieder, aber das Strömungsmuster ist ein anderes. Im Bereich der Eyewall gibt es weiterhin Aufsteigen, aber diese aufsteigende Luft erzeugt in größeren Höhen kein signifikantes Ausströmen. Stattdessen sinkt ein großer Teil der Luft auf der dem Zentrum zugewandten Seite ab. Im Süden und Westen der Eyewall befinden sich größere Lücken in der Radarreflektivität. Um diese starken Asymmetrien erklären zu können, müssen zuerst einmal mögliche Mechanismen identifiziert werden. Eine Möglichkeit, die in vielen Studien untersucht wurde, ist die Wechselwirkung des tropischen Wirbelsturms mit einem Trog der mittleren Breiten, die in einer raschen Verstärkung des Wirbelsturms resultieren kann. Im vorliegenden Fall ist die Rolle der Umgebungsströmung allerdings darauf beschränkt, dass Sinlaku im Laufe der Zeit einer immer stärker werdenden vertikalen Scherung ausgesetzt ist. Eine direkte Wechselwirkung zwischen Sinlaku und der Umgebungsströmung wurde nicht beobachtet. Deshalb wird in dieser Arbeit vermutet, dass die Struktur von Sinlaku hauptsächlich durch die vertikale Scherung der Umgebungsströmung beeinflusst wird und aufgrund dessen wurde die Struktur des Taifuns besonders im Hinblick auf mögliche, durch die Scherung verursachte Merkmale untersucht.

Die Neigung des Sturms konnte anhand seines Wind- und seines Zirkulationszentrums bestimmt werden. Es stellte sich heraus, dass der Sturm zur Linken des Scherungsvektors geneigt war, wobei eine west-südwestliche Scherung vorherrschte. Dieses Ergebnis steht im Einklang mit bereits existierenden Studien. Die Radarreflektivität und die Vertikalgeschwindigkeit wurden mit Hilfe von so genannten CFADs (contoured frequency by altitude diagrams) untersucht. Es ergab sich, dass das Hauptaufsteigen in den scherungsabwärtigen Quadranten statt findet und dass Abwärtsbewegungen vor allem in den dazu entgegen gesetzten, scherungsaufwärtigen Quadranten zu finden sind. Die Gebiete mit der höchsten bodennahen Radarreflek-

tivitäten befinden sich in den Quadranten links des Scherungsvektors, was sich mit den Erwartungen deckt, dass sich die höchsten Radarreflektivitäten stromabwärts der höchsten Aufwärtsbewegungen befinden. Auch diese Ergebnisse decken sich mit bereits existierenden Beobachtungen und Modellstudien.
Die Dropsonden, die im Kerngebiet des Taifuns und in der näheren Umgebung abgeworfen wurden, legen nahe, dass Sinlaku mit der trockenen Luft, die ihn auf mittleren Höhen umgab, wechselwirkte. Diese trockene Luft könnte auf der westlichen Seite der Eyewall in die Zirkulation des Taifuns eingemischt worden sein und eventuell auch die Intensität des Taifuns geschwächt haben, indem sie die Konvektion in der südlichen Hälfte des Eyewall behinderte. Die Einmischung wurde eventuell durch die vertikale Scherung der Umgebungsströmung ermöglicht. Es kann also zurecht vermutet werden, dass die vertikale Scherung die Struktur von Sinlaku auf verschiedene Arten beeinflusst hat.
In dieser Arbeit konnten mögliche Mechanismen die für die Struktur von Sinlaku wichtig waren, identifiziert werden. Nachdem die Analyse allerdings nur für einen einzigen Zeitpunkt durchgeführt wurde, ist es schwierig die Bedeutung der einzelnen Mechanismen genauer zu bestimmen. Dafür wäre es interessant die Arbeit im Rahmen einer Modellstudie weiterzuführen. Ein solcher Ansatz könnte genaueren Aufschluss darüber geben, welche physikalischen Mechanismen eine Rolle spielen und eventuell auch die Sensitivität der Struktur auf einzelne Merkmale der Umgebung untersuchen.

Contents

1 Introduction

Forecasting the track and intensity of a tropical cyclone correctly remains a challenging task, but is very important because tropical cyclones pose a large thread to both life and property. The sooner the track and intensity can be established, the longer there is time to warn the public and thus take steps in order to be prepared for the arrival of the cyclone.

A prerequisite for improving forecasts is a detailed understanding of the physical processes that affect the development of the tropical cyclone's structure and its interaction with the environment. In order to gain insights into the acting physical mechanisms, different paths can be followed. On the one hand, the behavior of tropical cyclones can be examined in model studies. The huge advantage of this approach is that the initial conditions can be set deliberately and thus the response to certain conditions can be investigated. Moreover, the possibility to change the initial conditions slightly provides valuable information about the sensitivity of the results to different parameters. However, all conclusions that are drawn on the basis of model results, are limited by the extent to which the model provides an accurate representation of the real situation. On the other hand, observations of tropical cyclones can be gathered in order to test the hypotheses that evolve from the model studies.

Such a field campaign took place in the Western Pacific in 2008, called T-PARC (THORPEX Pacific Asian Regional Campaign). One of its goals was to improve the understanding of the processes involved in the extratropical transition of tropical cyclones. This is especially challenging, because an extratropical transition describes the process of a tropical cyclone moving toward the midlatitudes and along the way encountering substantial changes in its environment. Many of the environmental features can drastically change the development of the tropical cyclone and thus forecasting the track and intensity at this time of the life cycle of a tropical cyclone is very difficult.

The first step to understanding the physical mechanisms is to analyze the structure of the tropical cyclone in detail. Thus in this study, one of the tropical cyclones

occurring during T-PARC, Typhoon Sinlaku, is examined in the later stage of its life cycle.

The presented analysis is mostly based on radar data collected during a flight into the cyclone, supplemented by dropsonde, flight level and satellite data. To obtain a gridded analysis, a new 3D variational data assimilation technique was applied. The resulting analysis provides a very detailed insight into the structure of the eyewall with a horizontal resolution of up to 1 km and a vertical resolution of 500 m.

The thesis is organized as follows. First, the theoretical background needed for the interpretation of the results is established. Then the environment that Sinlaku is embedded in, is investigated to identify factors, that could potentially affect the structure of the tropical cyclone. After that a detailed analysis of the core region of Sinlaku, based on data that were collected during the flight into the system is carried out and, finally, the influence of vertical shear on the structure of Sinlaku is examined.

2 Theoretical background

2.1 Tropical cyclones

Tropical cyclones are warm-core, non-frontal synoptic-scale cyclones, originating over tropical or subtropical waters, with organized deep convection and closed surface wind circulation about a well defined center. (WMO, 2005). Depending on the ocean basin they occur in, severe tropical cyclones have different local names. In the North Atlantic and eastern North Pacific ocean basins they are called hurricanes, in the western North Pacific Ocean typhoons and in the South Pacific and Indian Oceans cyclones. In contrast to midlatitude cyclones whose primary energy source is associated with a horizontal temperature gradient, the primary energy source for tropical cyclones is provided by fluxes of sensible and latent heat from the ocean. As stated in Gray (1968), there a several precursor environmental conditions that are necessary but not sufficient for tropical cyclone formation:

- ocean temperatures exceeding 26°C throughout a depth of about 50 meters
- formation at low latitudes between around 5° to 20°
- pre-existing near-surface disturbance
- low values of vertical wind shear
- midlatitude humidity

The high ocean temperature is needed to supply energy to the air above, that later is released in the eyewall. The formation typically takes place at latitudes between 5° and 20° and not in the vicinity of the equator, because the planetary rotation is needed to generate low level relative vorticity. The pre-existing low-level disturbance is necessary to develop an organized system with low-level inflow. And since vertical wind shear is defined as the magnitude of wind change with height, too high values hinder or destroy the formation of a tropical cyclone. The midlevels must be relatively moist in order to allow for continuing development of deep convection.

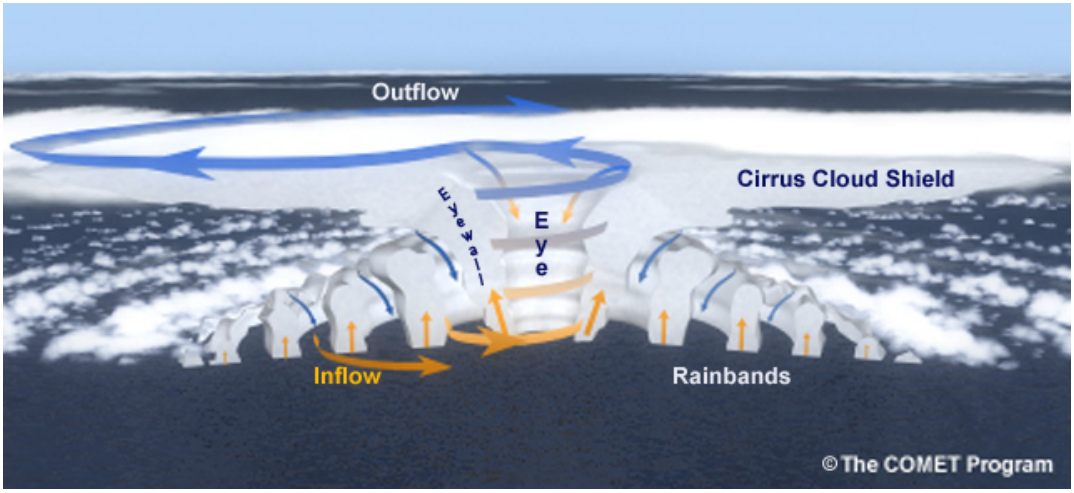

Figure 2.1: Schematics of a hurricane, arrows indicating the air motion and white areas representing the different cloud structures. From MetEd, operated by The COMET Program (2011).

In Fig. 2.1 the main structural features of a mature tropical cyclone are illustrated schematically. It has a dominant primary axissymmetric circulation, on which a weaker secondary circulation is superimposed. This secondary circulation consists of inflow in the boundary layer, upward motion in the eyewall and the spiral bands and outflow in a thin layer beneath the tropopause. Surface friction and latent heat release are responsible for this secondary circulation (Chan and Kepert, 2010). The eyewall is a region of deep convection, heavy precipitation and strong winds, sloping outwards as it rises. In contrast the eye, that on average spans a diameter of 20 to 50 km, has only light winds and subsiding air suppresses clouds and results in a warm core (Laing and Evans, 2010).

Apart from these features that are inherent to all tropical cyclones, tropical cyclones appear in a large variety of size and intensity. The size of a tropical cyclone can be classified by the radius within which the gale force winds exceed 15 m s^{-1}. Using this definition the largest tropical cyclone on record was Typhoon Tip (1979) with a radius of 1100 km and the smallest tropical cyclone was Tropical Storm Marco (2008) with a radius of 19 km (NOAA Hurricane Research Division, 2009). According to the World Meteorological Organization (WMO) the intensity of a tropical cyclone is classified by the 10-min averaged mean of the maximum sustained wind. The detailed values can be seen in table 2.1. Note that the averaging time span is different in different parts of the world and that measuring the wind in a tropical

cyclone is often not practicable and thus replaced by values, which are retrieved indirectly from satellite data.

As stated above, tropical cyclones have wind speeds of at least 33 m s^{-1} (or 119 km h^{-1}) and regions of deep convection accompanied with heavy precipitation. It is obvious that such a system hitting land, poses a serious thread to both life and property. Torrential rainfall can cause landslides and floods, storm surges can flood coastal regions and high wind speeds can disroot trees, devastate houses, cars and everything else, that is in the way.

Table 2.1: Tropical cyclone intensity

International Category	Max. sustained wind [m s^{-1}]
Tropical Depression	< 17
Tropical Storm	18 - 32
Severe Tropical Storm	> 33

2.2 Influence of shear

Shear has long been recognized as an important factor influencing the tropical cyclone's structure and intensity (e.g. Emanuel et al. (2004)), but the exact response depends on the individual characteristics of the storm. The influence of shear on the vertical structure of a tropical cyclone has been studied intensively both in dry (Jones (1995, 2000)) and moist (e.g. Frank and Ritchie (1999, 2001)) model studies. In the dry case and if the shear is not too strong, the shear will induce an initial tilt roughly in the direction of the shear that will precess with time (Jones, 1995). In case that moist processes are included in the simulations, the tilt develops to be at near-equilibrium to the downshear-left side and no precession is found to occur (Chan and Kepert, 2010). In observational studies, it was found that there is often a time lag between the onset of shear and the development of the tilt, depending amongst other things on the shear strength. If the shear is too large, the tropical cyclone is not able to maintain its strength. A value of 8-10 m s^{-1} of 850-200 hPa shear is considered to be the threshold for weakening to occur (Gallina and Velden, 2002).

In order to balance the horizontal wind field of a tilted vortex, the vertical velocity needs an additional asymmetric component. Model studies with dry dynamics

showed that the isentropes have to be perturbed upwards on the down-tilt side and thus maximum ascent takes place to the right of the tilt vector. IIn "full physics" simulations the maximum updrafts were located in the downshear-left quadrant and the rainfall maxima slightly downstream because of the horizontal cyclonic advection that is imposed on the falling precipitation (Wang and Holland (1996), Frank and Ritchie (1999, 2001)). Thus, despite the fact that there is no consensus about the exact location of the maximum updrafts, it is clear that the shear introduces asymmetries to both the vertical motion and the rainfall pattern around the eyewall. Shear can also favor the interaction of the vortex with environmental air. In general, an intense tropical cyclone is well protected from the intrusion of environmental air. It is possible that dry air wraps all around a developing tropical cyclone without affecting storm intensity at all when no shear is present. However, the weaker the storm and the higher the vertical shear, the more likely it is that an intrusion of environmental air into the storm's circulation can occur (Riemer and Montgomery, 2011). If the intruded air is dry this can have detrimental effects on the storm's intensity, because the dry air may enhance downdrafts, thus cooling and drying the boundary layer, hindering the eyewall convection and thus weaken the storm.
Hence, shear plays an important role in shaping the structure of tropical cyclones and affects them in many different ways.

2.3 Extratropical transition

Extratropical transition is the process of a tropical cyclone moving poleward and eventually reaching the midlatitudes. Based on Klein et al. (2000), this transition can be classified into two stages: the transformation stage and the extratropical stage. The transformation stage describes the response of the tropical cyclone to changes in its environment. The subsequent extratropical stage is defined as the stage, where the tropical cyclone exhibits extratropical characteristics such as frontal zones and possibly interacts with pre-existing extratropical systems.
The changes in the environment that lead to the onset of the transformation stage are due to the poleward movement of the tropical cyclone. This movement goes along with various changes in the environment of the cyclone such as increased baroclinicity and vertical shear, decreasing sea surface temperature and increased sea surface gradients, meridional humidity gradients and an increased Coriolis parameter. The cyclone responds to these changes with asymmetries in wind, thermal

structure, moisture field, convection, precipitation and surface fluxes, eventually loosing its warm core and decreasing its intensity. Because the environmental flow largely determines the forward motion of the cyclone, the motion of the cyclone into the midlatitude westerlies results in an increased translation speed (Jones et al., 2003). Less than half of the tropical cyclones undergo ET, with the chance of ET being highest when the regions that are favorable for tropical development and extratropical development are close. For the Atlantic this is the case in September and October (Hart and Evans, 2001). Usually ET results in a weakening of the cyclone. But when interacting with an extratropical system in the extratropical stage, the cyclone can re-intensify rapidly as an extratropical system. This re-intensification is very sensitive to the relative position of the tropical cyclone relative to midlatitude trough-ridge pattern (Klein et al. (2002), Ritchie and Elsberry (2007)). Moreover the physical processes determining extratropical transition are not fully understood. Thus, to properly forecast both the position and the intensity of a cyclone during ET poses a big challenge to forecasters (Jones et al., 2003). Improving the forecast skill is very important because cyclones do not only have a direct impact but also a so called downstream impact. This means they can modify the trough-ridge pattern of the midlatitudes, for example by amplifying an existing ridge directly downstream of ET (Bosart and Lackmann, 1995) and subsequently strengthen the trough downstream of that ridge. Hence, even if tropical cyclones don't affect Europe directly, their remnants along with the resulting modification of the midlatitude flow can lead to high impact weather and large forecast errors (Anwender et al., 2008, Harr et al., 2008).

2.4 Radar

The results shown in later chapters are obtained by using a data set of various different data sources. However, the main source is airborne radar data. To be able to interpret the results thoroughly, the basics of radar meteorology are presented in this section, following Sauvageot (1992) and Handwerker and Beheng (2010). The word radar is an acronym for "**ra**dio **d**etection **a**nd **r**anging", implying that it is a remote sensing technique for detecting distant objects via radio waves. More precisely the distance and various other information about the object are assessed by emitting a radar signal and detecting and analyzing the fraction of the signal that is reflected back in the direction of the radar.

The radar signal must be designed according to the information, that should be obtained. The most important parameters are:

- the directional radio pattern of the antenna
- the frequency
- the pulse repetition time (PRT)
- and the polarization.

First of all, it is important that the antenna has a good directive radiation pattern, i.e. that the radar beam is narrow, in order to get a high spatial resolution. The area that is covered by the beam and thus the spatial resolution is a function of the distance from the antenna. For example, a beam width of 1° covers a circle of approximately 200 meters in diameter at a distance of 10 km whereas in a distance of 60 km it has already a diameter of 1000 meters. Moreover, it is favorable that as much of the power P_t that is emitted by the antenna as possible is actually used for the measurement thus a directed radiation is beneficial. The intensity S_i at the location of the scattering object is given by the following equation:

$$S_i(R, \theta, \varphi) = \frac{P_t}{4\pi \cdot R^2} \cdot D(\theta, \varphi) \tag{2.1}$$

where the object is assumed to be located at a distance R and at azimuthal and elevation angles of θ, φ from the antenna and $D(\theta, \varphi)$ is a function representing the directive radiation pattern.
A typical directive radiation pattern can be seen in Fig. 2.2. It shows that most of the intensity is the main lobe, but a minimal fraction is located in the side lobes also. Even though the intensity in the side lobes is suppressed by a factor of 1000 with respect to the main lobe's intensity, it can lead to misguiding signals. If the detected signal is a reflection from the signal of the side lobe instead of the main lobe, a reflecting object would be expected in the direction of the main lobe but instead it is located in the direction of the side lobe.
Secondly, the frequency of the radar signal must be chosen according to the particle size that should be detected. To explain this link, the relationship between the intensity of the reflected signal and the properties of the reflecting object has to be elucidated. In order to be able to follow an analytic approach, the scattering object

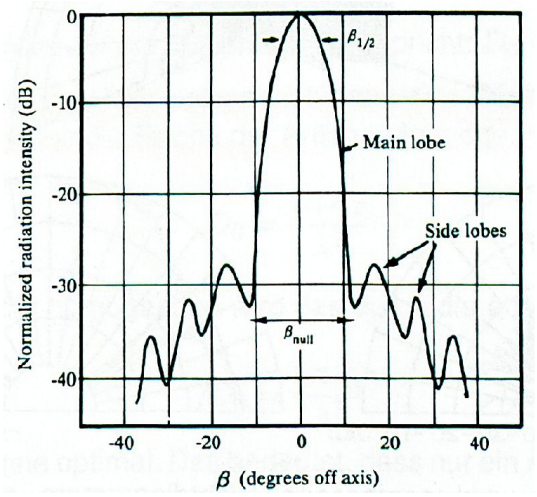

Figure 2.2: Rectangular radiation pattern showing the radiation intensity for different beam angles. From Sauvageot (1992).

is assumed to be homogeneous and spherical with radius r. The power P_s that is scattered by this object is:

$$P_s = S_i \cdot \oint \frac{\sigma_s(\theta, \varphi)}{4\pi} d\Omega \tag{2.2}$$

where S_i is the incident intensity of radiation at the position of the scattering object, $\sigma_s(\theta, \varphi)$ the differential scattering cross section as a function of the angles θ and φ, and Ω the solid angle. Assuming that the position of the receiver is identical with the position of the antenna, only the intensity that is scattered backwards (angle of π), will be detected:

$$S_s(R, \theta, \pi) = \frac{S_i}{4\pi \cdot R^2} \sigma_s(\pi) \tag{2.3}$$

Thus the scattered signal is a function of the emitted power, the radiation pattern, the distance between antenna and object and the differential scattering cross section. The differential scattering cross section in turn is a function of the object's size, the complex refraction index m and the antenna frequency. The exact formula was first given by Gustav Mie in 1908:

$$\sigma_s(\pi) = \frac{\lambda^2}{4\pi} \left| \sum_{n=1}^{\infty} (-1)^n)(2n+1)(a_n - b_n) \right|^2 \tag{2.4}$$

where the Bessel functions a_n and b_n depend on m and r. This rather complicated relationship can be simplified by the so called Rayleigh approximation in case that the radius of the scattered object is small in comparison to the wavelength ($r \ll \lambda$):

$$\sigma_s(\pi) = \frac{64 \cdot \pi^5}{\lambda^4} |K|^2 r^6 \tag{2.5}$$

where $|K|^2$ is the dielectricity factor:

$$|K|^2 = \left| \frac{m^2 - 1}{m^2 + 2} \right|^2 \tag{2.6}$$

Since the complex refraction index m of ice and water is different, the dielectricity factor differs also. In Sauvageot (1992) $|K|^2$ is given as 0.91 to 0.93 for water and 0.18 for ice. Thus snow reflects about five times less that rain. This is the main reason for the so called bright band, which is a region of higher reflectivities located just below the zero-degree level and thus the region where falling ice particles melt. The melting of the ice particles starts from the surface, so the particles are still large in size, but the reflectivity is determined by the coating of liquid water. When melted completely the reflectivity decreases again, because a raindrop is smaller in size than an ice particle with the same amount of water (Fig. 2.3). In stratiform rain the bright band can be seen clearly. In convective regions the band structure is not that distinct because of the turbulent wind regime. For a precipitation radar, there is not only one scattering object, but many different sized rain drops. Assuming that the particles are randomly positioned, the total differential scattering cross section η is the integral over all different diameters $D = 2r$ of particles:

$$\eta = \int_0^\infty \sigma_s(\pi, D)\ n(D)\ dD = \frac{\pi^5}{\lambda^4} \cdot |K|^2 \cdot Z \tag{2.7}$$

with the radar reflectivity factor

$$Z = \int_0^\infty D^6\ n(D)\ dD. \tag{2.8}$$

where $n(D)$ is the quantity density distribution.
In order to achieve a low signal to noise ratio, the frequency should be chosen to get an intensely reflected signal. Equation 2.7 shows that the larger the frequency (the smaller the wavelength), the bigger the scattering cross section η. On the other hand the wavelength must be large in comparison to the size of the particles that

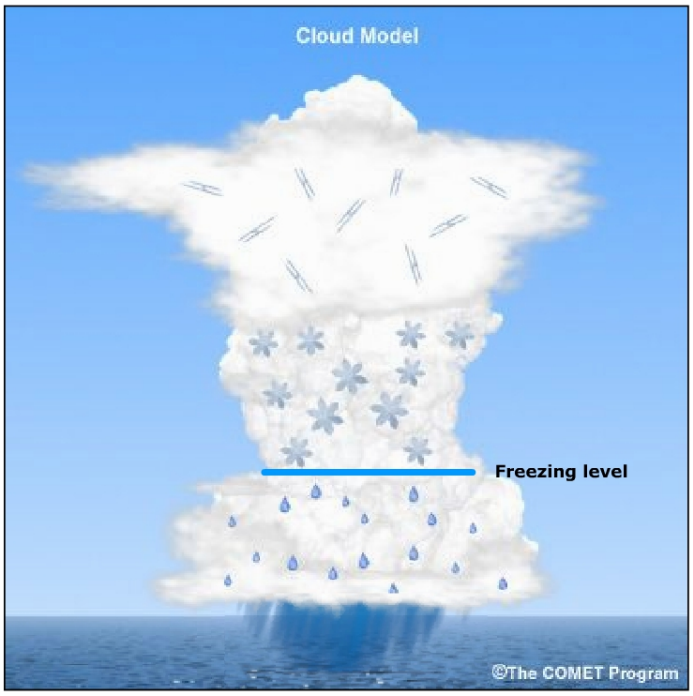

Figure 2.3: Schematics of a precipitating cloud. Ice particles in various shapes above the freezing level and raindrops below. From MetEd, operated by The COMET Program (2011).

should be detected, so that the Rayleigh approximation holds. Following these two limitations rain radars typically use frequencies between 2 and 8 GHz.
Note that the scattering cross section is proportional to the sixth power of the radius of the scattering object. Thus, bigger raindrops contribute much more to the absolute value of reflectivity than smaller ones.
Further information that can be gained analyzing the frequency of the detected signal using the Doppler shift is the speed of the detected object. Note that only the radial component of the velocity can be measured and thus additional radars with different vantage points are needed to calculate a three dimensional wind field.

Thirdly, the pulse repetition time determines the maximum unambiguous distance, that can be measured. The time between two pulses is τ, and since the signal propagates with the speed of light, c, the maximum unambiguous distance d_{max} is:

$$d_{max} = \frac{1}{2} \cdot c \cdot \tau \tag{2.9}$$

The factor $\frac{1}{2}$ is due to the fact that the signal travels the distance twice, to the scattering object and back to the detector. In order for the radar to have a large range, it would be favorable to have a long pulse length. But this is in opposition to the fact that an exact measurement of the velocity needs a high pulse repetition time. Hence, the choice of the pulse repetition time is a compromise between velocity and range, which is also known as the "Doppler dilemma". One of the resulting problems are the so called "second trip echos". They occur because the detector receives a signal that was reflected in a distance larger that the maximum unambiguous distance and thus will be assigned to the most recently sent signal, despite the fact that it is actually a reflection of the previous signal.

Lastly, the polarization can shed light on the shape of the particles. When the signal is polarized vertically, the scattering object will be excited to oscillate in the vertical as well, and so the detected signal contains only information about the vertical extent of the scattering object. Analogously, when the signal is polarized horizontally the detected signal contains information about the horizontal extent of the scattering object only. The fraction of the horizontally and the vertically polarized signal thus reveals amongst other things whether the object is spherical or not.

In conclusion, there is a lot of information that can be gained from radar data, but it is important to be aware of the limitations as well. In addition to side lobes and second trip echos there are several other problems that have to be taken care of. A major one is ground clutter. It makes measurements near the surface difficult because as soon as the radar beam hits the ground, even if only partially, the reflection becomes very large and thus masks the information about scattering objects such as raindrops near the surface. Moreover, it is very difficult to estimate the rain rate based on the measured reflectivity pattern, because the size distribution of the rain drops and their state of aggregation are unknown and the relationship between reflectivity and drop size is non-linear. Thus, errors of the estimated rain rate in the range of 200 or 300 % are not unusual. Another aspect that has to be taken into account is the attenuation of the signal because of absorption and scattering by both atmospheric gases and rain drops/droplets. This is the reason why cloud radars preferentially use frequencies that are close to 35 GHz or 95 GHz, because at these frequencies there are so called "windows of attenuation" for the atmospheric gases.
In general, the radar reflectivity factor Z is referred to as "reflectivity". The range of

the values is very large, so a logarithmic scale is used. Moreover, the value relative to the norm reflectivity $Z_0 = 1\frac{mm^6}{m^3}$ is used rather than the absolute value. Thus the reflectivity is given by:

$$\zeta = 10\ dBz \cdot log_{10}\left(\frac{Z}{Z_0}\right) \tag{2.10}$$

Typical values for Z and ζ are given in Tab. 2.2:

Table 2.2: typical values

	Z $[\frac{mm^6}{m^3}]$	ζ [dBz]
non-precipitating clouds	10^{-3}	-30
very light rain	1	0
moderate rain	10^3	30
intense thunder storm with hail	$5 \cdot 10^7$	77

2.5 ELDORA

The radar data, that will be analyzed later, come from an airborne dual Doppler radar, named ELDORA (**El**ectra **Do**ppler **Ra**dar). It was developed jointly by the National Center for Atmospheric Research (NCAR) and the Centre de Recherches en Physique de L'Environement Terrestre et Planetaire (CRPE) and is mounted on the tail of a Lockheed P-3 aircraft, which is operated by the Naval Research Laboratory (NCAR Earth Observing Laboratory, 2010). It was specifically designed to observe atmospheric mesoscale convective systems at high spatial and temporal resolution. Technical details are displayed in Tab. 2.3.

ELDORA consists of two radars, which scan at an angle of ± 18.5 ° forward and backward of a plane normal to the aircraft's axis (see Fig. 2.4(a)). This scanning pattern allows for every point in the atmosphere to be scanned from two different vantage points (see Fig. 2.4(b)). As mentioned in section 2.4, this is necessary to calculate the wind field.

Despite the major advantage of being able to examine systems that are too remote for ground-based observations, there are several disadvantages associated with using an airborne radar.

First of all, the radar must be light and small to minimize the impact on the aircraft's endurance and payload. Secondly, the measurement has a much larger number of

Table 2.3: ELDORA radar characteristics. From Hildebrand et al. (1996).

characteristic	ELDORA
number of radars	2 (fore/aft)
transmit frequency [GHz]	9.2 - 9.8
beamwidth [°]	1.8
beam tilt angle [°]	± 15 - 19
sidelobes [dB]	- 35
polarization	horizontal
pulse repetition frequency [s^{-1}]	2000 - 5000
unambiguous range [km]	20 - 90
unambiguous velocity [m s^{-1}]	13 - 20
max. range resolution [m]	150

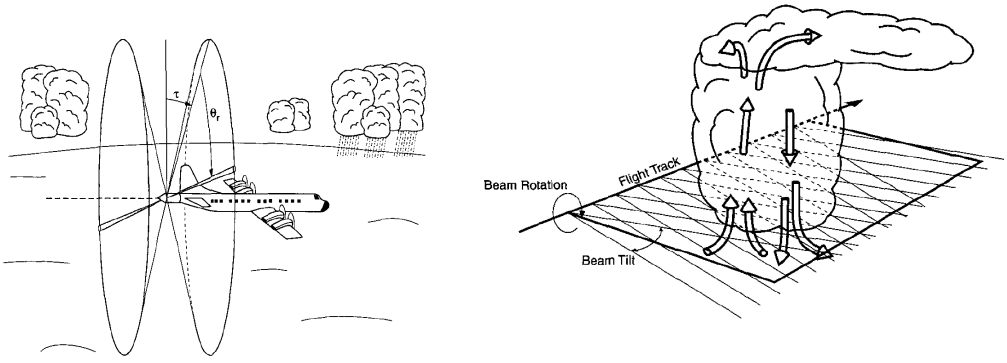

(a) (b)

Figure 2.4: (a) Schematics of the ELDORA scan technique showing the dual radar beams, tilted fore and aft of the plane of a plane normal to the fuselage. The antennas and radome rotate as a unit about an axis parallel to the longitudinal axis of the aircraft. (b) Schematics of the sampling of a storm complex by the ELDORA airborne dual-Doppler radar. The flight track past a hypothetical storm is shown. Data are taken from the fore and aft beams to form an analysis of the velocity and radar reflectivity field on the planes through the storm. From Hildebrand et al. (1996).

degrees of freedom than a ground based radar observation, such as the altitude of the aircraft, the speed of the aircraft, the pitch, the drift and the roll of the aircraft. All these variables have to be measured additionally in order to be able to assign the measured reflectivity and velocity values to the right location with the right magnitudes. Of course, these measurements are afflicted by errors and in order to

minimize those, navigation corrections, developed by Testud et al. (1995) and Bosart et al. (2002), are applied to the measured data set.
An error in the drift angle (angle between the aircraft track and the heading), for example, results in an asymmetric residual surface velocity pattern (see Fig. 2.5). In the plotted example the measurements would indicate that the surface left of the aircraft moves in a direction towards the aircraft and the surface on the right of the aircraft moves in a direction away from the aircraft. This mostly likely does not represent the reality, but points to an error in the measured angle. As for the drift angle, there exist typical residual velocity patterns for all additional degrees of freedom, from which the measurement error can be identified. In Bosart et al. (2002) these sources of errors are examined in detail and the Bosart-Lee-Wakimoto method to determine these errors is introduced. The method compares statistically the flight-level dual-Doppler winds and the in situ winds, measured with sensors, installed at the exterior of the aircraft. This allows corrections to be deduced for the parameters that are likely to contain the largest errors, namely the tilt, drift and ground speed. The along-track component of the dual-Doppler winds is affected mainly by the ground speed and tilt, whereas the cross-track component is affected by the drift. These parameters have to be adjusted, so that the difference between flight-level dual-Doppler winds and in situ winds is minimized. To rule out other effects, the method is best applied to a stratiform, straight and altitude-constant leg of the flight track.

Another fact, that has to be kept in mind, is that the uncertainty in the calculation of the vertical velocity depends strongly on the angle between the beams of the different vantage points (Hildebrand et al., 1996). Their Fig. 4 shows that the uncertainty for angles above 40° is fairly constant, but increases drastically for smaller angles. For example an angle of 20° results in an uncertainty in vertical velocity twice as high as for 40° just because of geometrical considerations. As can be seen in Fig. 2.4(b), this angle corresponds to twice the beam tilt angle for a straight flight pattern. However, if the aircraft's track is curved, the beams fan out at the outer part and the angle between the beams gets smaller and thus the uncertainty in the vertical velocity increases. Thus data from curved parts of the flight track are afflicted by larger errors than are straight legs.

The ELDORA antenna completes a 360° turn about every 3 seconds. The raw data of each sweep are stored in a separate file, containing variables such as radar reflec-

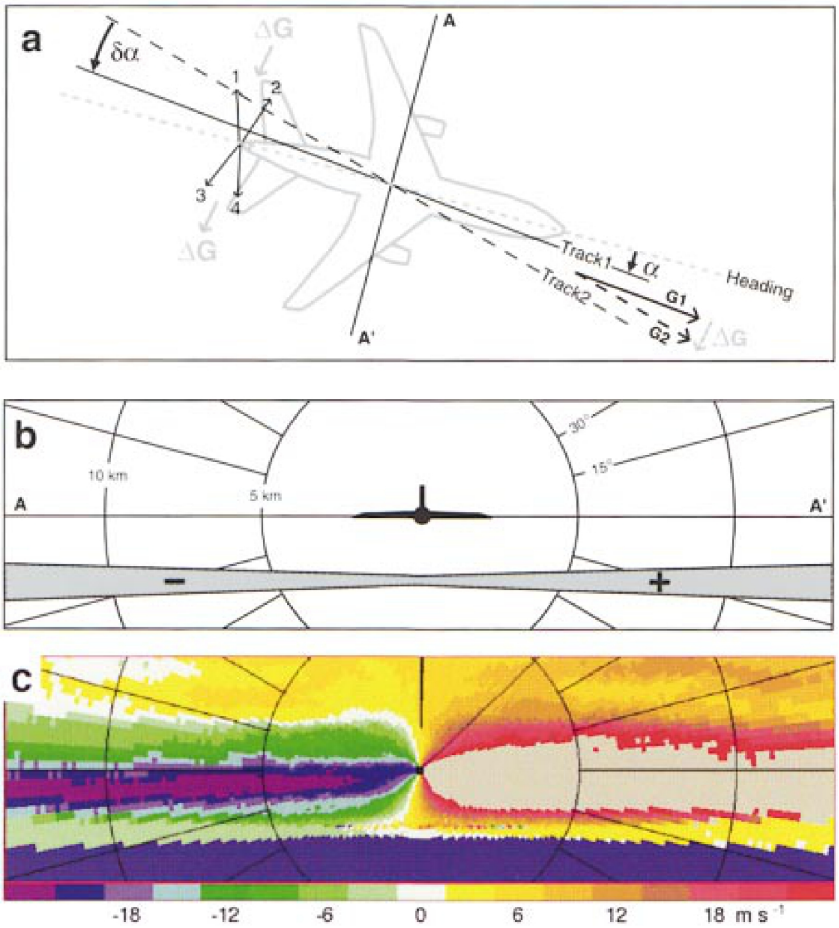

Figure 2.5: Schematic diagrams of the Doppler velocity pattern due to a negative drift error ($\delta\alpha < 0$). (a) Difference between track and heading defining the drift angle $\delta\alpha$. (b) Illustration of the residual surface velocities appearing on the fore radar display on the AA' cross section. Plus (+) and minus (-) indicate the sign of the residual surface Doppler velocities. The aircraft is located in the center of the plot and the gray shades represent the earth surface. (c) The corresponding radar display in (b) with observed data. Color scale shows the single Doppler velocities in m s^{-1}. Warm (cold) colors are Doppler velocities moving away (toward) the radar. Gray colors represent values off the color scale. From Bosart et al. (2002).

tivity, radial velocity and spectral width. The raw data can not be analyzed directly, but have to be pre-processed because they contain a lot of non-weather echos along with the information of interest (see Fig. 2.6). First of all the navigation corrections are applied and then the data are edited both automatically and manually for noise, ground echos, radar side lobes and second trip echos. To identify noise, the

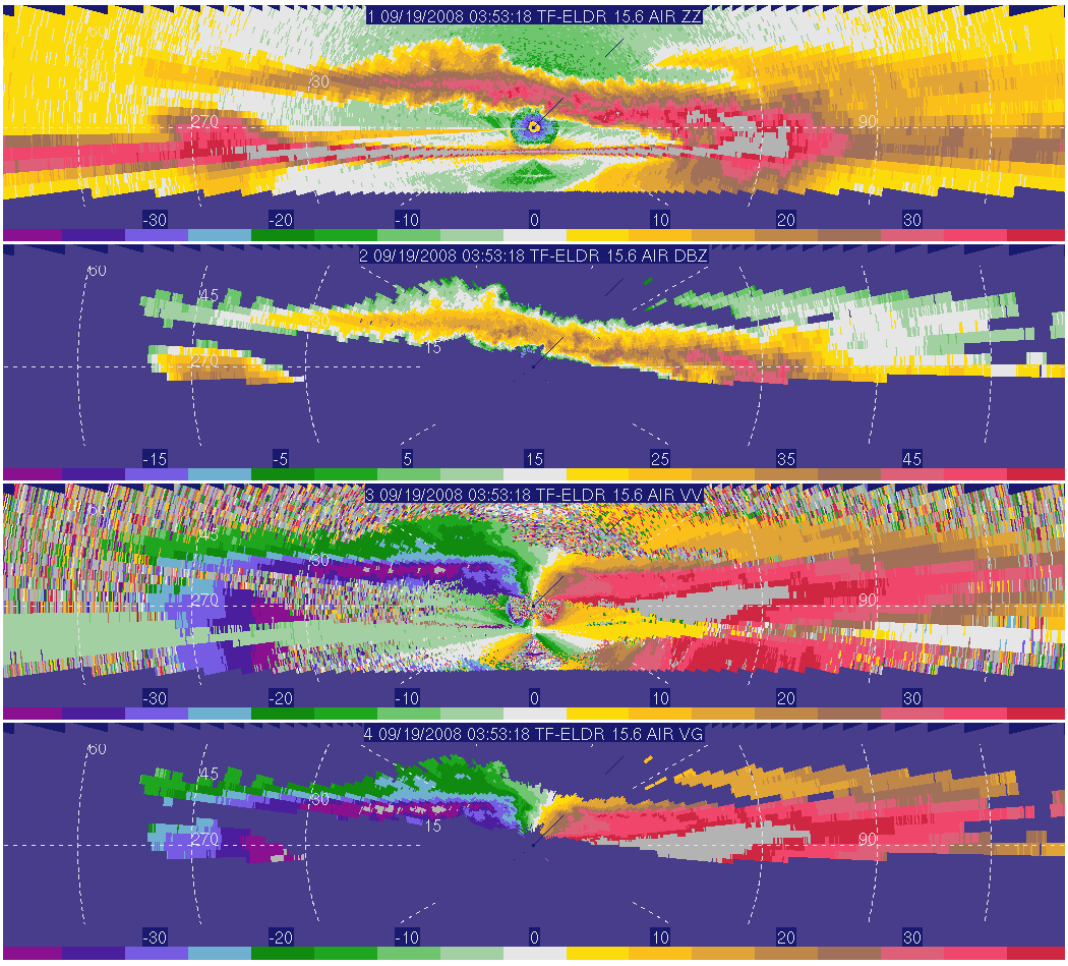

Figure 2.6: Panel of raw and edited data for radar reflectivity and radial velocity. The reflectivities are given in dBz and the velocities in m s^{-1}. Gray colors show values exceeding the color scale.

additionally recorded fields such as spectral width and normalized coherent power are very helpful and most of the noise can be removed automatically. Distinguishing other artifacts, such as side lobes, objectively from weather returns is very difficult and thus needs manual editing.

In the example shown in Fig. 2.6 many of the non-weather echos can be identified looking at the fields of radar reflectivity and radial winds. The aircraft is always located in the center of the plots. The first subfigure shows the raw data of radar reflectivity, the second one the edited radar reflectivity, the third one the raw data of radial velocity and the forth subfigure the edited radial velocity. In the unedited

reflectivity strong ground clutter can be seen, indicated by the horizontal gray band. The side lobes can be best identified in the raw velocity data. Around the aircraft there is a circle of strongly varying velocities, reaching from blue to red, surrounded by green areas on the lefthand side and yellow areas on the righthand side. These green and yellow areas also appear being mirrored at the ground axis. This pattern indicates that the sidelobe's signal was reflected at the ocean's surface and dominate the detected signal, because the reflection of the mainlobe's signal was very weak.

The edited data can then be interpolated on a regular grid and three dimensional wind fields can be derived using methods developed by Carl Mohr and Jay Miller NCAR/MMM (Mohr, 1988) or John Gamache (Reasor et al., 2009). We will take another approach in this work and first combine the radar data with data from other measurements such as dropsondes. The wind field is then calculated, using a variational technique, described in section 2.6.

2.6 SAMURAI

The **S**pline **A**nalysis at **M**esoscale **U**tilizing **R**adar and **A**ircraft **I**nstrumentation (SAMURAI) was developed by (Bell, 2010, Bell et al., 2012) with the goal to obtain an objective best estimate of the state of the atmosphere using as much information as possible. The analysis uses a variational data assimilation approach. It minimizes a cost function, that determines the departure of the background field and the observations from the "true" state of the atmosphere under a mass continuity constraint. Characteristics of this software program are that it uses cubic B-splines as a basis and that it minimizes the cost function in observational space rather than on a Cartesian grid. The advantages of these approaches will be examined in detail below.

The challenge is to obtain a best estimate of the true state of the atmosphere, having measurements of different quality and at randomly distributed locations. Moreover not only the value of a certain variable at a given grid point is of interest, but also its derivatives. To use a standard interpolation method would result in a memory intensive storage of interpolation coefficients and finite difference operators. A spectral approach such as a Fourier spectral transform would be desirable, but goes along with problems in incorporating boundary conditions. To utilize the strengths of both of these methods, an approach using cubic B-splines is chosen for SAMURAI. They can easily incorporate boundary conditions while not being as storage intensive, and are more accurate in calculating derivatives than the classical finite element approach. The disadvantage of B-splines in comparison to a spectral technique is the fact that cubic B-splines are neither analytic nor orthogonal. Thus the computational effort is higher, e.g. because matrix inversions are necessary. But that is justifiable, given the accuracy achieved and the versatility of the spline method.

Before going into detail of the analysis itself, it is helpful to have a look at the characteristics of the cubic B-splines (see Ooyama (2002)). Cubic splines are used, because this is the lowest order of splines that supports the required smoothness for both the analyzed variable and its derivative. The name B-spline refers to the fact, that a given (here for simplicity only one dimensional) function $u(x)$ is approximated by a superposition of **b**asic splines:

$$u(x) = \sum_{m \in M} \phi_m(x)\ a_m \tag{2.11}$$

with the basic function $\Phi(\xi)$ being assigned to each equidistant node x_m:

$$\phi_m(x) = \Phi\left(\frac{x - x_m}{\Delta x}\right) \tag{2.12}$$

$$\Phi(\xi) = \begin{cases} \frac{1}{6}(1 - |\xi|)^3 - \frac{2}{3}(1 - |\xi|)^3 & \text{if } 1 \geq |\xi| \geq 0, \\ \frac{1}{6}(2 - |\xi|)^3 & \text{if } 2 \geq |\xi| \geq 1, \\ 0 & \text{if } |\xi| \geq 2. \end{cases} \tag{2.13}$$

Fig. 2.7 shows how a combination of basic splines can approximate every possible function, be it constant, linear or any other shape. Boundary conditions can be incorporated easily because of the local nature of the splines by setting the cubic spline coefficients near the edge of the domain according to the required conditions.

Starting from randomly distributed observations, several transformations are nec-

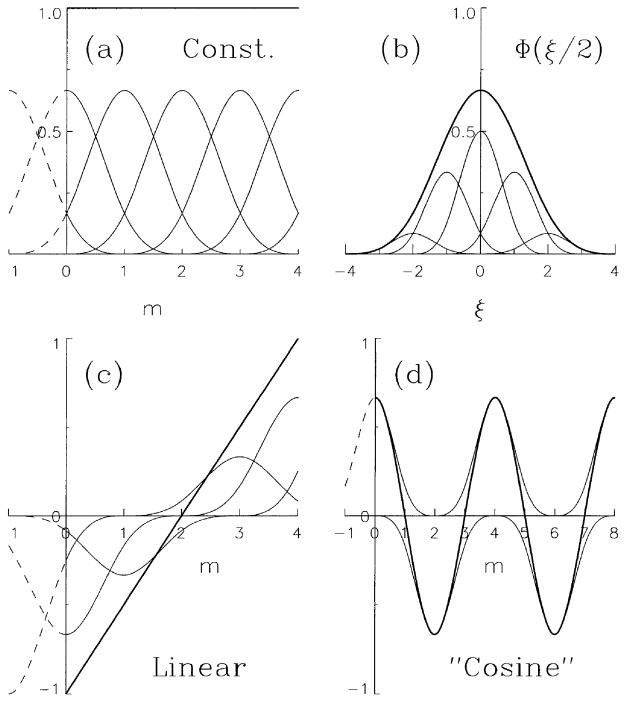

Figure 2.7: Simple examples of cubic-spline functions (thick lines): (a) a constant, (b) a double-width B-spline, (c) a straight line, and (d) a 4Δx cosine approximate. Thin lines are contributing members of nodal splines. From Ooyama (2002).

essary to gain spline coefficients a_m at equidistant nodes and thus a cubic spline function that represents the best approximation. The function $\breve{u}(x)$ is known only at a finite number $\bar{\imath}$ of points x_i with its respective weights w_i.

$$b_m = \sum_{i=1}^{\bar{\imath}} \phi_m(x_i)\breve{u}(x_i)\ w_i \tag{2.14}$$

This means that the value of the cubic spline coefficient at a particular node is determined by the surrounding observations. Due to the definition in Eq. 2.13, the basic spline is non-zero only in a radius of $2 \cdot \Delta x$. Thus, the summation is actually limited to the observations in the vicinity of the node.
The first transformation $\mathbf{b} = S_B[\breve{u}]$ (Eq. 2.14) changes the representation from randomly distributed values to a nodal representation. Subsequently, this nodal representation is transformed to cubic spline coefficients, $\mathbf{a} = S_A[\mathbf{b}]$:

$$\mathbf{a} = (\mathbf{P} + \mathbf{Q})^{-1}\mathbf{b} \tag{2.15}$$

where the coefficients are determined by the method of least squares ($\mathbf{P}$) with an additional third derivative constraint ($\mathbf{Q}$) to act as a low-pass filter. This matrix equation is the result of minimizing the cost function J in case of no boundary conditions:

$$J = \int \left\{ \left[\breve{u}(x) - u(x)\right]^2 + \epsilon_q(x) \left[u'''(x)\right]^2 \right\}\ dx \tag{2.16}$$

with ϵ_q being the weighting function of the third derivative constraint. The last transformation $u(x) = S_I[\mathbf{a}]$, given in Eq. 2.11, is then used to retrieve the best approximation of the function $\breve{u}(x)$ at point x. Thus the best approximation $u(x)$ of the function $\breve{u}(x)$ is found using these three transformations. Of course, this one dimensional representation can be extended straight forward to three dimensions.
Following Gao et al. (2004), SAMURAI uses a cost function that is more complex than the one proposed in Eq. 2.16 by Ooyama (2002). It incorporates a background field in addition to the observations and takes background, instrument and representation errors into account.
Based on Bayesian's first principles, the assumptions that the errors are random and

the probability distributions are Gaussian, the probability that state x is the true state of the atmosphere x_t, is:

$$P(y = y_t|x = x_t) = C \cdot exp\left(-\frac{1}{2}(x_t - x_b)^T \mathbf{B}^{-1}(x_t - x_b) - \frac{1}{2}(y_t - h(x_t))^T \mathbf{R}^{-1}(y_t - h(x_t))\right) \tag{2.17}$$

$$C = \frac{1}{2\pi \ |\mathbf{B}|^{\frac{1}{2}} \ |\mathbf{R}|^{\frac{1}{2}}} \tag{2.18}$$

where $\mathbf{B} = [x_\epsilon x_\epsilon^T]$ denotes the "background" error covariance matrix ($x_\epsilon = x_t - x$). The background state is defined on an equidistant grid, denoted by x, whereas the observational space is denoted by y. The forward model h(x) maps from the gridded space to observational space and, if h(x) is a linear function, this Bayesian approach is equivalent to a least-squares approach. The covariance matrix $\mathbf{R} = [y_\epsilon y_\epsilon^T]$ accounts for instrument and representation errors ($y_\epsilon = y_t - h(x_t)$).
The maximum likelihood estimate for the true state of the atmosphere is achieved by maximizing the exponent of Eq. 2.17, or equivalently minimizing the cost function J(x):

$$J(x) = J_B + J_O = \frac{1}{2}(x_t - x_b)^T \mathbf{B}^{-1}(x_t - x_b) + \frac{1}{2}(y_t - h(x_t))^T \mathbf{R}^{-1}(y_t - h(x_t)) \tag{2.19}$$

J_B measures the departure of the analysis from the background, J_O measures the departure of the analysis from the observations. The departures are weighted by the inverse of the respective error covariance matrices. Gao et al. (2004) use an additional mass continuity constraint in the cost function. In SAMURAI the mass continuity constraint is incorporated in a different way, because the use of the cubic B-spline basis allows the representation of gradients. Thus at each of the grid nodes a "pseudo-observation" of momentum gradients is placed in order to equal the sum of the momentum gradients to zero.
If the second-order derivative of J(x) is positive definite, there is a unique best estimate for the true state of the atmosphere. The minimization of J(x) is achieved by finding the state, where the derivative of J(x) equals zero:

$$\nabla J(x) = \mathbf{B}^{-1}(x_t - x_b) + \mathbf{H}^T \mathbf{R}^{-1}\left(y_t - h(x_t)\right) = 0 \tag{2.20}$$

In order to solve this equation it is necessary to store and invert the background error covariance matrix $\mathbf{B}$. This has large memory requirements and is computationally

intensive. To avoid this, an incremental approach is taken. The increment is defined as the difference between the true state and the background:

$$\delta x = x_t - x_b \tag{2.21}$$

Defining a symmetric matrix $\mathbf{C}$, that has the same eigenvectors as $\mathbf{B}$ and the same eigenvalues as the square root of $\mathbf{B}$ ($\mathbf{B} = \mathbf{C}^T\mathbf{C}$), and the control variable vector $q = \mathbf{C}^{-1}\delta x$, yields

$$\nabla J_{inc}(q) = \left(\mathbb{1} + \mathbf{C}^T\mathbf{H}^T\mathbf{R}^{-1}\mathbf{H}\mathbf{C}\right) q - \mathbf{C}^T\mathbf{H}^T\mathbf{R}^{-1}d \tag{2.22}$$

where d denotes the so called "innovation vector"

$$d = h(x_b) - y_t \tag{2.23}$$

The minimization of the cost function is carried out in various iteration steps. In addition to Eq. 2.22, its derivative has to be calculated to determine the search direction of minimization. A criterion to stop the iteration process, such as that the derivative goes below a certain threshold, has to be fixed.
In order to speed up the convergence of the minimization procedure, a control variable q is introduced. Its quotient between the largest and smallest eigenvalues of the second-order derivative of J(q) is smaller than that of J(δx).
In SAMURAI, the control variable state vector q is defined as following:

$$q(x, y, z) = \{\rho u, \rho v, \rho w, T', q_v', \rho'\}^T \tag{2.24}$$

where ρ is the total density, T is the temperature and q_v the water vapor mixing ratio. The primes denote the departure from a hydrostatic reference state given by the moist tropical mean sounding from Dunion (2011). All relevant physical variables can be derived from this state vector. The different variables of q were chosen in a way, that they have a smooth distribution and their error correlations are well approximated by a Gaussian distribution. This enables to simplify the background error matrix $\mathbf{B}$ by modelling part of it as a recursive filter (Purser et al., 2003). The length scale of this recursive filter then acts as both an effective distance for the influence of the observations and as a spatial filter. A large value helps spread the information provided by an observation but also removes fine-scale details from the analysis.

As denoted above, the minimization of the observational error is performed in observational space. That reduces the errors that originate from interpolating radar observations to a regular grid and preserves the radial nature of the radar observations. Thus, the Cartesian wind velocities have to be transformed to observational space:

$$V_r = \frac{(X - X_0)u + (Y - Y_0)v + (Z - Z_0)w}{r} \tag{2.25}$$

where u, v and w are the wind components in Cartesian coordinates (X,Y,Z) and (X_0,Y_0,Z_0) is the radar location. The radial velocity that is measured by the radar, is the velocity of the detected hydrometeors. To obtain the air motion, the fall speed of the hydrometeors has to be subtracted from the measured velocity.

$$V_r = V_r^a + w_t \sin\theta \tag{2.26}$$

where V_r is the true velocity of the air, V_r^a the actually observed velocity, w_t the terminal fall speed of the hydrometeors and θ the elevation angle. Since the terminal fall speed w_t depends on the size of the particles, it can be determined roughly from the reflectivity. Below the melting level an empirical relationship derived by Joss and Waldvogel (1970) is used, and above it one that was derived by Atlas et al. (1973).

In regions where there are no observations the analysis relaxes to the background state. This can result in discontinuities in the state vector variables, because of the different data density. To avoid this problem, the reflectivity can be masked. In other words, only grid points with at least one reflectivity value in their direct vicinity exceeding the fixed threshold, are computed. All other grid points have no assigned value.

The optimal adjustment of the various parameters depends on the particular case. So the resolution of the Cartesian grid, the errors of the background field (u,v,w,T,q,ρ), the weight of the mass continuity constraint, the spline cut-off Δx, the length scale of the recursive filter and a constraint for the upper boundary can be set in a separate SAMURAI configuration file.

SAMURAI was developed initially to examine tropical cyclones. To account for their translation during the data collection, the analysis is performed in a storm relative system.

2.7 Remote sensing via satellites

Satellites provide products such as infrared, visible, water vapor and microwave imagery. In order to be able to interpret these data correctly, it is necessary to understand what information they contain. As described in Laing and Evans (2010), infrared instruments sense the energy that is emitted from cloud tops and thus their temperature. The higher the clouds reach, the colder they are. So the cloud top temperature displayed in infrared imagery, is a measure for the height of the clouds. Water vapor imagery tracks mainly mid- and upper-level moisture, but can shed no light on the water content of lower levels. For this purpose it is better to use imagery of total precipitable water, because there the water vapor is integrated in a vertical column and the largest fraction of water vapor is concentrated at lower levels.
Microwave imagery is useful to get further insight in the distribution of hydrometeors. Low-frequency channels (5 to 37 GHz) are sensitive to energy emitted from medium-to-large-sized raindrops that are mainly located below the freezing level. Higher frequency channels (80 to 300 GHz) mostly gather information about ice particles above the freezing level. Thus these two channels complement each other and give valuable information about the character and distribution of the hydrometeors.

3 Overview Sinlaku

In this study the structural characteristics of Typhoon Sinlaku (2008) after its re-intensification are examined. The analyzed data were gathered during the **T**HORPEX **P**acific **A**sian **R**egional **C**ampaign (T-PARC). This multi-national field campaign

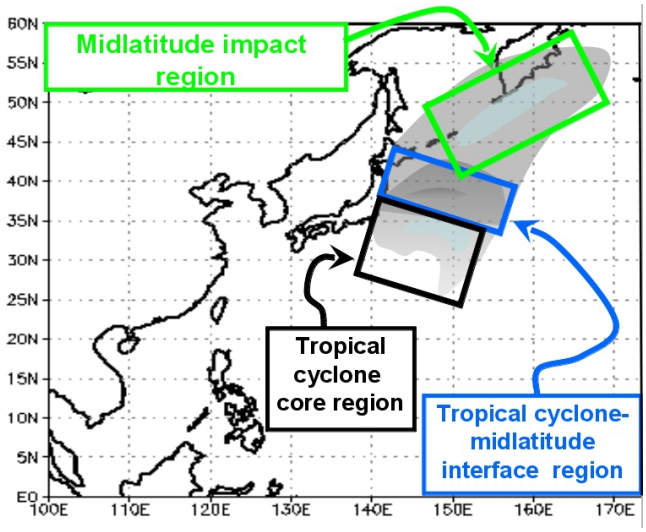

Figure 3.1: Schematics of three regions associated with the extratropical transition of a decaying tropical cyclone over the western North Pacific. The light gray shaded regions represents overall cloud patterns. Shaded regions within the light gray areas indicate regions of concentrated cloud amounts defined by convection in the tropical cyclone core region, largescale precipitation in the tropical cyclone midlatitude interface region, and cirrus in the midlatitude impact region. From P. Harr in Chan and Kepert (2010).

took place in the western North Pacific from August through October 2008, in cooperation with the Tropical Cyclone Structure TCS08 experiment (Elsberry and Harr 2008). One of its goals was to identify important physical characteristics associated with the extratropical transition of tropical cyclones. Therefore three research aircraft (NRL P-3, USAF WC-130J and DLR Falcon) equipped with Lidar, Radar, GPS Dropsondes and AXBTs (airborne expendable bathythermograph) investigated

the three regions that are characteristic for a cyclone moving into the extra tropics: the tropical cyclone core region, the tropical cyclone-midlatitude interface region and the midlatitude impact region (Fig. 3.1).
The WC-130J and the NRL P-3 primarily provided data about the physical characteristics of the tropical cyclone in the core and midlatitude interface regions, with the WC-130J also being able to obtain measurements in the inner core of a mature tropical cyclone. The DLR Falcon, equipped with an airborne Doppler wind lidar and a water vapor differential absorption lidar (DIAL) mainly observed the upper-level outflow in the midlatitude impact region.

3.1 Sinlaku's life cycle

Typhoon Sinlaku was one of four typhoons during T-PARC. It was first classified as a tropical depression on 8 September, developing east of the Philippines and moving north-westward. After a period of rapid intensification it reached typhoon strength at 12 UTC on 9 of September (Fig. 3.2 and 3.3). It intensified further, peaking on 10 and 11 September with a central pressure of 935 hPa and maximum winds of 100 knots. It moved further north-westward, remained almost stationary

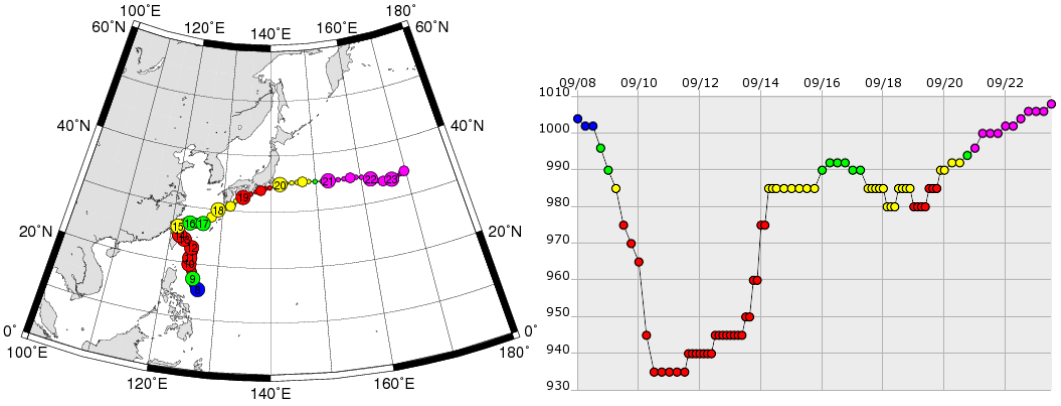

(a) (b) central pressure chart (utc)

Figure 3.2: (a) Best track of Typhoon Sinlaku. The numbers in the circles indicate the location of the cyclone at 00UTC on that date in September 2008. (b) Central pressure of Sinlaku with the pressure in hPa on the ordinate and the time on the abscissa. The color in both plots indicates the strength of the cyclone: tropical depression (blue), tropical storm (green), severe tropical storm (yellow), typhoon (red) and extratropical cyclone (magenta). From KITAMOTO Asanobu / National Institute of Informatics (2011).

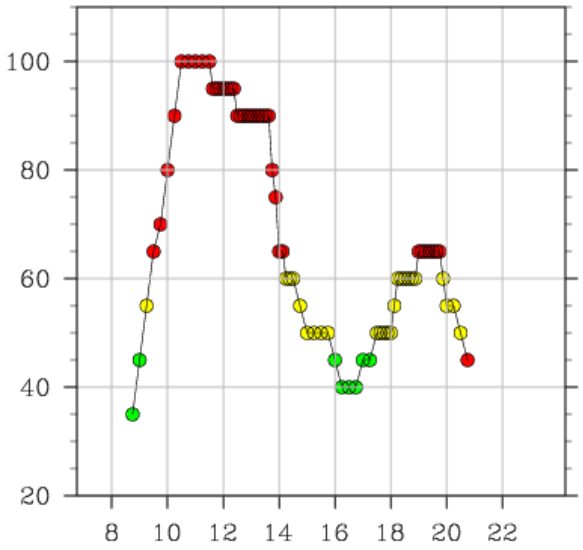

Figure 3.3: Temporal evolution of wind speed in knots. Day of September on the abscissa and wind speed on the ordinate. Colors indicating the strength of the cyclone as in Fig. 3.2.

to the east of Taiwan for a while and finally made landfall in the northern part of Taiwan on 13 September. The influence of Taiwan weakened Sinlaku remarkably. It lost its typhoon strength on 14 September. Sinlaku recurved on 15 September, moved north-east and weakened further to a tropical storm with a central pressure of 992 hPa and maximum winds of 40 knots on 16 September. This weakening after recurvature and the concurrent movement toward the midlatitudes was defined as the transformation stage of extratropical transition by Klein (2002). But instead of completing the transformation and adopting extratropical characteristics, Sinlaku re-intensified starting 17 September. This re-intensification period was examined in detail by Sanabia (2010), who found that three mesoscale vortices interacting with the decaying tropical storm initiated the re-intensification, which was then followed by multiple convective bursts. During this intensification Sinlaku moved further to the north-east and later along the southern coastline of Japan. On 19 September the tropical storm was again classified as a typhoon, reaching a central pressure of 980 hPa and wind speeds of 65 knots, with the wind speed showing a more distinct change than the central pressure. After 18 UTC on 19 September, Sinlaku began finally to weaken again, accelerating toward the east and entering its extratropical stage on 21 September.

3.2 Larger scale environment

This study will focus on the physical characteristics of Sinlaku at the time after re-intensification. The radar data taken by the P-3 between 03.50 a.m. and 4.15 a.m. on 19 September is the main part of the data set. Here the resulting analysis is put into context by analyzing the environment in which Sinlaku is embedded.

The considerable structural changes that Sinlaku experienced since the beginning of the re-intensification period, can be seen in water vapor imagery (Fig. 3.4). Recall that only water vapor in mid- to upper-levels is depicted and thus no conclusions can be drawn regarding the low level moisture. At 00.30 UTC on 17 September, Sinlaku is located between Taiwan and Japan and is still connected to a band of moister air that elongates to the south-west of Sinlaku. West of Sinlaku is a region of drier air advancing eastward, which results in a sharp moisture gradient at the western edge of Sinlaku. Over time this region of reduced moisture extends further south. At the beginning of the re-intensification period (Fig. 3.4(a)), Sinlaku is connected to the deep tropics via a band of higher moisture values with embedded convection extending southwestward of Sinlaku. This connection becomes weaker over time, at 12.30 UTC on 18 September this moisture band is clearly disrupted and Sinlaku is surrounded by drier air in the south.

The structure of the moisture to the northeast of Sinlaku also varies over time. On 17 September at 12.30 UTC, the region northeast of Sinlaku is significantly moister than 12 hours before, probably due to enhanced outflow. This moist region broadens during the next day. On 19 September at 00.30 UTC the moist region northeast of Sinlaku has been transported further downstream. The dry region, located in the upper left corner in Fig. 3.4(b) is likely related to the jet stream. On 18 September this dry region moves further eastward, passing Sinlaku at its northern side. A resulting large moisture gradient can be seen in Fig. 3.4(c) and 3.4(d), which probably illustrates the impingement of the moist outflow of Sinlaku on the jet stream. The water vapor content in the core region of Sinlaku decreases steadily during the sequence of plots 3.4(b) - 3.4(f), indicating that either the convection is decaying or there is less moisture that can be transported upward. Moreover, the core region exhibits different structures over time. Until 18 September at 00.30 UTC convective bursts are a dominant feature in the water vapor imagery. For example at 00.30 UTC on 17 September (Fig. 3.4(a)) there is one intense maximum of moisture located in the western part of the convection and 12 hours later, there are several regions with higher moisture values, located in the core region and extending

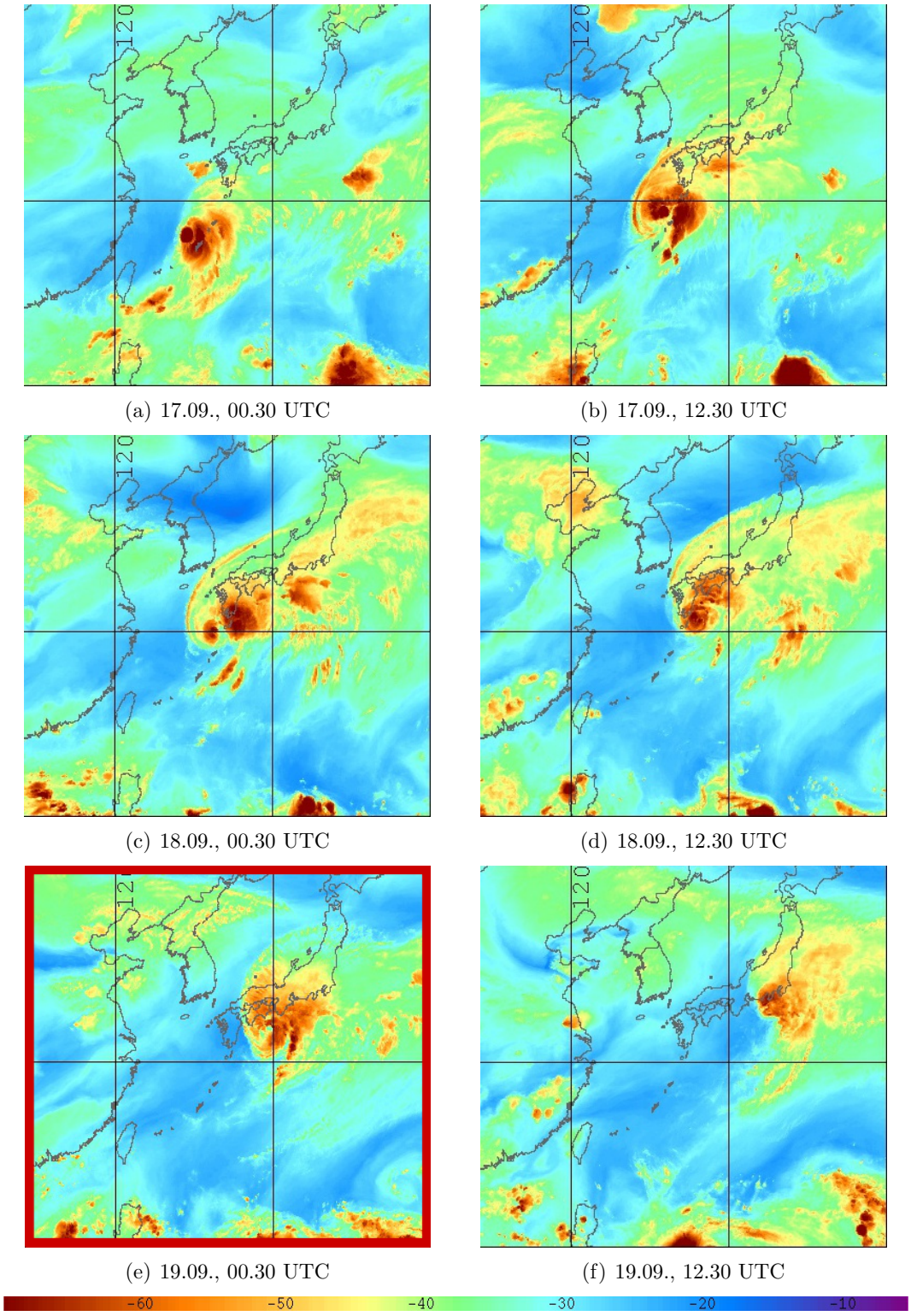

(a) 17.09., 00.30 UTC

(b) 17.09., 12.30 UTC

(c) 18.09., 00.30 UTC

(d) 18.09., 12.30 UTC

(e) 19.09., 00.30 UTC

(f) 19.09., 12.30 UTC

Figure 3.4: Water vapor imagery provided by the Naval Research Laboratory via the T-PARC field catalog. The plots cover an area from 115°E to 150°E and from 15°N to 43°N. The red box indicates the time closest to the time of the analysis.

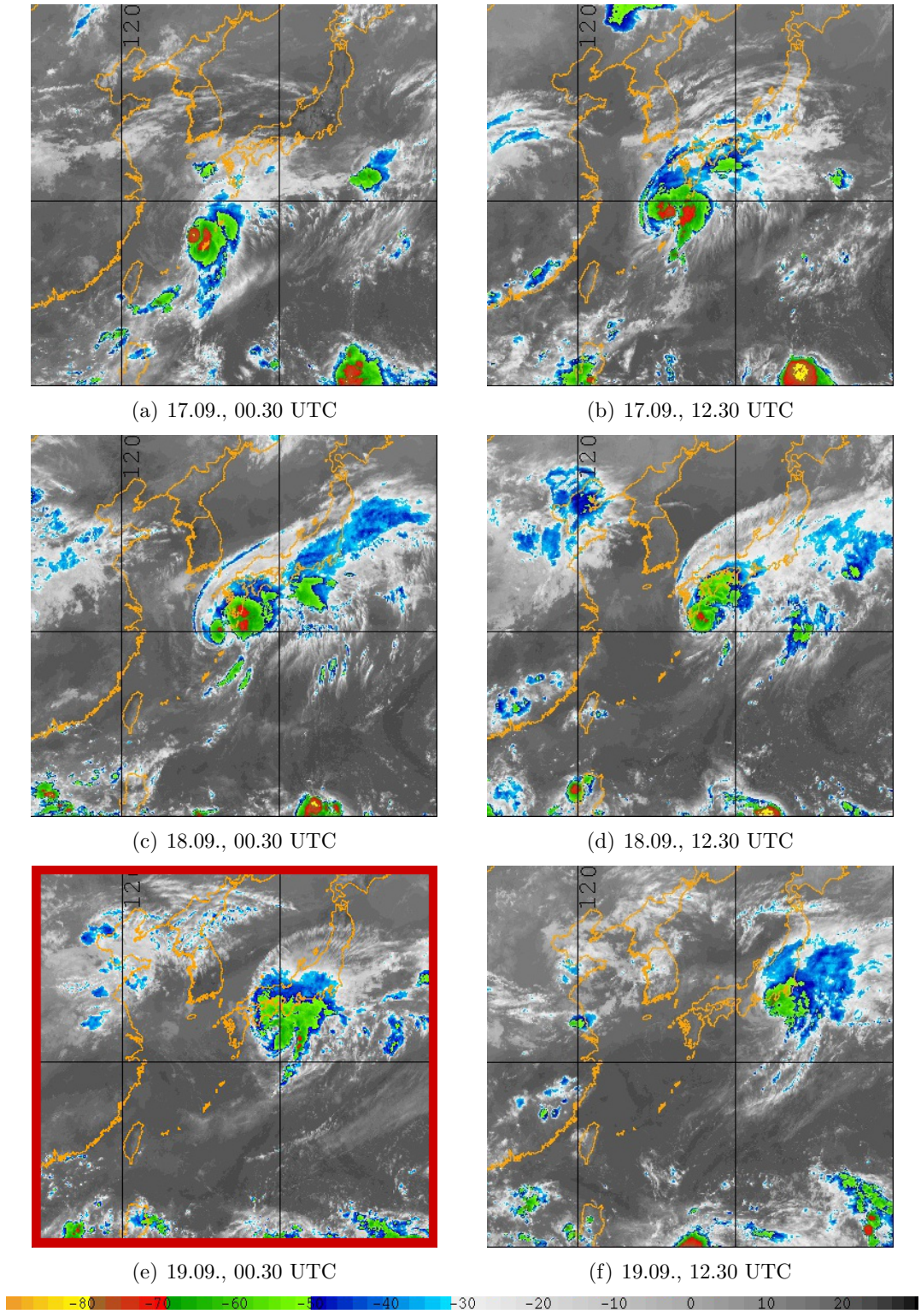

(a) 17.09., 00.30 UTC

(b) 17.09., 12.30 UTC

(c) 18.09., 00.30 UTC

(d) 18.09., 12.30 UTC

(e) 19.09., 00.30 UTC

(f) 19.09., 12.30 UTC

Figure 3.5: Infrared Color Imagery provided by the Naval Research Laboratory via the T-PARC field catalog. The plots cover an area from 115°E to 150°E and from 15°N to 43°N. The red box indicates the time closest to the time of the analysis.

into the region of the rainband to the south. In contrast, starting at 12.30 UTC on 18 September the water vapor imagery exhibits a more homogeneous structure in the core region of Sinlaku. A circular area of higher moisture can be seen in Fig. 3.4(d), which gets more asymmetric in the following 24 hours. The principal rainband starting in the east and elongating to the south can be seen most clearly in Fig. 3.4(e).
Complementing the water vapor imagery, the height of the cloud tops can be assessed in the infrared imagery shown in Fig. 3.5. As the water vapor content, the cloud top height decreases steadily over the sequence of plots 3.5(b) - 3.5(f) and the location of the highest clouds (red) in the infrared imagery coincides with the location of the convective bursts in the water vapor imagery. The broadest region of high clouds to the northeast of Sinlaku occurs on 18 September at 00.30 UTC, supporting the picture of enhanced upper level outflow. But as was also visible in the water vapor imagery, on 19 September at 00.30 UTC, this region to the northeast of Sinlaku is separated from the core region of Sinlaku and advected downstream.
Despite the fact that the water vapor imagery shows decreasing water vapor content in mid- to upper-levels and the infrared imagery shows decreasing cloud top heights over the depicted period of time, Sinlaku still intensified until the early 19 September based on central sea level pressure and maximum winds.

3.3 Interaction with the midlatitude circulation

In several studies it has been noted, that extratropical transitions are very sensitive to the midlatitude circulation pattern they move into. For example, Harr and Elsberry (2000) found two characteristic patterns for the western North Pacific that have very different influences on the decaying tropical cyclone. Depending on whether the primary midlatitude circulation is northwest or northeast of the decaying tropical cyclone, either an intense extratropical cyclone develops or the cyclone does not intensify significantly. Often, an upper level trough approaching from the west favors the interaction of the cyclone with the midlatitudes by providing an upper level jet streak just poleward of the decaying system with which the outflow can interact.
To investigate the location of Sinlaku relative to the midlatitude circulation, operational analysis data of the European Centre for Medium-Range Weather Forecasts (ECMWF) are used. The data are provided on a grid with a resolution of 0.25°,

which at a latitude of 33°N corresponds to approximately 25 km. This resolution is too coarse to represent the detailed structure of a tropical cyclone, but it is useful to get insight into the environmental conditions that surround the tropical cyclone. In order to determine the position of Sinlaku relative to midlatitude features, tropopause charts are commonly used. Therefore, the potential temperature θ is plotted on a surface of 2 PVU (Ertel potential vorticity units), which is considered to represent the dynamic tropopause (Hoskins et al., 1985). In general, lower potential temperatures are due to a lowered tropopause, referred to as a tropopause depression and higher potential temperatures are due to a raised tropopause. So upper-level troughs are associated with low θ values on the dynamic tropopause and inversely an upper-level ridge is associated with high θ values (Morgan and Nielson-Gammon, 1998). In Fig. 3.6 a strong gradient of potential temperature can

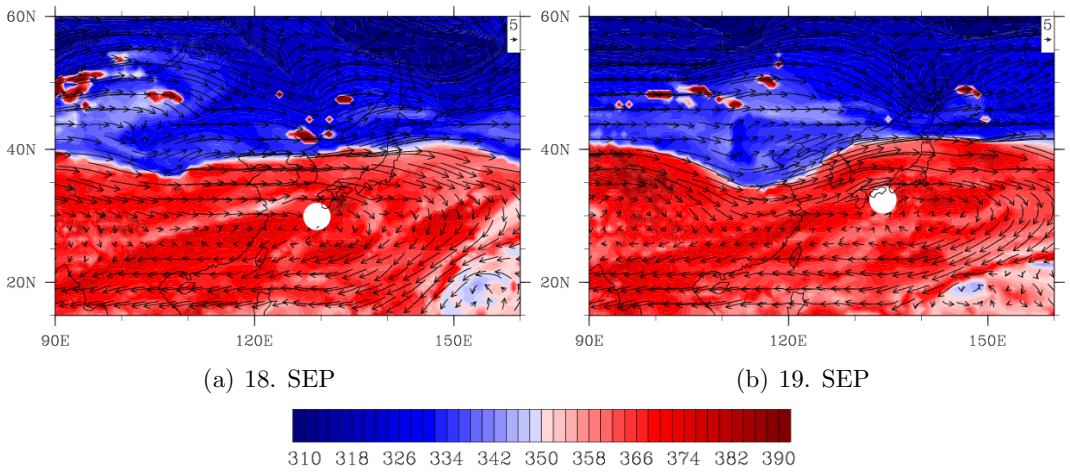

(a) 18. SEP (b) 19. SEP

Figure 3.6: Potential temperature (shaded) and wind vectors on the 2 PVU surface. The white circle marks the best track position of Sinlaku.

be seen at about 40°N. It illustrates the slope of the height of the tropopause from the tropics to the midlatitudes. Superimposed on this general pattern, features such as troughs and ridges can be seen.

As on the days before (not shown), on 18 September there is no distinct trough apparent. The strong gradient of potential temperature is aligned zonally. Moreover, Sinlaku is located more than 5° south of this gradient zone and the wind vectors indicate relatively low wind speeds at the location of Sinlaku. On 19 September (Fig. 3.6(b)) there is a weak trough located to the west of Sinlaku at around 115°E. The absolute distance of Sinlaku to the gradient zone has not changed significantly in comparison to the previous day. But the weak trough to the west of Sinlaku results

in enhanced wind speeds both in front of the trough and at the position of Sinlaku. In conclusion, these tropopause charts suggest, that Sinlaku did not directly interact with the midlatitude circulation pattern in the form of the weak trough to the west of it. Sinlaku was rather influenced indirectly by the trough, because it increased the shear of the environmental flow in which Sinlaku is embedded.

3.4 Environmental flow

One of the most important factors that influence the properties of a tropical cyclone is the environmental flow in which it is embedded (see section 2.2). The tropopause charts in the last section showed an increase in upper level wind speed, which is likely to translate into increased vertical shear. To further elucidate this, the ECMWF operational analysis data are used to calculate the environmental flow. The wind field is a superposition of the environmental flow and the circulation of the tropical cyclone. In order to remove the circulation of the tropical cyclone, the environmental flow is calculated by averaging the zonal and meridional components of the horizontal winds over an area with a radius of 500 km centered on the best track position of Sinlaku. This method "removes" the cyclone's circulation under the assumption that the circulation is roughly symmetric. The sensitivity of the results to the averaging radius was tested by performing the technique also for radii of 400 and 600 km, but no significant differences were found. Hence, the results are assumed to be robust.

The temporal evolution of the environmental flow on different pressure levels can be seen in Fig. 3.7. At lower levels up to around 700 hPa the winds are predominantly southerly with magnitudes of 5 m s^{-1}, turning to south-westerlies over time. At upper levels down to 300 hPa first there are south-westerlies, turning to almost purely westerlies and intensifying from 10 to 20 m s^{-1}. The levels of 300 to 500 hPa exhibit not that much change over time. They consist of westerlies, that gain a little bit of intensity, but not as significantly as the upper levels.

With the increased wind speeds the shear increases with time also. Following Davis et al. (2008), the shear is defined as the difference of the environmental wind speeds between 400 and 900 hPa. Thus for 00 UTC on 19 September, which is closest to the time of the analysis presented in later chapters, the shear vector has a magnitude of 7.50 m s^{-1} and the shear is west-southwesterly. More precisely the shear angle amounts to 76.35°, where 0° is north and the angle is measured clockwise. This is a magnitude of shear, that typically a tropical cyclone can withstand. To decrease

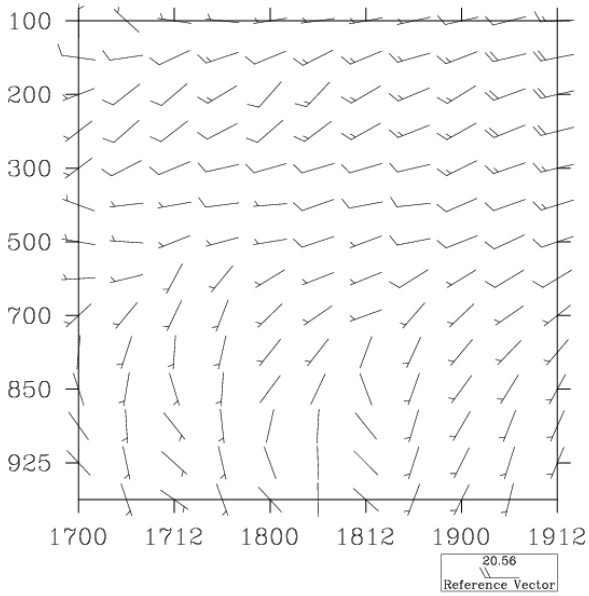

Figure 3.7: Average environmental flow in the area around Sinlaku. On the abscissa the time from 17 September at 00 UTC to 19 September at 12 UTC is plotted and on the ordinate the pressure levels in hPa. The average environmental flow was computed by averaging the zonal and meridional components of the horizontal winds of the ECMWF operational analysis over an area with a radius of 500 km centered on the best track position of Sinlaku.

the total vortex circulation, the shear would have to approach values of 20 m s^{-1} (Davis et al., 2008).

3.5 Eyewall structure

After examining the larger scale environment, finding that Sinlaku does not directly interact with a midlatitude trough and that the shear is significant but not destructive, a closer look is taken at the finer structure of Sinlaku.

ECMWF data can not be used because the resolution is too coarse, but satellite microwave imagery provides useful insights. As mentioned above, the main data source for our analysis is the radar data collected between 03.50 a.m. and 04.15 a.m. on 19 September. In this time span, more precisely at 03.59 UTC, NASA's Aqua-1 satellite passed over Sinlaku's position and provided microwave scans (see Fig. 3.8). These scans give insight into the horizontal structure of the eyewall and, since the

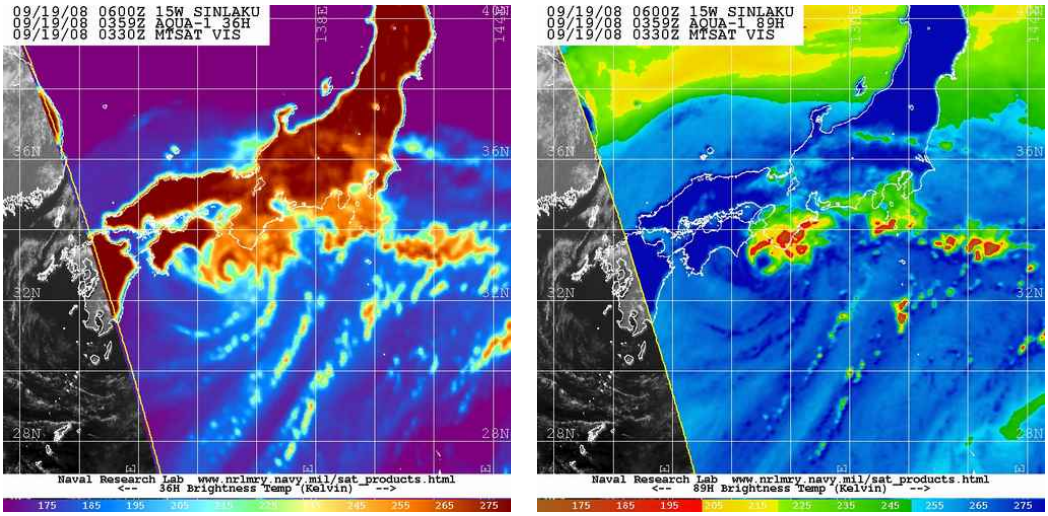

(a) 36 GHz (b) 89 GHz

Figure 3.8: Microwave imagery of Sinlaku at 03.59 UTC on 19 September provided by NASA's Aqua-1 satellite. (a) 36 GHz, mostly sensitive to lower-level rain. (b) 89 GHz, mostly sensitive to ice particles.

two channels are sensitive to particles at different heights, conclusions about the vertical structure can be drawn also. In general, the eyewall can be seen clearly around a distinct eye in both scans. There is a large region of convection directly adjacent to the northeast of the eye and further convection is located to the east with rain bands extending to the south.

The eyewall is broken in both cases, but in different locations. The 36 GHz plot exhibits the gap to the southeast, whereas it is located to the southwest in the 89 GHz plot. This points to differences in the vertical extent of convection around the eyewall. Recall that the 36 GHz channel is primarily sensitive to lower-level rain and the 89 GHz channel to ice particles. Hence, the straightforward interpretation is that the convection in the southwestern quadrant of the eyewall is weaker than elsewhere around the eyewall. The convection does not extend that far in the vertical and thus there are no ice particles at upper levels. Since there are no ice particles in higher levels, there are no falling hydrometeors that can be advected to the southeastern quadrant and produce rain there. In the 89 GHz plot the lowest brightness temperatures within the eyewall are measured in the north to northwestern part, which indicates that the convection is deepest in this region.

4 Analysis setup

4.1 Data set

The SAMURAI software (Bell, 2010, Bell et al., 2012) is used in this study to achieve the most likely estimate for the state of the atmosphere. It assimilates data from various observations in the core region of Sinlaku in the early hours of 19 September. The ELDORA doppler radar accounts for the main part of the data in this study. It provides measurements of reflectivity and radial velocities in a time slot between 03.50 and 04.15 UTC. The radar data were edited both automatically and manually as described in chapter 2.5 and navigation corrections were applied. The corrections were computed from a straight leg in stratiform precipitation earlier on the same flight (02.23.00 UTC to 02.26.00 UTC). Because of reasons explained later in this chapter, radar data from 03.55.23 UTC to 04.03.45 UTC were excluded.
In addition to the the radar data, dropsonde data of two aircraft (C-130, P-3) provide information about pressure, temperature, relative humidity, horizontal wind speed and wind direction. The C-130 released 6 dropsondes at a height of 9.3 km and the P-3 released 8 dropsondes at a height of 3.1 km in the core region of Sinlaku. These dropsonde data were provided by NCAR/EOL under sponsorship of the National Science Foundation. Moreover, the flight level data of the P-3 were included, containing measurements of pressure, temperature, moisture and horizontal winds. Indirect measurements of the windspeed and direction were retrieved by tracking cloud patterns in subsequent satellite imagery. The so called resulting "Atmospheric Motion Vectors" (AMVs, e.g. Velden (1996), Velden et al. (1997, 2005)) were provided by the Cooperative Institute for Meteorological Satellite Studies (CIMSS).
As stated in section 2.6, the SAMURAI technique needs an initial background state. Thus, the ECMWF operational analysis at 00UTC on the 19th of September, which is part of the YOTC ("Year" of Tropical Convection", a joint project of the WWRP-THORPEX and the WCRP) data set, is used. This analysis has a resolution of 0.25° (T799), which as mentioned above, is not high enough to represent a tropical cyclone

in detail, but captures the broad features and hence is a good first estimate of the background state.
Thus, the SAMURAI analysis bases its estimate of the state of the atmosphere on radar data, dropsonde data, flightlevel data, AMVs and ECMWF analysis data.

4.2 SAMURAI setup

The spatial resolution of the data used in this analysis differs significantly. The ECMWF analysis has a resolution of approximately 25 km and the radar data has a resolution of a few hundred meters. To get the best analysis result, it is thus advisable to carry out the data assimilation in multiple steps. In this study, first a SAMURAI run is performed with a horizontal resolution of 10 km and a vertical resolution of 1 km, which then serves as a background state for a subsequent run with higher resolution.
This was especially important in the present case, because the tilt of the center in the radar data differed from the tilt in the ECMWF background field. A miss-represented center in the background field leads to large deviations in windspeed in comparison to the observations, because not only the magnitude but also the direction does not match. To account for this discrepancy, the errors of the background windspeeds would have to be set relatively high, which in turn reduces the positive effect of the background field in parts of the analysis domain that are more distant to the center. Thus, a better solution is to carry out the data assimilation in multiple steps and adjust the background field gradually to the measurements.
In the SAMURAI run with a resolution of 10 km the wind speed errors for the horizontal wind components u and v of the background field are set to 10 m s^{-1}, and that for the vertical wind component w to 2 m s^{-1}. The background error of temperature was estimated as 3 K, of specific humidity as 3 g kg^{-1} and of density as 30 g m^{-3}. The radius of influence of the background field is set to 30 km. The recursive filter, which acts as an effective distance for the influence of the observations and as a spatial filter, is set to 40 km in the horizontal and to 2 km in the vertical. The radar data are sampled in gates of a length of 150 m. To approximately match the vertical analysis resolution of 1 km 7 consecutive gates are averaged.
The analysis domain is chosen to comprise the whole core region of Sinlaku. For the 10 km run the domain was 200 km x 200 km large, centered around 32.9°N/135.2°E. The ground was used as the lower boundary and a height of 14 km was asigned to the

upper boundary. At this height the absolute vertical velocity values are constrained to be lower or equal 1 m s^{-1} and at 14.5 km the vertical velocity is set to zero.
This 10 km run is then used to serve as the inital guess of the background for two higher resolution runs. For these two runs a domain of 140 km x 140 km was used with a vertical extend of 14 km and a vertical resolution of 500 m. The horizontal resolution is set to 4 km in one run, and to 1 km in the other. These two different resolutions were chosen to be able to analyze different features of the core region of Sinlaku. For example, to investigate the general structure of the tropical cyclone regarding its vorticity pattern, it is easier to interpret a coarser resolution plot. Higher resolution plots feature many details and thus it can be harder to identify the general structure. In turn, for vertical velocities a higher resolution is preferable, because e.g. convective updraft regions are usually of small horizontal extent and would not be captured that well with lower resolutions.
In both higher resolution runs all grid points with no reflectivity or reflectivity values lower than -10 dBz are masked, to avoid sharp gradients that could occur because the field relaxes to the background field when no observations are present. The number of radar gates, over which the averaging is performed, is adapted to the higher vertical resolution in comparison to the 10 km run and thus only 3 instead of 7 radar gates are averaged. The radius of influence of the background field is 12 km in both cases, which is chosen to be slightly larger than the grid point distance. The errors, that were asigned to the background fields are also identical for both runs. The horizontal velocities u and v are estimated to have an error of 10 m s^{-1}, the vertical velocity 5 m s^{-1} and for the other remaining errors the same values as in the 10 km run are assigned. The error of the vertical velocity of the background field is set higher as in the 10 km run, in order to not constrain the observational data too close to the background field. It is known that the ECMWF analysis does not represent the tropical cyclone's structure in detail and thus also does not contain the strong updrafts, that are expected to occur in the eyewall convection. On the other hand the ELDORA Doppler radar has a high spatial and temporal resolution and thus measures these smaller scale features. In order for the resulting analysis to contain these smaller scale features, it is important to put less weight on the background field. This discussion also illustrates that the magnitude of the vertical velocities depends on the degree to which it is constrained to the background und thus the interpretation of the resulting vertical velocity field should focus on the spatial pattern rather than on the absolute values.
The spatial filter scale is set according to the different horizontal resolutions. The 1

km run uses a spatial filter with a distance of 2 km on both horizontal and vertical direction, the 4 km run uses a distance of 4 km in the horizontal and of 2 km in the vertical.

The SAMURAI analysis technique uses a storm relative framework. To compute the translation speed of Sinlaku, the best track data of 00 UTC and 06 UTC 19 September were used. This results in a translation to the east-northeast More precisely, the angle is 66° (0° is north and the angle is measured clockwise) and the translation speed is 8.8 m s^{-1}. This translation is used in all three SAMURAI runs.

As mentioned above, some of the radar data were excluded from the analysis. This has to do with the strong curvature of the flight track of the P-3, carrying the ELDORA Doppler radar. The track is marked in the horizontal cross sections in the next chapter. The aircraft approached the eyewall from the southeast, penetrating the eye. The initial plan was to complete a circle counterclockwise in the eye and then leave the eye through the opening in the eyewall to the southwest. But due to the fact that the circle was started too early, the aircraft hit the backward, southern part of the eyewall, and then completed a very narrow circle to get back into the eye and finally left the eye in westward direction. As was discussed in chapter 2.5, the accuracy of the calculation of the vertical velocity depends strongly on the curvature of the track. The stronger the curvature, the higher the uncertainty of the vertical windspeed calculation. In this study, the fanning out of the beams on the righthand-side of the track caused updrafts everywhere inside the circle and downward motion surrounding the circle. To avoid the introduction of errors in the vertical velocity because of the unfavorable geometry of the track, all the data in the curved part of the track were excluded. This affects the data taken from 03.55.23 UTC to 04.03.45 UTC.

5 Results

5.1 Structural characteristics

In chapter 3 an overview of the evolution of Sinlaku up to 19 September was given using ECMWF analyses and satellite imagery. Now the detailed structure of the core region of Sinlaku in the early hours of 19 September is investigated. After reintensifying to typhoon strength on the previous two days, Sinlaku is starting to experience the negative impact of environmental factors such as shear and dry air. The following detailed view of the 3D structure of the inner core convection of Sinlaku is provided by the SAMURAI analysis based primarily on airborne radar data. First of all, the radar reflectivity pattern is examined from the bottom up to get an impression of the structure of the core region. After that the wind field will be investigated in detail by looking at fields of horizontal wind speed, vorticity, vertical velocity and divergence.

Near the surface (at 1 km, Fig. 5.1(f)), a well developed, circularly shaped eyewall can be seen in the form of a ring of high reflectivity. This ring of high reflectivity encircles the eye which, as expected, has very low reflectivity values, in some areas even below zero. The location of the eye can be identified also according to the horizontal wind vectors, which show a strong cyclonic circulation around the center. The reflectivity exhibits distinct differences around the eyewall. The maximum values are located to the northeast of the center. A second reflectivity maximum can be seen to the northwest and a third weaker maximum almost south of the center. To the southeast there is a marked gap in the eyewall. In addition to these main features, there are further details to be noticed. Encircled by the flight track there are two regions with slightly increased reflectivities to the southeast of the center. They are located inside the eyewall ring. Moreover, there are also regions of higher reflectivities outside the ring of highest reflectivities to the east, the west and the southwest.
At 3 km (Fig. 5.1(e)), the ring structure of the eyewall is still clearly visible, with

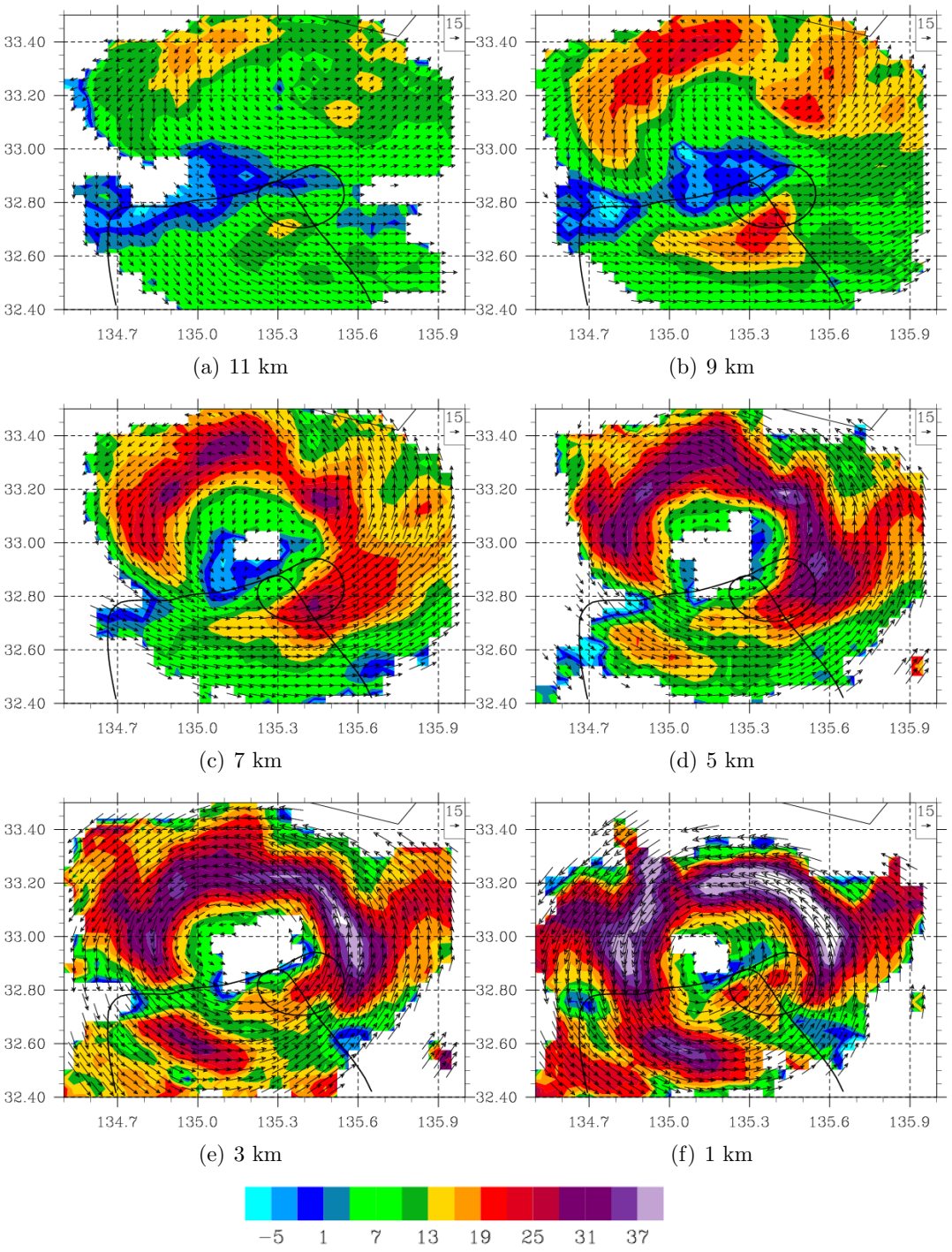

(a) 11 km (b) 9 km

(c) 7 km (d) 5 km

(e) 3 km (f) 1 km

Figure 5.1: Horizontal cross sections of radar reflectivity in dBz (shaded) and horizontal wind vectors at 11 km (a), 9 km (b), 7 km (c), 5 km (d), 3 km (e) and 1 km (f) with a horizontal resolution of 4 km. The reference vector is given in m s^{-1}. Grid points with no reflectivity data or values below 10 dBz are masked. The flight track of the P-3, carrying the ELDORA radar is marked with a black line.

the highest values to the northeast of the center and the gap to the southeast. The absolute values are smaller in general compared to the 1 km level. Moreover, an additional gap in the eyewall can be seen to the west, which separates the maximum to the southwest from the rest of the eyewall. The flight track shows that this is where the aircraft (flying at approximately 3 km altitude) was able to exit the eye again. The two regions with slightly increased reflectivities to the southeast at 1 km, that were encircled by the flight track, are now connected to the eastern part of the eyewall. The width of the ring of maximum reflectivities differs around the eyewall, with the narrowest distribution to the northeast. To the east and northwest there are again broad regions of higher reflectivities outside the ring of highest values. To the north, the region with reflectivities exceeding 19 dBz (red) broadens abruptly along the cyclonic flow at 135.3°E.

At 5 km, the region to the southwest, which is disconnected from the rest of the eyewall, is smaller in size in comparison to its extent at 3 km and the reflectivity values are decreased. Despite the fact that its position did not change significantly with height, the region to the southwest of the center looks to be located outside the ring of maximum values, and instead the region encircled by the flight track to the southeast appears to be included. The ring of highest values is rotated slightly clockwise or anti-cyclonically in comparison to the levels below. The gaps in the eyewall are now located to the south and the southwest. The part of the eyewall to the east of the center has broadened even further. To the northeast, the highest values of reflectivity on this level can be seen and the broadening of the region of values exceeding 19 dBz to the north is even more pronounced than 2 km below. In this location the wind vectors show that the circulation is not purely cyclonic anymore, but has a component directed outward.

At 7 km, the overall magnitude of reflectivity decreased in comparison to the level below. The region disconnected from the rest of the eyewall to the southwest has vanished and leaves a marked gap in the eyewall to the southwest. The rest of the eyewall can be partitioned into three regions with higher reflectivities. The broadest one is located to the southeast of the center, with its maximum located in the region encircled by the flight track. Its shape is not circular but rather rectangular when looking at the region of values exceeding 19 dBz (red). This is probably due to the structure of the horizontal winds. At this level the outflow is more pronounced and can be seen from the southeast to north-northwest of the system. The smallest region of higher reflectivities is located to the northeast of the center. Its maximum is located at the inner edge, with lower reflectivities reaching much further out ra-

dially. The third region of higher reflectivities covers the whole quadrant northwest of the center, with the maximum values to the north of the center. In comparison to the levels below, the location of the maximum values in this northern part of the eyewall is shifted northward. At 1 km at a longitude of 135.2°E the maximum reflectivity was located at 33.2°N, now it is at 33.35°N.
At 9 km, in addition to the gap in the eyewall to the south east, a second gap appears to the east. As at 7 km, the eyewall convection can be split up into three regions, One to the south, one to the northeast and one covering the northwestern quadrant. At this level all reflectivities are below 25 dBz.

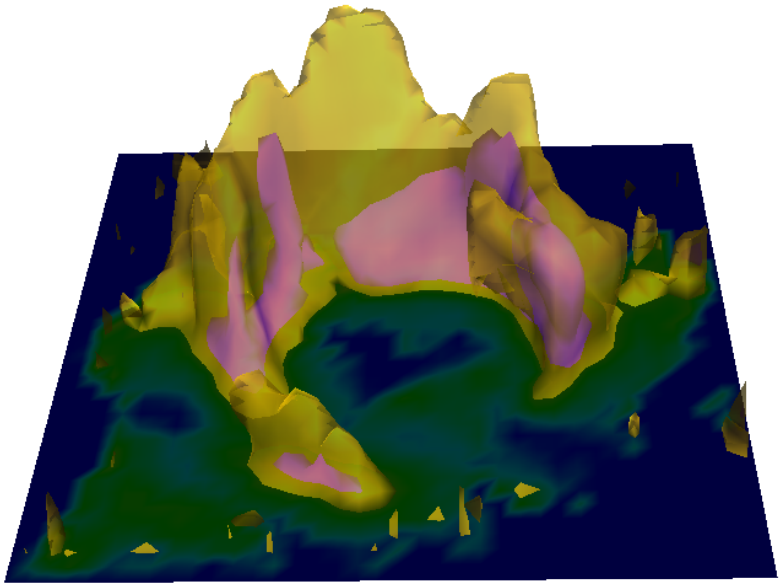

Figure 5.2: 3D radar reflectivity seen from the south. The 34 dBz surface is shown in magenta and the 26 dBz surface in yellow. The horizontal surface is at 1 km over the whole domain with the colors being reflectivity, blue values denote low reflectivities and green higher reflectivities.

At the uppermost level, at 11 km, almost the entire analysis domain has values below 13 dBz. Only one region to the northwest of the center exhibits values higher than 17 dBz. Thus the deepest convection of Sinlaku extends up to about this height.
In conclusion, the reflectivity pattern of the core region of Sinlaku exhibits a very complex structure, that also changes significantly with height, indicating different stages and intensities of convection around the eyewall. To get an impression of how the different horizontal levels link together, a 3D plot is shown in Fig. 5.2. Again the circular eyewall structure with the gap to southeast can be seen clearly. The gap

in the eyewall to the west, which separates the region to the southwest from the rest of the eyewall is hard to see from this point of view, but is there. As the horizontal cross sections showed, the northeastern quadrant of the eyewall had maximum values of reflectivity at lower to mid-levels. Thus the magenta 34-dBz surface is relatively broad. In the northeastern quadrant the magenta 34-dBz surface is mostly limited to the lower levels, with two almost vertically aligned peaks. This also suggests that the convection differs greatly around the eyewall, with a broad band of convection to the northeast and two isolated convective cells in the northwest. The yellow 26-dBz surface shows that the convection is deepest to the north as was also noticed in the horizontal cross sections at upper levels. Despite the fact that the higher reflectivity values (higher than 34 dBz) are most frequent to the northeast, the convection in this region is not that deep.
In stratiform precipitation, a bright band would be expected in the radar reflectivity below the melting level. Despite the fact that a tropical cyclone eyewall is mostly not made up of stratiform precipitation, a weak bright band can be identified at least partially in the raw data. Temperature soundings of the C-130 indicate that the melting level ranges between 4.6 and 5.8 km over the whole flight. The reason that no bright band can be established from the horizontal cross sections at these levels is probably that the vertical resolution of 500 m is too coarse to depict such a weak signal.

At the lowest level (1 km) the circular structure of the eyewall of Sinlaku seen in the reflectivity pattern is evident in the wind speed also (Fig. 5.3(f).) A strong cyclonic flow is apparent, which exhibits a ring structure. In the eye, the wind speed is near zero, but increases rapidly with radius. The highest wind speed is located in a ring around the center, with values exceeding 40 m s^{-1} everywhere around the eyewall except for a part to the south. To the south and east, the decrease of wind speed with radius can be seen at larger radii. In the vorticity (Fig. 5.4(f)), the strong cyclonic flow results in an extensive positive area centered around the eye. As for the wind speed pattern, the vorticity structure is also not completely rotationally symmetric, but rather elliptic. The magnitude of the vorticity decreases gradually with increasing radius, and becomes negative at large radii. This distribution can be explained by looking at the wind vectors and the wind speed. The wind vectors show that the circulation is cyclonic everywhere throughout the analysis domain, which results in a positive contribution to the vorticity everywhere. The total vorticity is a combination of this curvature vorticity and the shear vorticity, which in

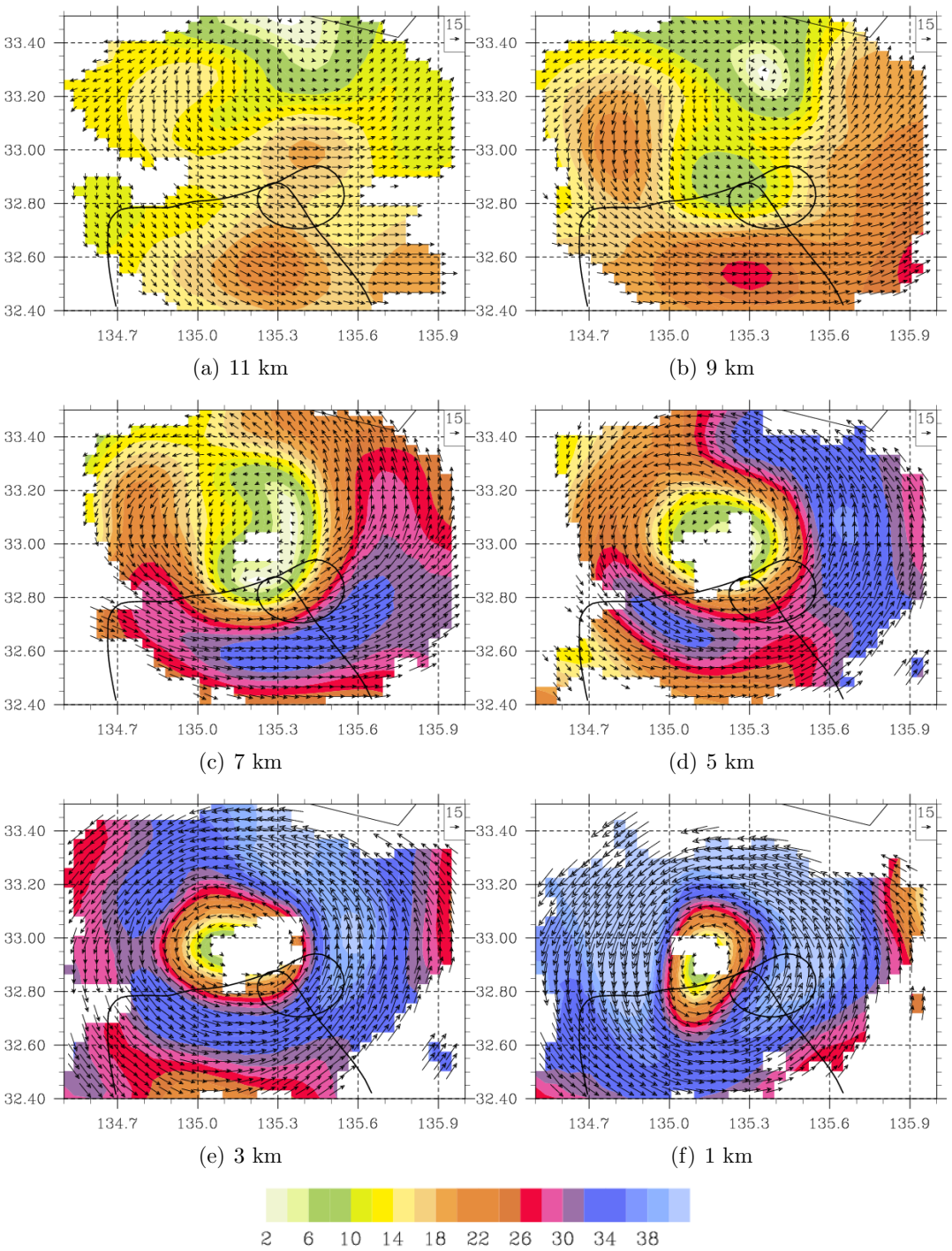

(a) 11 km (b) 9 km

(c) 7 km (d) 5 km

(e) 3 km (f) 1 km

Figure 5.3: Horizontal cross sections of horizontal wind speed in m s^{-1} (shaded) and horizontal wind vectors at 11 km (a), 9 km (b), 7 km (c), 5 km (d), 3 km (e) and 1 km (f) with a horizontal resolution of 4 km. For further information, see Fig. 5.1.

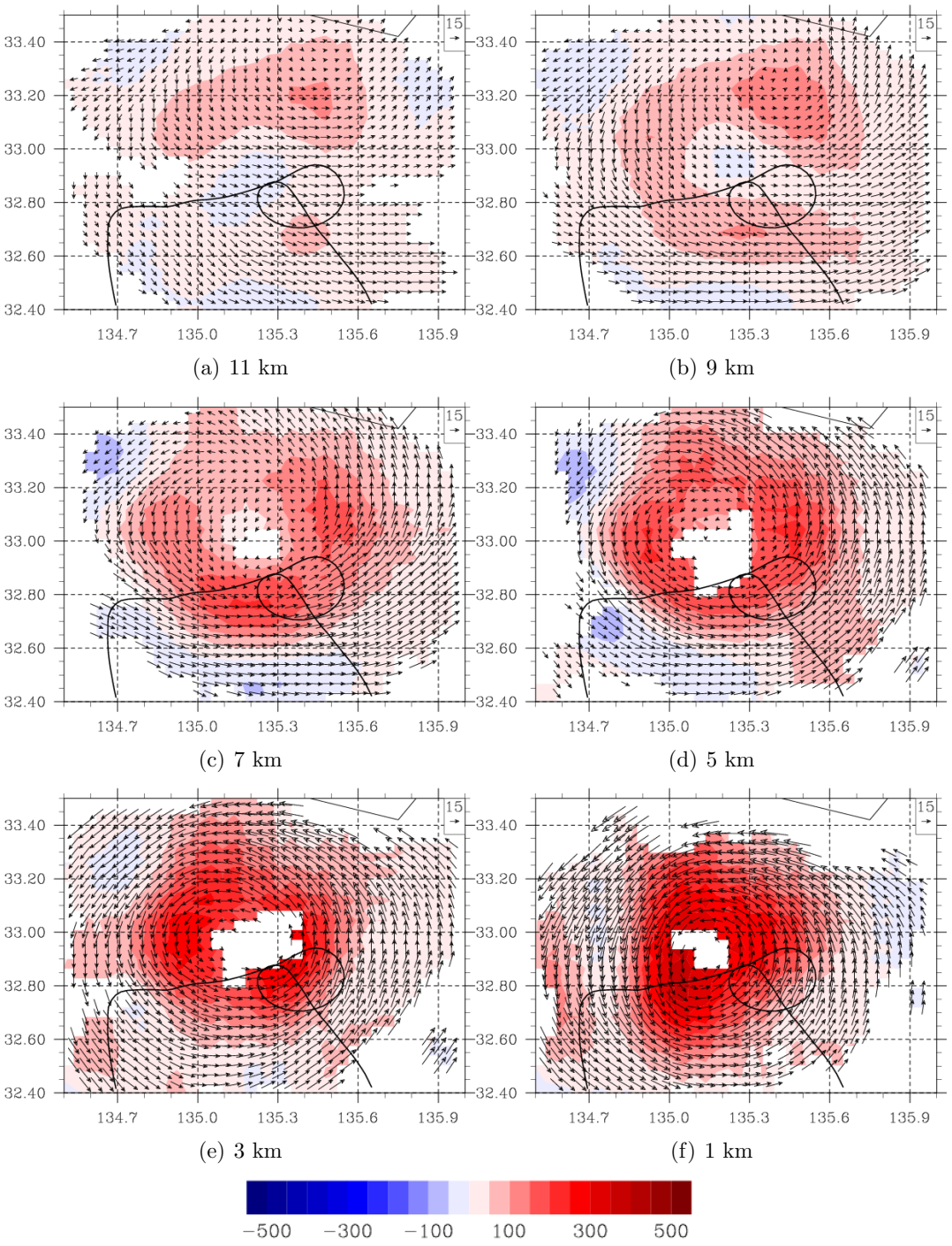

(a) 11 km (b) 9 km

(c) 7 km (d) 5 km

(e) 3 km (f) 1 km

Figure 5.4: Horizontal cross section of the vertical component of vorticity in 10^{-5} s^{-1} *(shaded) and horizontal wind vectors at 11 km (a), 9 km (b), 7 km (c), 5 km (d), 3 km (e) and 1 km (f) with a horizontal resolution of 4 km. For further information, see Fig. 5.1.*

turn originates from differences in wind speed between two adjacent wind vectors. This shear vorticity has positive values from the center of the eye out to the radius of maximum winds (RMW), because of the steady increase of wind speed. Outside the RMW, the wind speed decreases again, so the shear vorticity is negative. In summary, the total vorticity inside the RMW is definitely positive, because two positive values are added, but outside the RMW the sign of the total vorticity depends on the relative magnitudes of curvature and shear component.

At 3 km, the flow pattern is again purely cyclonic. In general, the wind speed is lower (Fig. 5.3(e)) than at 1 km. Values exceeding 40 m s^{-1} are limited to the quadrant northeast of the center, which is also the broadest region on high values. The area of values exceeding 32 m s^{-1} (blue) has a circular shape, indicating the location of the RMW. There is only a small gap in this annulus to the west showing that, in contrast to the level below, the minimum values within the RMW are now located to the west and not to the south of the center. To the north of the center there is a strong gradient in the wind speed along the direction of circulation. This gradient is followed by a small anomaly to the north northwest in the wind field at the inner edge of the blue annulus, denoted by purple colors, resulting in an outward shift for higher wind speeds. The vorticity structure at 3 km (Fig. 5.4(e)) is similar to the one 2 km below. A strong circularly shaped area with positive vorticity is centered around the eye. The absolute values are slightly smaller than at 1 km. Since the curvature is still strongly cyclonic everywhere, this change is probably due to the generally lower magnitudes of wind speed. The shape of this positive vorticity region is more symmetric and not as elliptical as at 1 km, which is also apparent in the wind speed plot. To the north of the center, where a small anomaly was apparent in the wind speed, the vorticity shows enhanced values stretching out to the border of the domain.

At 5 km, the wind vectors display a cyclonic circulation similar to the levels below, but the wind speed distribution (Fig. 5.3(d)) has changed. The wind speeds have decreased again in magnitude everywhere, but most noticeably to the northwest. This is now the region with lowest wind speeds around the eyewall, with values not exceeding 26 m s^{-1}. In contrast, the northeastern quadrant still exhibits values of over 36 m s^{-1} (blue). This results in a strong wind speed gradient to the north of the center. A slightly weaker gradient of wind speed is located to the southeast at the other end of the region of wind speeds exceeding 36 m s^{-1} (blue). Moreover, it can be seen that this blue area to the southeast does extend outward as far as data are available instead of exhibiting the more common structure that the wind

speed decreases with radius. In addition to the high wind speeds to the northeast, there is another maximum of wind speed located to the southwest. In the vorticity (Fig. 5.4(d)), the large area of positive values around the center is still broad, but now encircled by an area of negative vorticity to the west. There is an additional band of positive vorticity to the southwest of the center outside the main area of positive vorticity. Its location coincides with the region of strong gradient in wind speed (which can be seen easily by taking the flight track for orientation). The anomaly of higher values to the north, that was seen at the level below, still exists. At 7 km, the circulation is still cyclonic everywhere, but displays more structural variation. The maximum wind speeds at 7 km are to the south and east of the center, with the region to the southwest having values even higher than on the level below. The ring structure in the wind speed (Fig. 5.3(c)) with low values in the center, increasing with radius up to the radius of maximum winds and then decreasing again is still evident in the southern and eastern part of the eyewall, but to the northwest no radius with distinct maximum values of wind speed can be seen. Instead the area of lower wind speed values elongated very far north. The wind vectors in this area also exhibit a departure from the typical cyclonic flow (which can be best seen in Fig. 5.4(c)). In an area between 135.0°E and 135.3°E the flow south of 33.25°N is almost purely northerly and the flow to the north of 33.25°N is southeasterly, which results in a divergent structure. The departure from the strong cyclonic flow to the north, is seen as lower values of vorticity (Fig. 5.4(c)). In general, the vorticity pattern exhibits a ring structure with maxima to the south and east and, as just mentioned, a gap to the north. To the west the positive values are again surrounded by negative ones. The wind vectors in this region differ from the ones at the level below. They shifted from south-southwesterlies to southwesterlies, and thus are not directed cyclonically around the center but more outside of the domain. The same structure can be seen to the north-northeast also, where the direction of the wind vectors again is shifted clockwise in contrast to the ones at 5 km and thus away from the center.

At 9 km, only remnants of the ring structure in the wind speed are visible (Fig. 5.3(b)). The maximum values have decreased to below 28 m s^{-1} and are mostly located to the south and east, with an additional smaller region to the west. The low values are not confined to the region around the center anymore, but another minimum with even lower wind speeds is located to the north. This area to the north is also interesting with regard to the direction of the wind vectors, because they show that this area is encircled by cyclonic flow. In turn, the region where the eye was located

at lower levels is now dominated by northwesterly to westerly flow. The only part of the eyewall that exhibits the same flow direction as the lower levels (1-5 km) is the southwestern quadrant. In the southeastern part, the flow is mostly westerly and does not show strong curvature. To the eastern side, the wind vectors point predominantly to the east and not to the north as at lower levels, which indicates outflow out of the system. Thus, the flow at this level is a combination of environmental almost westerly flow and remnants of the tropical cyclone circulation. In the vorticity (Fig. 5.4(b)), the ring structure of positive vorticity can still be seen, but in general with lower values. This time, the gap in the ring is to the east and not to the north. In this region, the flow is purely westerly. The cyclonically encircled region of low wind speeds to the northeast results in a maximum of vorticity. In the middle of the ring of positive vorticity, the vorticity reaches negative values. To the west of the positive vorticity ring the typical pattern with negative values surrounding the ring can be seen as in the two levels below.

At the uppermost level (11 km), the magnitude of the wind speed decreases further (Fig. 5.3(a)). The lowest values are located to the north of the domain and the highest values to the south of the domain. The northern half of the domain still exhibits cyclonic flow, whereas the southern half is dominated by westerly flow. In the vorticity (Fig. 5.4(a)), only the northern part of the vorticity ring remained, with the maximum values occurring to the northeast, as at the level below. The rest of the domain exhibits very small values of vorticity.

In summary, the wind speed and vorticity shows that up to at least 7 km the Sinlaku has a strong cyclonic circulation. Above this height, the flow in the southern part becomes mostly westerly and to the northeast a smaller-scale region of cyclonic flow appears. The wind speeds differ significantly around the eyewall with the highest values mostly to the southeast and northeast.

After this overview of the structure of both reflectivity and horizontal winds, the link between those two is now considered. From lower to mid-levels the wind speeds have high values in the northeastern quadrant, coinciding with the broad region of high reflectivities in this quadrant. At upper levels (above 7 km), this wind speed maximum shifts to the south, where also a region of high reflectivities is located. In contrast, the convection to the northeast is accompanied with reduced values of wind speed. At 9 km, the smaller scale cyclonic circulation to the north or north-northeast is located in the vicinity of the area of higher reflectivities.

The hydrometeors that provide the reflectivity information are of course advected around the tropical cyclone by the horizontal flow. The distance of advection de-

pends on the horizontal wind speed, but also on the vertical velocity. For example, this advection effect can be seen very well in the layer between 5 and 7 km height to the southeast of the center. This is a layer with high wind speeds and a broad region of reflectivity. By comparing the reflectivity patterns of 7 and 5 km in this region, it is evident that there is a cyclonic shift in the reflectivity from the higher to the lower level. This indicates, that falling hydrometeors have been advected downstream with the cyclonic circulation. Thus, by looking at the reflectivity and horizontal wind patterns, conclusions about the vertical velocity can be drawn also. If the vertical air motion would be positive and higher than the fall speed of the particles, the shift in the reflectivity would have been anti-cyclonic.

This method would be rather painful and very inaccurate to determine the vertical velocity. Fortunately, the vertical velocity is part of the data set provided by the analysis and will be examined in the following. As mentioned in chapter 4, the vertical velocity is examined using the SAMURAI analysis with a horizontal resolution of 1 km, instead of the resolution of 4 km that was used so far in this chapter. Recall that the interpretation should concentrate on the spatial pattern and not on the absolute values.

Three features dominate the vertical velocity pattern: a broad region of ascent to the east of the center, a region of ascent flanked by two regions of descent to the northwest and a region exhibiting a very diverse pattern of alternating up- and downdrafts to the southwest.

More precisely, the region of broad ascent extends from the straight leg of the flight track in the southeast to the north of the center. At 1 km (Fig. 5.5(f)), the vertical velocities have low values, with a pattern of small regions of up- and downward motion located next to each other to the southeast and a broad region of upward motion only interrupted by one small region of downward motion in the northeastern quadrant. At 3 km (Fig. 5.5(e)) the magnitude of vertical velocities increases and the region is covered almost entirely by positive values. The maximum values are located inside the area encircled by the flight track. These high values can be assigned partly to inaccuracies in the analysis (see chapter 4). But since the radar reflectivity exhibits areas of enhanced values in this region also, it is probably not purely an analysis inaccuracy. At 5 km (Fig. 5.5(d)), the pattern is similar to the one on the level below. The whole eastern edge of the eyewall exhibits upward motion and the maximum values are encircled by the flight track. An additional weaker maximum can be seen at the inner part of the eyewall just north of the flight track

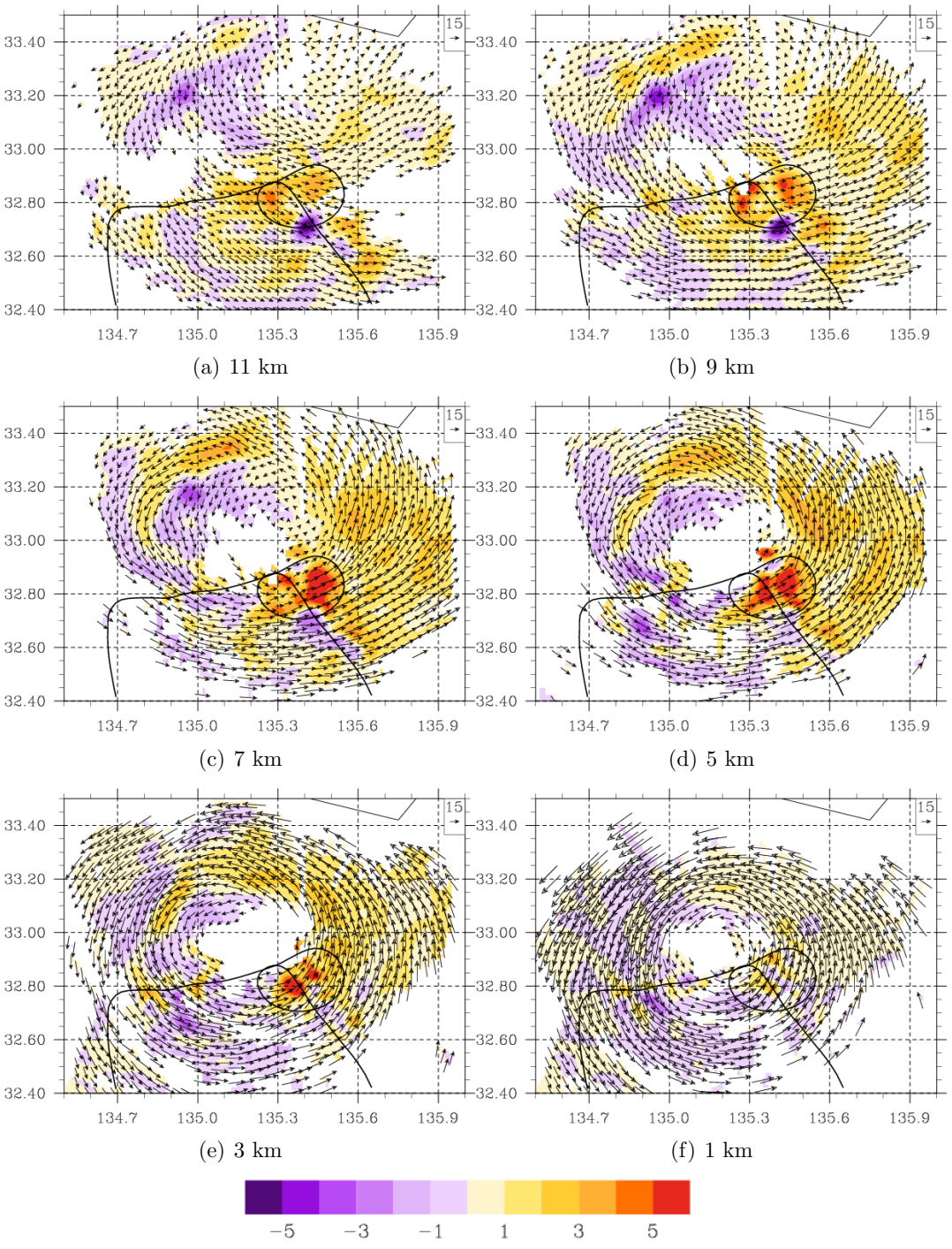

(a) 11 km (b) 9 km

(c) 7 km (d) 5 km

(e) 3 km (f) 1 km

Figure 5.5: Horizontal cross section of the vertical velocity in m s^{-1} (shaded) and horizontal wind vectors at 11 km (a), 9 km (b), 7 km (c), 5 km (d), 3 km (e) and 1 km (f) with a horizontal resolution of 1 km. For further information, see Fig. 5.1.

circle. In comparison to the level below, the overall magnitudes of the positive values have increased slightly. Two kilometers higher, at 7 km (Fig. 5.5(c)), this part of the eyewall still exhibits a broad region of ascent without any embedded regions of downward motion. The magnitude of the vertical motion is comparable to the magnitude at the level below. At 9 km (Fig. 5.5(b)), the vertical velocities again begin to decrease, but still there are no negative values apparent. This changes slightly at the uppermost level (Fig. 5.5(a)), with three or four small regions of downward motion, but still the general feature is upward motion. Thus, a few small regions of downward motion can be seen only at the lowest and the highest levels. Otherwise, the eastern edge of the eyewall is governed by broad ascent throughout the entire area.

Next, the vertical velocity in the area of the region of ascent flanked by two regions of descent to the northwest is investigated. At 1 km, the velocities in general are weak. The area is covered slightly more by downward motion than by upward motion. In contrast to the eastern part of the eyewall, where the downdraft regions were very small in scale, in this part of the eyewall the areas of both positive and negative velocities are broader. At 3 km, there is a broad region of ascent to the north flanked by downward motion both at larger and smaller radii. This pattern continues round to the northwest, but there the area of positive values is much narrower. At very large radii the vertical velocity becomes positive again. At 5 and 7 km, the region of downward motion at the outer edge of the upward motion has vanished to the north of the center, but to the northwest the band structure of two descent and one ascent region still exists. This structure also continues at 7 km. The region of descent at the inner edge of the ascent region increases in size with height. At 7 km, this descent region exhibits a minimum with values lower than -2 m s^{-1}. To the northeast of this minimum, there is a maximum ascent within in the band of upward motion. At 9 km, the outer band of negative velocities can not be seen anymore. North of the center the region of downward motion has extended further to the north and to the west at 33.0°N, the region of downward motion covers all radii. Since the horizontal circulation is not exactly circular anymore at this level, the structure of the upward- and downward couplet is also more parallel and not that curved anymore. At 11 km, the couplet structure does exist still, but with smaller magnitudes. Hence, this quadrant exhibits a very interesting vertical velocity pattern consisting of a band of positive vertical velocities at most levels, flanked by two regions of negative vertical velocities.

The third region that will be examined is the quadrant to the southwest of the cen-

ter. At 1 km, the regions of descent dominate, but the structure is very complex. To the southwest of the center, small regions of positive vertical velocities alternate with small regions of negative vertical velocities. To the south a broader region of descent can be seen. At 3 km, the pattern is very similar to the level below, but the magnitudes of the vertical velocity are larger for both ascent and descent. At 5 km, the magnitudes of the vertical velocities increase further. At lower levels the region to the south is dominated by descent, now this area exhibits ascent surrounded by descent. At 7 km, the pattern changes further from smaller to broader regions of positive and negative velocities. To the south-southwest of the center, the region of positive values is accompanied by negative values to the inner and outer edge of it and to the southwest the band of negative values connects with the outer band of descent from the northwestern quadrant. Ascent is more dominant at this level than lower down and the magnitudes of vertical velocities decreased again in comparison to the level below. At 9 km, the magnitudes decrease further, but the pattern is similar to 7 km, with a broad region of positive values to the south, and a more diverse pattern to the southwest. At the uppermost level (11 km), the southwestern quadrants exhibits more areas of upward than downward motion. The areas of negative values consist of a few small regions, one broader region to the southwest and one to the southern edge of the analysis domain. Thus, this region of the eyewall exhibits the most complex structure of vertical velocities with regions of descent alternating with regions of ascent. At lower levels the downward motion accounts for the larger fraction of the area and at upper levels the upward motion.
In summary, the investigation of the vertical velocity around the eyewall showed very different characteristics. At the eastern edge of the eyewall, a broad region of ascent can be seen covering all levels. To the northwest, a band of positive vertical velocities is surrounded by two bands of negative vertical velocities throughout all heights. To the southwest, a very diverse pattern of alternating up- and downward motion was found. In all quadrants, the highest magnitudes of vertical velocity occur at midlevels. The broad ascent to the east matches with the region of highest radar reflectivities. The southwestern quadrant with a lot of downward motion, coincides with the quadrant where the radar reflectivities reach up to only 5 to 7 km.

To further establish a 3D picture of the structure of Sinlaku, vertical cross sections are examined. The locations of the cross sections are marked in Fig. 5.6. They all cut through the center of Sinlaku and are located 45° apart from each other. Cutting through the ascent region to the east of the center (righthand side of Fig. 5.7(a))

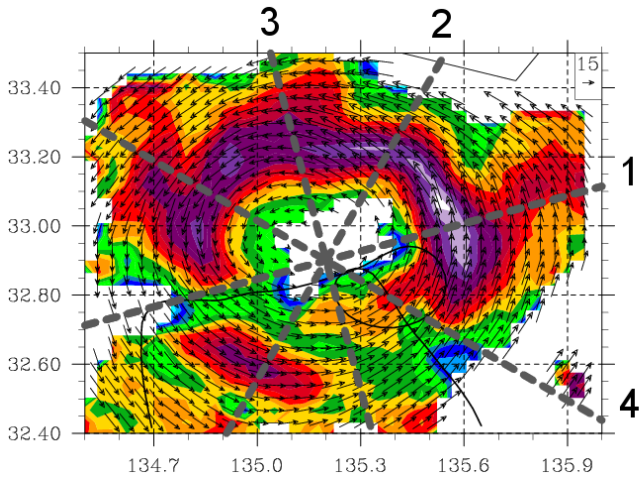

Figure 5.6: Location of the cross sections shown in Fig. 5.7 and Fig. 5.8, plotted on top of the horizontal cross section of reflectivity at 3 km (Fig. 5.1(e)). Cross section 1 is parallel to the shear vector and cross section 3 is perpendicular to it.

shows a broad region of higher reflectivities with values exceeding 13 dBz at almost all radii from 1 to 8 km height. The maximum values are located in the inner third of this broad region. At levels above 9 km a uniform region of low reflectivities in displayed. Thus, the convection is very strong at lower levels, but is not very deep. The wind vectors exhibit a flow pattern, that is typical for tropical cyclones. At lower levels up to 2 km, there is radial inflow, which then rises in the region of highest convection, i.e. highest reflectivities and flows radially outward at the top of the convection. This outflow layer is located between 7 and 10 km height. Above the outflow layer, weaker flow is directed outward as well, which presumably represents the environmental westerly flow. In the center, where no reflectivity is apparent, the wind vectors are not zero, but show outward motion, which is most pronounced at heights of 2 to 6 km.

In the vorticity (righthand side of Fig. 5.7(b)), the maximum values can be seen at lower levels to the center of Sinlaku. Above 2 km, the maximum shifts outward with height and the area covered by vorticity exceeding 10^{-3} s^{-1} broadens up to 8 km. Above 10 km the vorticity is almost zero. The tangential winds show a distinct radius of maximum winds at 2 km height and an outward slope of the isotachs with height at the inner edge of the eyewall that is similar to the slope of maximum vorticity with height. The isotachs also follow the distribution of the wind vectors and thus their slope is considered to illustrate the conservation of angular momentum.

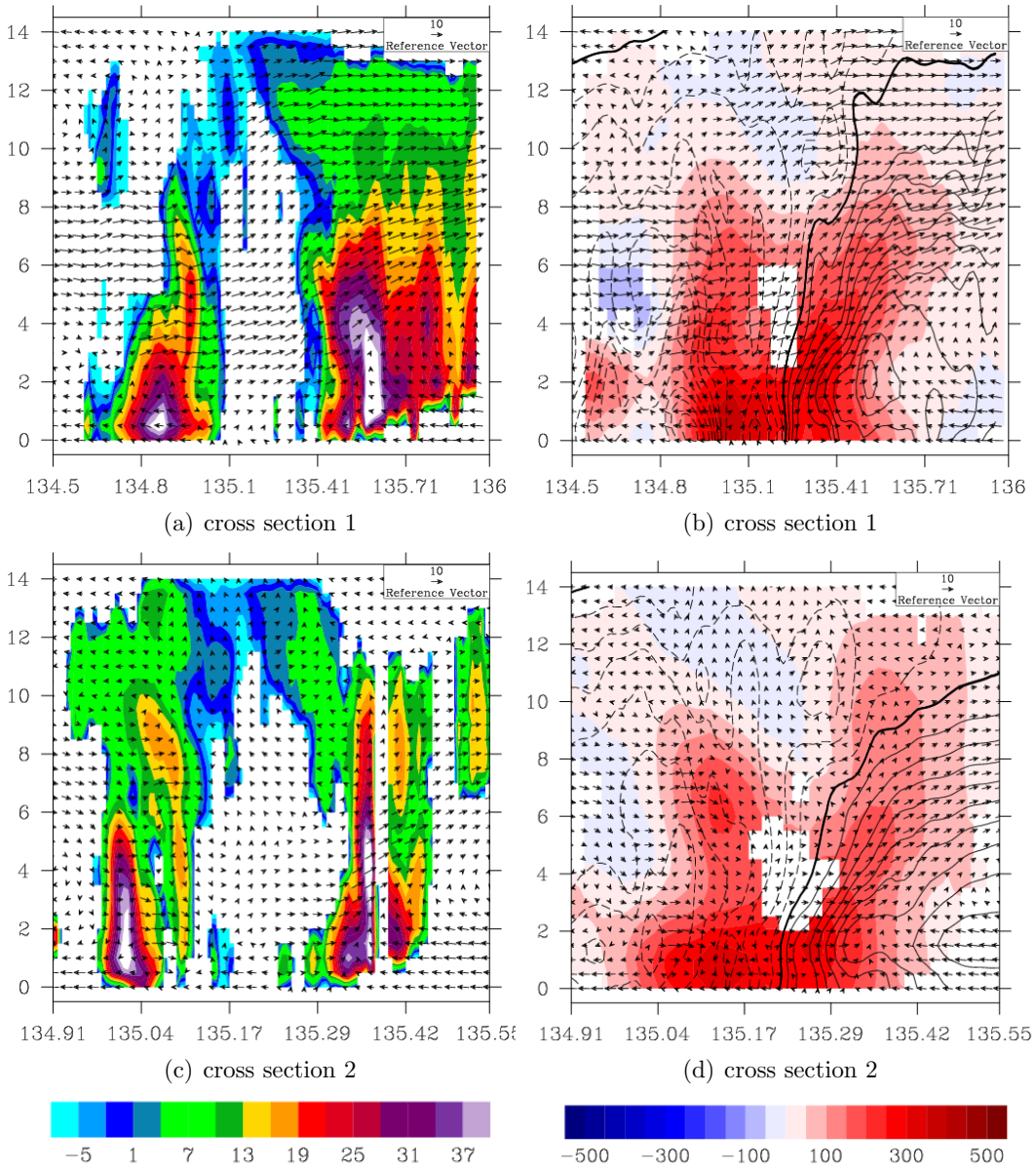

(a) cross section 1

(b) cross section 1

(c) cross section 2

(d) cross section 2

Figure 5.7: (a) and (c): Cross sections of reflectivity in dBz (shaded) and wind vectors composed of vertical velocity and the in-plane component of horizontal velocity. The reference vector is in m s^{-1}. The horizontal resolution of the analysis is 1 km. (b) and (d): cross sections of vorticity in 10^5 s^{-1} (shaded), tangential wind speed (contoured in intervals of 5 m s^{-1}, the bold solid line denotes zero, solide lines represent positive and dashed lines negative values) and wind vectors. The horizontal resolution for velocity and reflectivity is 1 km and for vorticity 4 km. The wind field is not masked.
The westernmost point of the cross section is on the left and the easternmost point to the right of the plot.

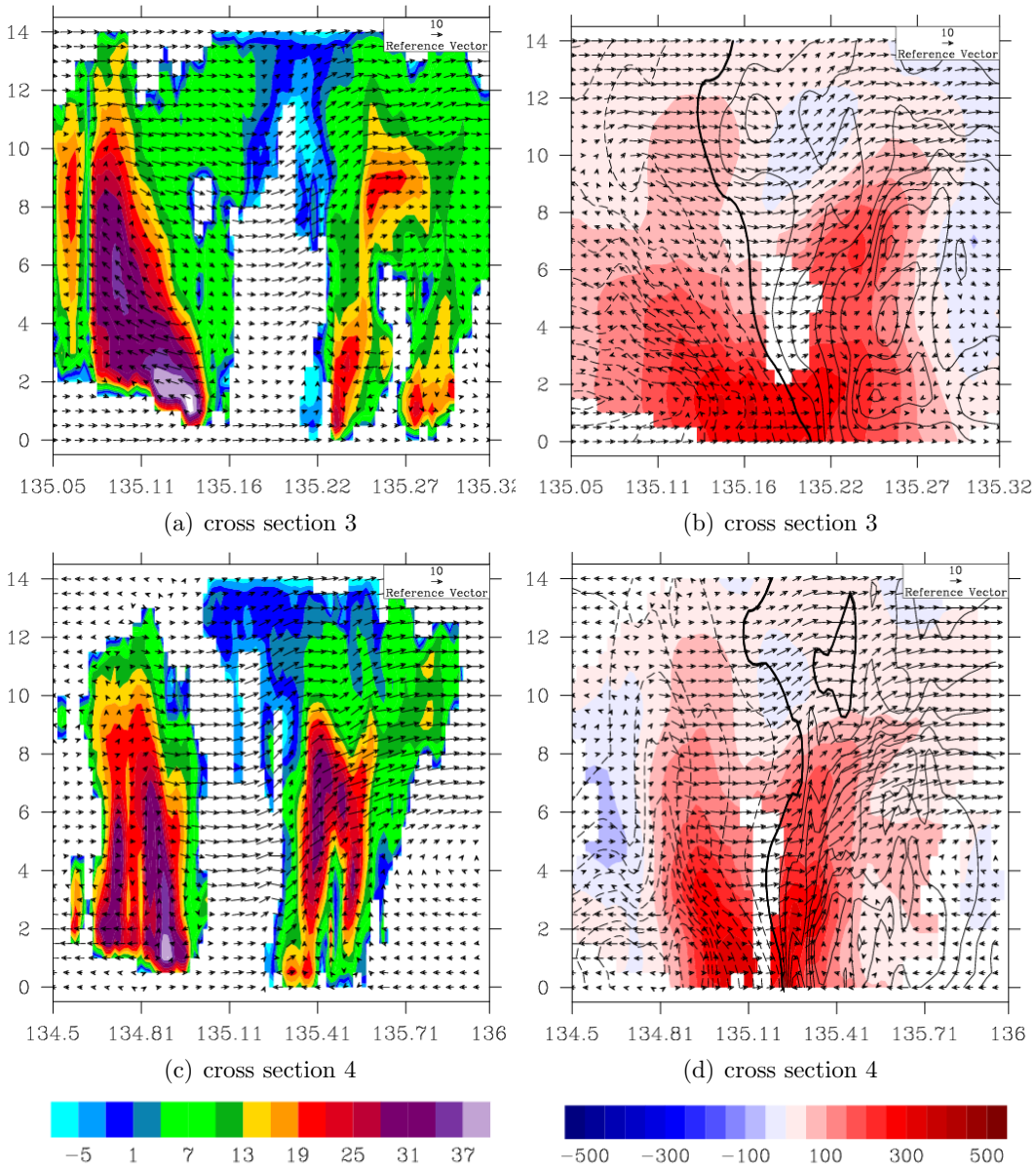

(a) cross section 3

(b) cross section 3

(c) cross section 4

(d) cross section 4

Figure 5.8: (a) and (c): Cross sections of reflectivity in dBz (shaded) and wind vectors composed of vertical velocity and the in-plane component of horizontal velocity. The reference vector is in m s^{-1}. The horizontal resolution of the analysis is 1 km. (b) and (d): cross sections of vorticity in 10^5 s^{-1} (shaded), tangential wind speed (contoured in intervals of 5 m s^{-1}, the bold solid line denotes zero, solid lines represent positive and dashed lines negative values) and wind vectors. The horizontal resolution for velocity and reflectivity is 1 km and for vorticity 4 km. The wind field is not masked.
The westernmost point of the cross section is on the left and the easternmost point to the right of the plot.

In summary, this cross section to the east displays typical characteristics of eyewall convection, with inflow at lower levels, upward motion in the eyewall with conserved angular momentum and outflow at upper levels. In contrast to a mature hurricane in the deep tropics, the convection of Sinlaku at this stage of its life cycle is not that deep anymore, with a height of approximately 8 km.
The next cross section (righthand side of Fig. 5.7(c)) cuts through a narrower part of convection to the northeast. The reflectivity still exhibits values of more than 40 dBz up to heights of 5 km and values of more than 13 dBz up to 10 km, but the radial extent is much narrower than in the cross section discussed previously. The wind vectors display inflow at lower levels up to 3 km, upward motion in the region of high reflectivities and outflow above. In contrast to the previous cross section, the wind speeds of the outflow are not as high. Moreover, in the previous cross section the outflow started at levels above the maximum reflectivities (white) and now the outflow starts at levels within the maximum reflectivities and at the levels above no distinct outflow can be seen.
The vorticity (righthand side of Fig. 5.7(d)) is much deeper for weak positive vorticity values than in the previous cross section. At levels below 6 km, the location of the maximum vorticity shifts outward with height, but above this height the vorticity is vertically aligned. The maximum in tangential winds is located at around 2 km at the edge of the domain. The slope of the isotachs is weaker than in the previous cross section and the zero line indicates that the flow at upper levels is directed weakly in the opposite direction. Thus, the area covered with convection in this cross section is smaller than in the previous one, but the vorticity is deeper. A typical flow pattern can be seen, which a sloped updraft to conserve angular momentum and the maximum tangential winds are located at low levels and large radii.
Cross section 3 cuts through the region, that showed an area of upward motion flanked by two areas of downward motion. In the reflectivity (lefthand side of Fig. 5.8(a)), a broad region of convection can be seen. The separation into two regions of higher values divided by a vertical line of lower (green) values, originates from interpolation over an area with no data coverage and is not physical. The maximum values of reflectivity are located at 1 km to the inner edge of the region. Another slightly weaker maximum can be seen at 6 km height. The isolines of reflectivity at the inner edge of the eyewall are all sloped outward with height. Reflectivities exceeding 16 dBz reach up to 11 km, which is higher than in the two previous cross sections. The wind vectors exhibit inflow at lower levels, but no distinct region of updraft at the inner edge of the eyewall, where the maximum reflectivities occur.

Outward motion already begins at 2 km height, but while moving outward, the vertical wind component increases and the in-plane component decreases. Hence, e.g. in the region of maximum reflectivities at 8 km height, the wind vector points almost vertically. This upward motion in the region of maximum reflectivities can be seen up to 10 km. Above this height, the wind vectors turn inward and subsidence at the inner flank of the eyewall convection is evident. At lower levels the wind vectors turn outward again, indicating intrusion into the eyewall. This pattern illustrates the structure of vertical velocity, that was shown in the horizontal cross sections: a broad region of ascent is accompanied by descent at its inner edge and thus forms a circulation. In the vorticity (lefthand side of Fig. 5.8(b)), the distribution differs for levels below and above 6 km. Below 6 km, the maximum shifts outward with height whereas above the vorticity is vertically aligned. The maximum tangential winds are again located at low levels at the edge of the domain and its isolines at the inner edge exhibit a slope that is similar to the one in vorticity. Hence, one difference of this cross section to the two previous ones is the structure of the radial flow. They do not exhibit pronounced outflow at mid- to upper levels but instead an ascent-descent couplet. Weak outflow is located between 2 to 7 km. Another difference is the uniform slope of the isolines of reflectivity with height.

The next cross section cuts through the northwestern part of the eyewall. In the reflectivity (lefthand side of Fig. 5.8(c)), two adjacent vertically aligned regions of maximum reflectivity can be seen. The inner region exhibits its highest values at the bottom, but does not reach 40 dBz, in contrast to the previous cross sections. Values exceeding 13 dBz (yellow) are found up to heights of 10 km, which is slightly lower than in the cross section to the north of the center. The radial wind speeds are relatively small and the wind vectors exhibit a pattern that deviates from the expected flow pattern for a tropical cyclone. At low levels around 1 to 3 km height, there is outflow instead of inflow. In contrast, there is inflow at around 6 km, followed by weak descent in between the two reflectivity towers. Weak ascent occurs up to 10 km in the region of maximum reflectivity. The highest wind speeds occur in descent at the inner edge of the eyewall at 8 to 10 km. This descent can be seen at the inner edge of the eyewall down to 4 km. Weak outward motion into the region of maximum reflectivity is apparent below 4 km. Thus, the flow pattern of upward motion in the region of high reflectivities and downward motion at the inner edge of the eyewall is in general similar to the flow pattern to the north of the center, but the wind speed is much weaker and the flow in the lower levels changed from in- to outflow.

A vertically aligned tower of positive vorticity values can be seen, which is located at the inner part of the eyewall with its highest values at the bottom (lefthand side of Fig. 5.8(d)). At the outer part of the domain a region of negative vorticity can be seen with maximum values centered around a height of 6 km. The tangential winds exhibit a very interesting structure. The isotachs are bent upward strongly in the transitional region from positive to negative vorticities, which also coincides with the region of high reflectivities. Thus, the maximum of tangential wind for each level is located in this column. This feature suggests an upward flux of horizontal momentum within the convection. Thus, this cross section exhibits a few features that were not apparent in the previous cross sections.

The second part of cross section 1 cuts through the eyewall to the west of the center, slightly north of the gap in reflectivity. The main part of the reflectivity is confined to levels below 4 km (lefthand side of Fig. 5.7(a)). Only one narrow band at the inner edge extends to 7 km. The inflow region at the outer edge of the domain is located at 4 to 8 km height, which could be due to environmental flow. This inflowing air then ascends slightly, followed by upward motion at the top of the narrow band of maximum reflectivity and downward motion within the band. There is outflow at the outer edge of the domain below 2 km, and a clockwise circulation is visible within the main region of reflectivity, consisting of outward motion at lower levels, upward motion at the outer edge of the main region and inward flow at around 4 km. The vorticity (lefthand side of Fig. 5.7(b)) exhibits an upright tower of positive values at the inner region of the eyewall. Its vertical extent has decreased in comparison to the previous cross section. A region of negative vorticity is again located at the outer edge of the positive tower at around 5 to 6 km, this time accompanied by a region of positive vorticity below. The tangential winds exhibit upward bent isotachs as in the previous cross section, but this time not as pronounced. They are located at the outer edge of the domain and at the outer edge of the tower of positive vorticity, which coincides with the region of maximum reflectivities. Hence, this cross section displays the shallowest reflectivity pattern so far, but some of the flow characteristics also found in the previous cross section are still seen.

The next cross section cuts through the region of maximum reflectivities to the southwest, that is disconnected from the rest of the eyewall. This region can be seen in form of a vertically aligned area of maximum reflectivities with values exceeding 40 dBz (white) throughout the lowest 3 km (lefthand side of Fig. 5.7(c)). It is accompanied by a deeper region of low reflectivities toward smaller radii. The inflow is located at levels between 6 to 8 km, and the lowest levels exhibit outflow.

The region of maximum reflectivity is dominated by inward flow with components of descent at both its outer and inner edge. At 8 to 9 km, the maximum of reflectivity is surrounded by a weak anticlockwise circulation. At 8 km there is inflow, followed by weak upward motion at the inner edge of the reflectivity maximum, outward flow above the maximum and weak descent at the outer edge. Below, there is descent in most of the narrow band of reflectivity.
The vorticity (lefthand side of Fig. 5.7(d)) shows a broad distribution of positive values up to 3 km and above slightly outward shifted tower. The maximum values are located primarily at the bottom, with another maximum at 6 to 7 km. The midlevel maximum is located slightly below and slightly inward of the maximum of reflectivity. The tangential wind has its highest values at levels up to 2 km at the outer half of the domain, reaching up to around 5 km at the inner part of this region. The location of the maximum of tangential wind coincides with the maximum values of reflectivity.
The southern part of cross section 3 cuts through the southern part of the eyewall. The reflectivity (righthand side of Fig. 5.8(a)) shows that the two reflectivity regions identified in the last cross section developed differently in terms of the intensity. Note, that the southern part of the eyewall is on the left of Fig. 5.7(c) but in the right of Fig. 5.8(a). The outer region decayed and thus the magnitude and vertical extent of reflectivity decreased significantly. In contrast, the inner region developed and exhibits higher values of reflectivity both at the bottom and at around 9 km. The inplane winds at low levels are relatively weak in the region of the decaying convection. At the location of the lower level reflectivity maximum on the inner convection, there is a region of convergence with wind vectors pointing inward from the outside and wind vectors pointing out- and downward from the inside at 2 to 4 km. Above this layer, there is ascent in the region of the maximum reflectivity and outward motion to larger radii. The location of the highest radial wind speeds coincides with the location of the maximum reflectivities at 9 to 10 km. Thus a typical outflow pattern at heights of 7 to 10 km can be seen in this cross section again. The maximum of vorticity (righthand side of Fig. 5.8(b)) at lower levels up to 4 km is tilted outward, then from 4 to 6 km is mostly constant with height and tilts outward again at levels above 6 km with a slope almost parallel to the inplane winds. The greatest magnitudes are found at low levels and another maximum is located between 6 and 7 km, whose location again is slightly outward and below the maximum in reflectivity. The highest tangential winds occur at the outer edge of the positive vorticity tower and at 8 to 10 at the outer edge of the domain the

isotachs are approximately parallel to the inplane winds.
The last cross section cuts through the eyewall to the southeast of the center. Here, the reflectivity (righthand side of Fig. 5.8(c)) again exhibits values exceeding 28 dBz. There are two adjacent main columns of high reflectivities, which are connected at their tops. The flow pattern is again more typical for a tropical cyclone. At levels up to 3 km, there is weak inflow, and in the region of the inner high reflectivity column strong ascent occurs, which is also supported by flow from within the eyewall. The ascent reaches up to the top of the convective column and shifts gradually outward with height. At the location of the outer column of high reflectivities the wind vectors point mostly outward and only weakly upward, indicating that this column consists mainly of falling particles that originated in the inner column and were advected outward at levels around 5 to 8 km. The outflow covers a large range of heights. At the outer edge of the domain, this is 6 to 12 km. Thus, this cross section exhibits a similar flow pattern to the one, that was examined in the first cross section and shows that the cycle is almost completed now. In the vorticity (righthand side of Fig. 5.8(d)), a narrow, vertically aligned tower of positive vorticity can be seen, which tilts outward at the top. following the inplane wind vectors. The isotachs of the tangential wind also mostly follow the inplane wind vectors at the inner edge of the eyewall and in the outflow region.
In summary, the cross sections showed the very diverse structure of the eyewall in reflectivity, vorticity and winds. To the east and northeast, the reflectivity patterns were mostly upright and the winds exhibited the typical in-up-and-out flow pattern with the isotachs of tangential winds being sloped outward to conserve angular momentum. In the other cross sections the structure was more complex with features such as decaying and developing convection, outward sloped reflectivity patterns, inflow at midlevels or descent at the inner edge of the eyewall.

The region encircled by the flight track to the southeast will be excluded from the following investigation of divergence, because the magnitude of vertical velocity is supposed to have deviations from the true state there, which subsequently leads to errors in the divergence.
In the region of broad ascent to the northeast of the center, the divergence is mostly determined by in- and outflow. The strong inflow, that was seen in the cross sections in this region, results in a broad region of convergence at lower levels (Fig. 5.9(f), Fig. 5.9(e)). Adjacent to this convergent region is a divergence region at smaller radii, which represents the ascent in the eyewall. This area of convergence broadens

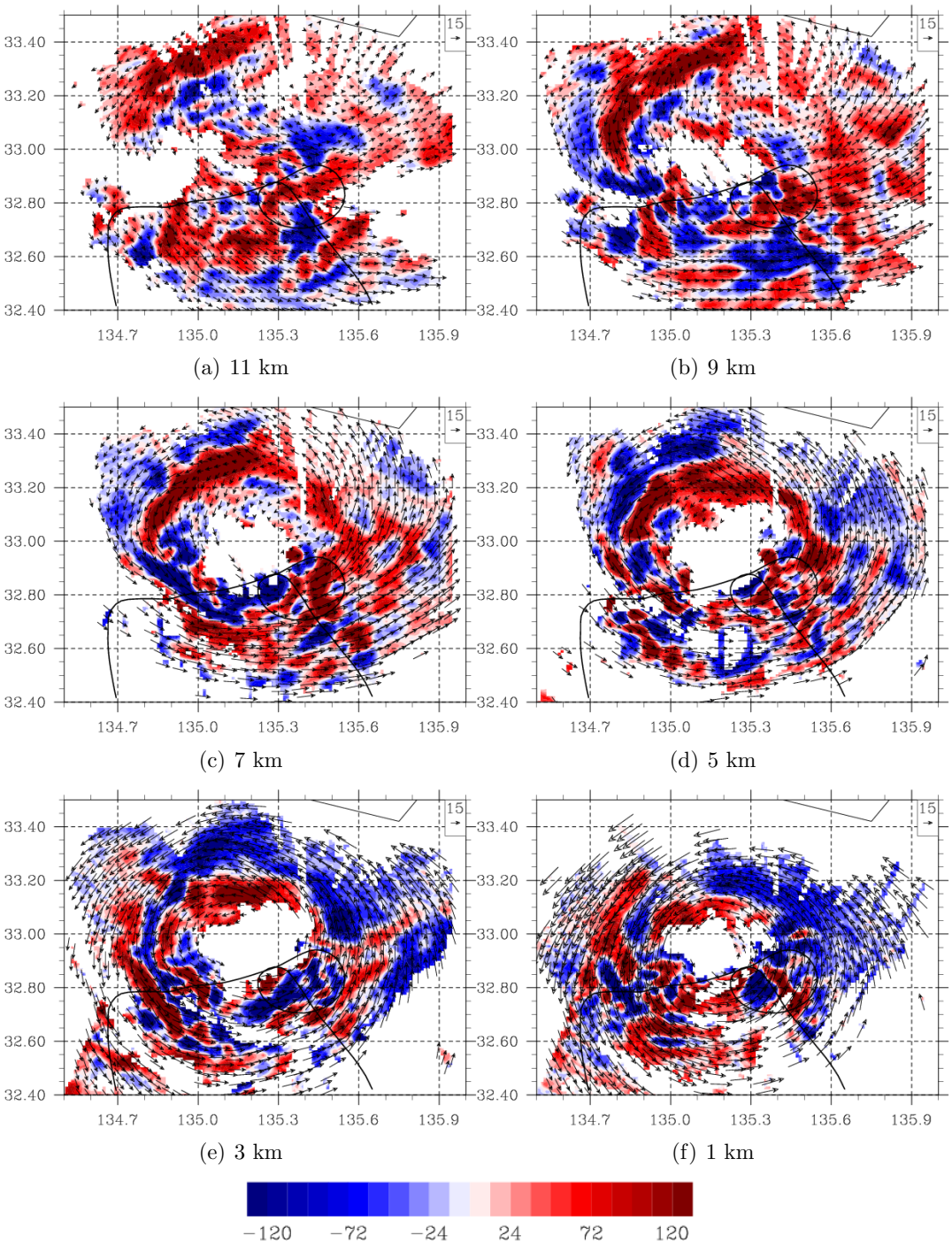

(a) 11 km (b) 9 km

(c) 7 km (d) 5 km

(e) 3 km (f) 1 km

Figure 5.9: Horizontal cross sections of divergence in 10^{-5} s^{-1} *(shaded) and horizontal wind vectors at 11 km (a), 9 km (b), 7 km (c), 5 km (d), 3 km (e) and 1 km (f) with a horizontal resolution of 1 km. For further information, see Fig. 5.1.*

with height and at 7 and 9 km (Fig. 5.9(c), Fig. 5.9(b)) the northwestern quadrant exhibits predominantly divergence. Cross sections suggest that enhanced outflow is the reason for this divergence pattern at these levels. Thus, the divergence in the region of broad ascent to the northwest of the center exhibits the typical in-up-and-out flow pattern of a tropical cyclone.

In the area to the northwest of the center, the vertical velocity showed a band structure with a region of ascent flanked by two regions of descent at both smaller and larger radii. In this area, the divergence pattern at lower levels (1 and 3 km) is closely linked to the vertical velocity. The areas of descent exhibit divergence and the areas of ascent exhibit convergence. At midlevels (5 and 7 km), a region of divergence at the inner edge of the eyewall is flanked by a region of convergence to larger radii. Recall that in the cross section through this region (lefthand side of Fig. 5.8(a)), strong ascent in the region of high reflectivity and descent toward the center could be seen at mid- to upper levels. The location of strongest divergence coincides with the location of the inner edge of the eyewall at midlevels and thus, with a region located in between ascent and descent. This creates strong divergence. This band of divergence shifts outward with height, following the slope of the ascent. At 11 km (Fig. 5.9(a)), the divergence pattern can be link again to vertical velocity. This time, the areas of ascent exhibit divergence and the areas of descent exhibit convergence, since this level is near the upper boundary.

In the southwestern quadrant, there is a pronounced band of convergence at 7 km. It elongates from the outer edge of the eyewall to the west to the inner edge of the eyewall to the southwest. The horizontal winds show a directional convergence and the vertical velocity shows, that this region of convergence coincides with a region of descent. Thus, it suggests descending inward flow of environmental air.

These are the main features that can be seen in the divergence. The other regions around the eyewall are highly structural.

5.2 Influence of shear

The overview in the last section showed a very diverse structure of the eyewall. This structure and the intensity of Sinlaku are influenced by many factors such as the energy supply from the ocean, possible orographic effects caused by the nearby location of Japan and the influence of the environmental flow. In general, if the tropical cyclone is still located over the ocean, vertical wind shear of the environmental flow is supposed to be one of the most dominant factors affecting the structure of a tropical cyclone. Although the possibility that other effects significantly contribute to the structure of the eyewall can not be eliminated and their impact can not be quantified, the following investigation assumes that the main factor influencing Sinlaku's structure is the vertical shear of the environmental flow. Hence, the correlation of the structural characteristics of the core region of Sinlaku with the vertical shear will be examined.
At the time of interest, 19 September at 00 UTC, the shear amounts to 7.50 m s^{-1} and is west-southwesterly, more precisely the shear angle is 76.35°, where 0° is north and the angle in measured clockwise (see section 3.4).

5.2.1 Vertical tilt

The influence of shear on the vertical structure of a tropical cyclone has been studied intensively both in dry (Jones (1995, 2000)) and moist (e.g. Frank and Ritchie (1999, 2001)) model studies. In the dry case and if the shear is not too strong, the shear will induce an initial tilt roughly in the direction of the shear that will precess with time (Jones, 1995). In case that moist processes are included in the simulations, the tilt develops to be at near-equilibrium to the downshear-left side and no precession is found to occur (Chan and Kepert, 2010). Since this study consists of a "snapshot" of Sinlaku, no conclusions can be drawn about the temporal evolution of the tilt and thus a possible precession.
In order to determine the tilt of Sinlaku, the center of Sinlaku has to be identified at all heights. A variety of ways exists to define the center of a tropical cyclone. One way is to assign the center to the location where the wind goes to zero. The disadvantage of this "wind center" definition is, that the center depends on the assumed translation speed of the vortex. Another way of defining the center was proposed by Marks et al. (1992). To determine the "circulation center", they maximize the vorticity within the radius of maximum winds (RMW). This method is not sensitive to

the storm motion, but poses the difficulty of first computing the radius of maximum winds for each height. In this section, both the wind and the circulation center are calculated to obtain the best estimate of center of Sinlaku. The SAMURAI analysis with a resolution of 4 km is used for the calculations.

The wind center for each level is computed by first identifying all grid points with wind speeds $\leq 3m\ s^{-1}$. Then, from subset of grid points fulfilling this criterion, the grid point located furthest to the north is identified and its latitude is defined as the maximum latitude. In an analogous manner, the minimum latitude is determined by the grid point located furthest to the south, the maximum longitude is determined by the grid point furthest to the east and the minimum longitude is determined by the grid point furthest to the west. Thus, a rectangle containing all grid points with

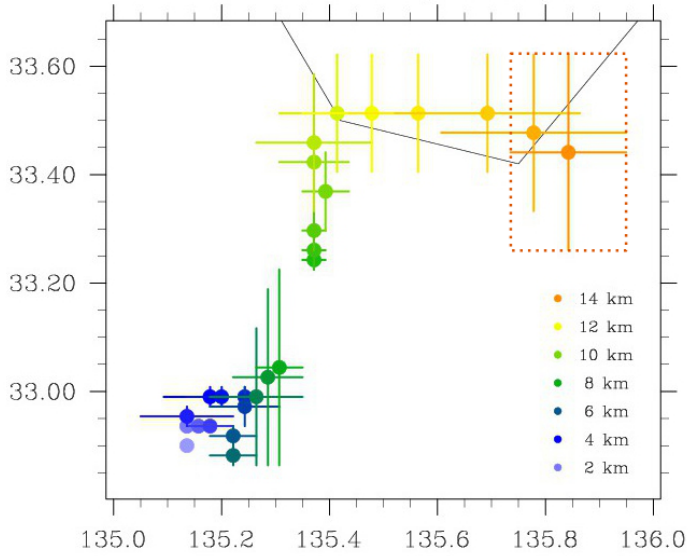

Figure 5.10: Location of the wind center for all heights. For the uppermost level a rectangle containing all grid points with wind speeds $\leq 3m\ s^{-1}$ is shown. For all other heights only the center of the rectangle and its perpendicular bisectors are shown. Colors indicate the height.

wind speeds $\leq 3m\ s^{-1}$ can be constructed based on these four values. An example for such a rectangle is plotted for the highest level marked in orange in Fig. 5.10. For clarity, at all other heights the respective area containing all grid point with wind speeds $\leq 3m\ s^{-1}$ is indicated by marking the center of the rectangle by a circle and the perpendicular bisectors by lines.

At lower levels (blue shades), the center is well defined, the lines representing the perpendicular bisectors are relatively short. At midlevels (dark green), the region of

wind speeds $\leq 3m\ s^{-1}$ gets larger and its meridional extent outweighs its zonal extent. Between 8 and 8.5 km the center jumps from a latitude of 33.04°N to 33.24°N, which is a distance of about 22 km. Above, the center first moves northward and starting at 11 km, it moves eastward with the rectangle getting larger.
The overview of the wind speed plots in the last section (Fig. 5.3) indicated, that the cyclonic circulation around a center can be seen clearly up to 7 km. Above, it was not that evident anymore. Looking at the wind speed plots also indicates, that at levels above 8.5 km the algorithm tracks the feature to the northeast of the eye, which most likely does not represent the tilted vortex but is a separate feature, because at 9 km there is still a local minimum of wind speed apparent south of this feature. Thus, it is assumed that the centers defined at levels above 8 km are not directly related to the tilt of the vortex and thus the tilt is determined between 0.5 and 8 km (see Tab. 5.1). This results in a tilt angle of 53.0° (with 0° being north, and the angle measured clockwise). With the shear angle being 76.35°, the tilt of the wind center is to the downshear-left side, as was suggested by idealized "full physics" simulations (Chan and Kepert (2010)). Another implication is, that Sinlaku cyclonic circulation extends up to about 8 or 9 km and above westerlies are dominating the flow pattern.

The second approach to finding the center of Sinlaku follows Marks et al. (1992). They define the center as the location that maximizes the vorticity inside the RMW, which is identical to maximizing the tangential wind at the RMW. A slightly dislocated center would result in lower values of tangential winds. E.g. if the center is dislocated slightly to the east but the value of the RMW is kept constant, the resulting average tangential wind will be smaller than in case of the actual center. To the east for the calculation of the tangential wind a location outside the actual RMW would be picked and to the west a location inside the RMW. Since at these locations the tangential winds are weaker than at the location of the RMW, the average tangential wind would be weaker also. Thus, inversely, the location of the center of a tropical cyclone can be determined by identifying the location that maximizes the tangential wind at the RMW. Since the RMW is not known either, the calculation of the tangential wind at RMW is conducted for various radii and center positions. More precisely, the tangential wind is calculated in a 4-km annulus around a given RMW, starting at an initial guess for the center position. Then, a two-dimensional "simplex" search (Nelder and Mead, 1965) is performed, which changes the initial guess center position according to a special algorithm and stops when a location is found, that exhibits higher tangential winds than its surroundings. The algorithm

works as follows. A triangle is constructed around the initial guess of the center. At all three vertices of the triangle the average tangential velocity is computed for the given RMW and compared to the result of the other two vertices. By reflection, contraction and expansion of the triangle the maximum tangential velocity is found (for more details see Lee and Marks (2000)). Since this could also be a local and not a global maximum, the "simplex" search is performed for 49 initial guesses and 20 radii (the assumed RMW) stretching from 8 to 88 km. If the maximum is global, for a given radius all 49 simplex searches should find the same center with the same tangential winds. In Sinlaku case, mostly 30 to 45 of the 49 searches found the same center. With these results, for every height level the radius of the 20 computed radii

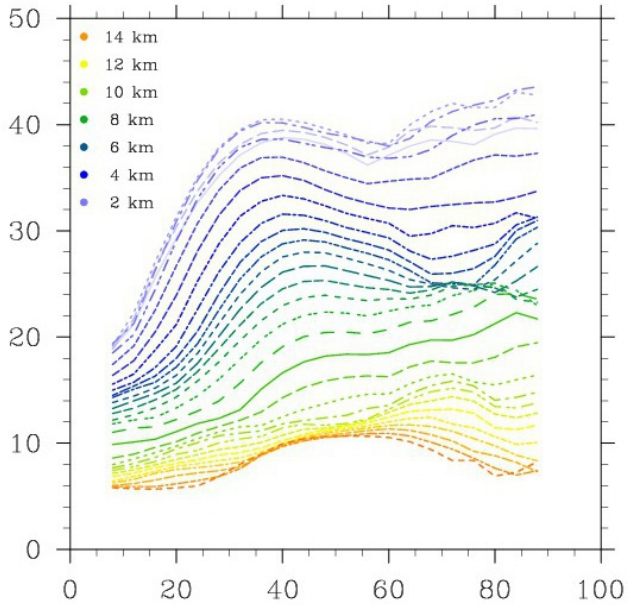

Figure 5.11: Tangential winds in m s^{-1} in dependency of the assumed RMW in km for all height levels. Colors denote the height.

can be identified, that really exhibits the highest tangential wind speeds and thus is the RMW. The center corresponding to this radius is then assumed to be the center of the vortex at the respective height level.

The relation between the tangential winds and the assumed RMWs is shown in Fig. 5.11. Over all, it can be seen that the maximum tangential wind speeds are highest at lower levels, as would be expected, and then decrease monotonically with height. At lower levels (blue shades) one local maximum appears at a radius of around 30 to 40 km, but the global maximum is located at the largest radii. This is

a computational artifact. Since our domain is only 140 x 140 km^2 large and Sinlaku is not axisymmetric anymore, calculating the tangential winds over a large radius with the annulus only being partly located in the analysis domain can result in a spuriously large tangential wind speed. Concentrating on the local maximum at smaller radii, it can be seen that the radius of maximum winds becomes larger with increasing height. At 2 km the radius is 30 km, increasing to 40 km at 6 km. At 8.5 km, marked by the solid green line, the local maximum starts to get weaker and becomes dominated another local maximum located at around 70 km. Above this, there again is only one maximum apparent, located at around 50 km.
Over all, the plots shows that at levels up to 8.5 km there is only one maximum in tangential winds for a RMW of around 40 km. This RMW constantly increases with height. At levels higher than 8.5 km it is not possible to objectively define one single maximum. Looking at the horizontal vorticity cross sections (Fig. 5.4) this is

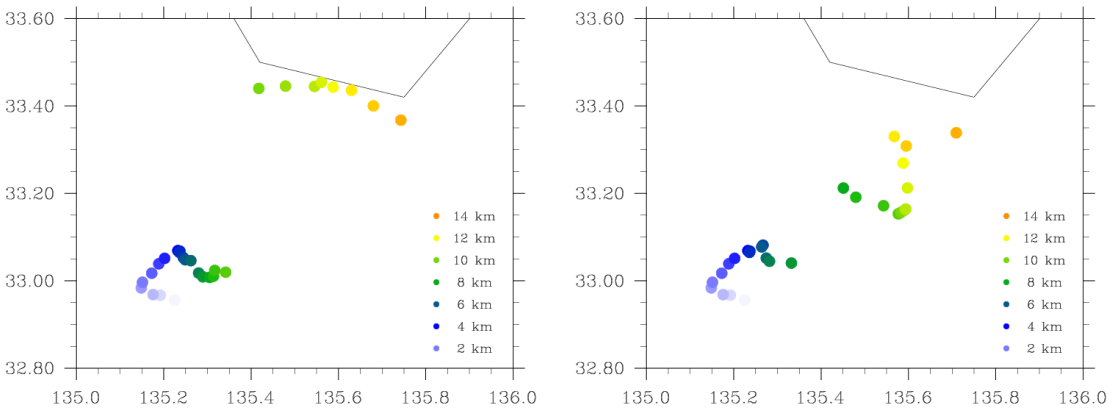

Figure 5.12: Circulation center locations for different RMWs. Colors indicate the height. (a) RMW increasing from 40 to 48 km with height. (b) RMW of 40 km at lower levels, at mid- to upper levels up to 70 km. For a detailed discussion see text.

probably due to the fact, that either the vorticity ring that breaks at higher levels is tracked or the maximum vorticity embedded in the vorticity ring in the north-east is tracked. To confirm this assumption the center positions that correspond to these maximum tangential winds are plotted. In Fig 5.12(a) the center position was chosen to linearly connect the maximum tangential winds at lower levels with the maximum tangential winds at upper levels. So at lower levels a RMW of 40 km was assumed, widening to 44 km at midlevels and to 48 km at the uppermost

levels. The change of the position of the circulation center with height resembles the distribution that was found for the wind center as well. At lower levels the center is located around 33°N/135.2°E and exhibits northeastward tilt. At midlevels the center jumps to a position much further north and then shifts to the east. This supports the assumption that the smaller scale feature to the northeast was tracked. For Fig. 5.12(b) the center up to a height of 6.5 km is the same as in Fig. 5.12(a), but after that shifts slowly to the local maximum of tangential wind at a RMW of 70 km. This results in positions of the center at midlevels, that are much further to the south compared to 5.12(a). This points to now tracking the vorticity ring instead of the smaller scale feature to the northeast.

Because of the large difference between the locations of the center depending on the estimated size of the radius of maximum winds, it is not possible to objectively determine a circulation center at levels above 8.5 km. This matches with the findings of the other center finding approach. Above 8.5 km no distinct center can be defined, which implies that the cyclonic circulation of Sinlaku might only extend to about 9 km.

As for the wind center, the tilt angle of the circulation center is calculated between 0.5 and 8 km (see Tab. 5.1). This results in a tilt angle of 27.3° for the circulation center. As for the wind center, the tilt angle is on the downshear left side, but the

Table 5.1: Tilt angle calculation

	wind center	circulation center
center at 0.5 km	32.94°N/135.14°E	32.95°N/135.23°E
center at 8 km	33.04°N/135.31°E	33.04°N/135.28°E
tilt angle	53.0°	27.3°

angle is larger. This deviation is mostly due to the difference in the longitude values for the different centers at 0.5 km. Given the uncertainties in the center finding methods, a definite tilt angle can not be specified, but it could be established that the tilt is to the northeast, which is the downshear-left side. This is in agreement with results of model studies including moist processes. Moreover, the difficulties in defining a center at upper levels led to the conclusion that a closed primary circulation exists up to about 8.5 km.

5.2.2 Asymmetries in the convection pattern

As was shown in the last section, the shear tilts the vortex to the downshear left side. This results in an altered horizontal flow pattern, which in order to be balanced forces an altered vertical flow. Model studies with dry dynamics showed that the isentropes have to be perturbed upwards on the down-tilt side. In a dry vortex this is can be achieved through maximum ascent to the right of the tilt vector. In "full physics" simulations the maximum updrafts were located in the downshear-left quadrant and the rainfall maxima slightly downstream because of the horizontal cyclonic advection that is imposed on the falling precipitation (Wang and Holland (1996), Frank and Ritchie (1999, 2001)). Observational studies also indicate that precipitation tends to be downshear left (e.g. Reasor et al. (2000)). E.g., the recent observational study by Hence and Houze (2011) investigated a composite of the core region of intense tropical cyclones using TRMM Precipitation Radar data. Their results suggest that the maximum rainfall region is located in the downshear-left quadrant and the convective generation of precipitation occurs in the downshear-right quadrant.
Hence, despite the fact, that there is no consensus about the exact location of the maximum updrafts, the shear is supposed to introduce asymmetries to both vertical motion and rainfall pattern around the eyewall.
To analyze the asymmetric structure of convection in more detail, the SAMURAI analysis domain is split up into quadrants according to the shear direction (Fig. 5.13). In section 5.1 the structural characteristics of Sinlaku were examined in detail, but e.g. choosing the location of a cross section is rather subjective and can only display a subset of the data. To gain insight into the overall structure, a statistical approach is taken in this section using contoured frequency by altitude diagrams (CFADs) following Yuter and Houze (1995). The ordinate of the CFAD is height and the parameter of interest is plotted on the abscissa. To get a frequency distribution of the parameter, the data is first binned on every level. For reflectivity the bin width is 5 dBz and for vertical velocity 1 m s^{-1}. These counts are normalized by the total number of points on the respective level to get a frequency distribution, and, finally, the frequency distributions of all height levels are combined and frequency isolines are contoured. To visualize this procedure, an example of Yuter and Houze (1995) is shown in Fig. 5.14. In their Fig. (a) the first step in creating a CFAD is illustrated. For each height such a histogram of e.g. radar reflectivity has to be calculated. In Fig. (b) all histograms are merged, which results in a three-dimensional

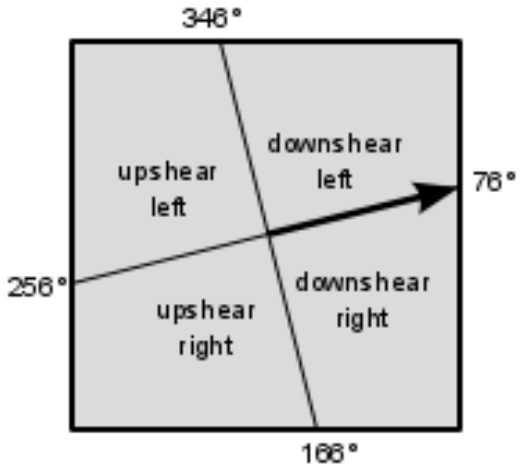

Figure 5.13: Schematics of splitting the SAMURAI analysis domain into quadrants according to the west-southwesterly shear vector.

frequency distribution. To simplify presentation, the perspective view is replaced with a contoured topographic map similar to that produced from elevation data for a mountain, which is the so called CFAD. The CFAD corresponding to Fig. (b) is shown in Fig. (c).

For all four quadrants defined in Fig. 5.13, CFADs of radar reflectivity are created (Fig. 5.15). In general, different types of precipitation result in different structures in the CFADs. Since stratiform precipitation is usually widespread and horizontally uniform, the frequency distribution concentrates on a few bins, and thus the frequency values are relatively high and the distribution is narrow. In contrast, convective precipitation consists of small updraft cores surrounded by weaker up- and downdrafts. Hence, the frequency distribution is broader and also contains higher values than in the stratiform case. As the precipitation particles fall, they undergo interaction with other precipitation particles and their environment. Above the melting layer effects such as deposition, aggregation and riming contribute to the growth of the particles, and below predominantly coagulation is supposed to contribute (K. D. Beheng, personal communication). Thus, the frequency distribution of reflectivity in general shifts to larger values with decreasing height. If the particles fall into a region of upward air motion, their fall speed is decreased and thus the time in which they can interact and grow is prolonged, which most likely results in larger particles. Hence, the slope of the distribution of reflectivity with height contains information about the magnitude of the particle growth and subsequently

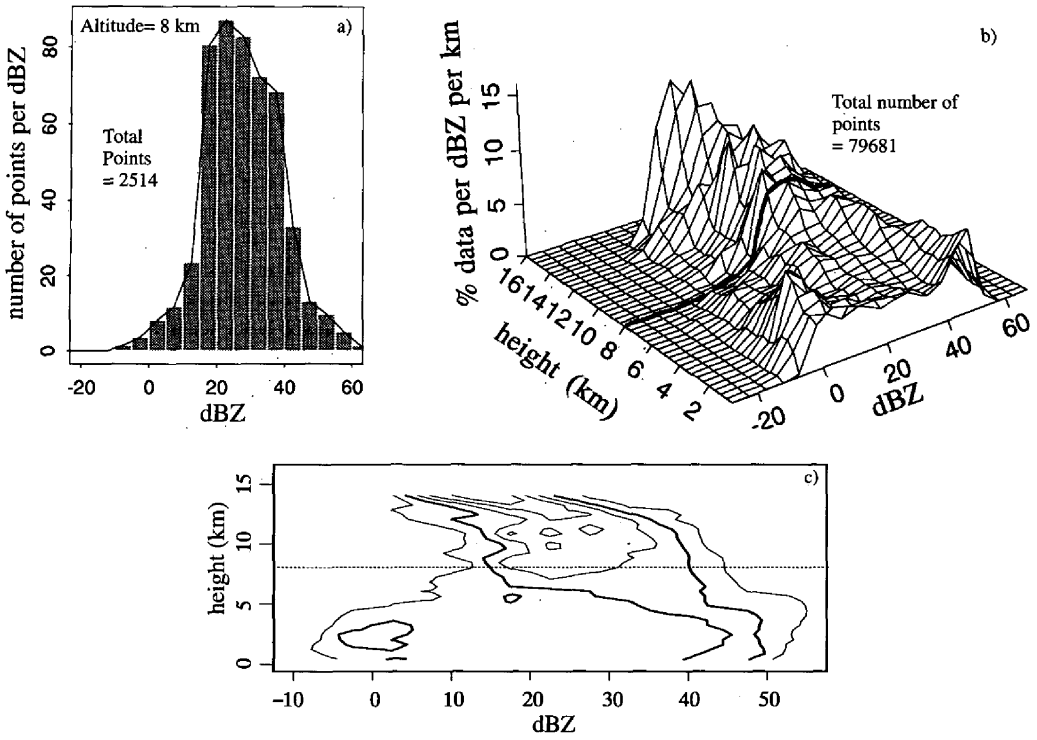

Figure 5.14: (a) Single-level histogram of radar reflectivity at 8 km. Histogram bin width is 5 dBz. (b) Perspective view of frequency by altitude diagram of radar reflectivity. Heavy line corresponds to single-level histogram at 8 km shown in (a). (c) Reflectivity CFAD. The bin size is 5 dBz, and the plot is contoured at intervals of 2.5% of data per dBz per kilometer with the 5% dBz^{-1} km^{-1} contour highlighted. Horizontal dashed line at 8 km corresponds to data contained in the single-level histogram in (a). From Yuter and Houze (1995).

about the environmental conditions in which they fell.

Recall that in the horizontal cross sections in section 5.1 the highest values of reflectivity were located in the northern part of the eyewall. Moreover, there was a gap in the reflectivity in the southwest at lower levels and in the southeast at higher levels. These features can also be seen in the CFADs. At lower levels up to 6 km, the frequency distribution is very broad in the downshear left and upshear left quadrants, which correspond to the northern half of the eyewall. Reflectivity values in a range from 10 to 35 dBz in the upshear left and from 10 to 30 dBz in the downshear left quadrants have the highest frequencies at lower levels. But there are also values exceeding 40 dBz in these two quadrants. In contrast, values in a range from 10 to 20 dBz are most common in the downshear right quadrant and the 0.05 isoline is as

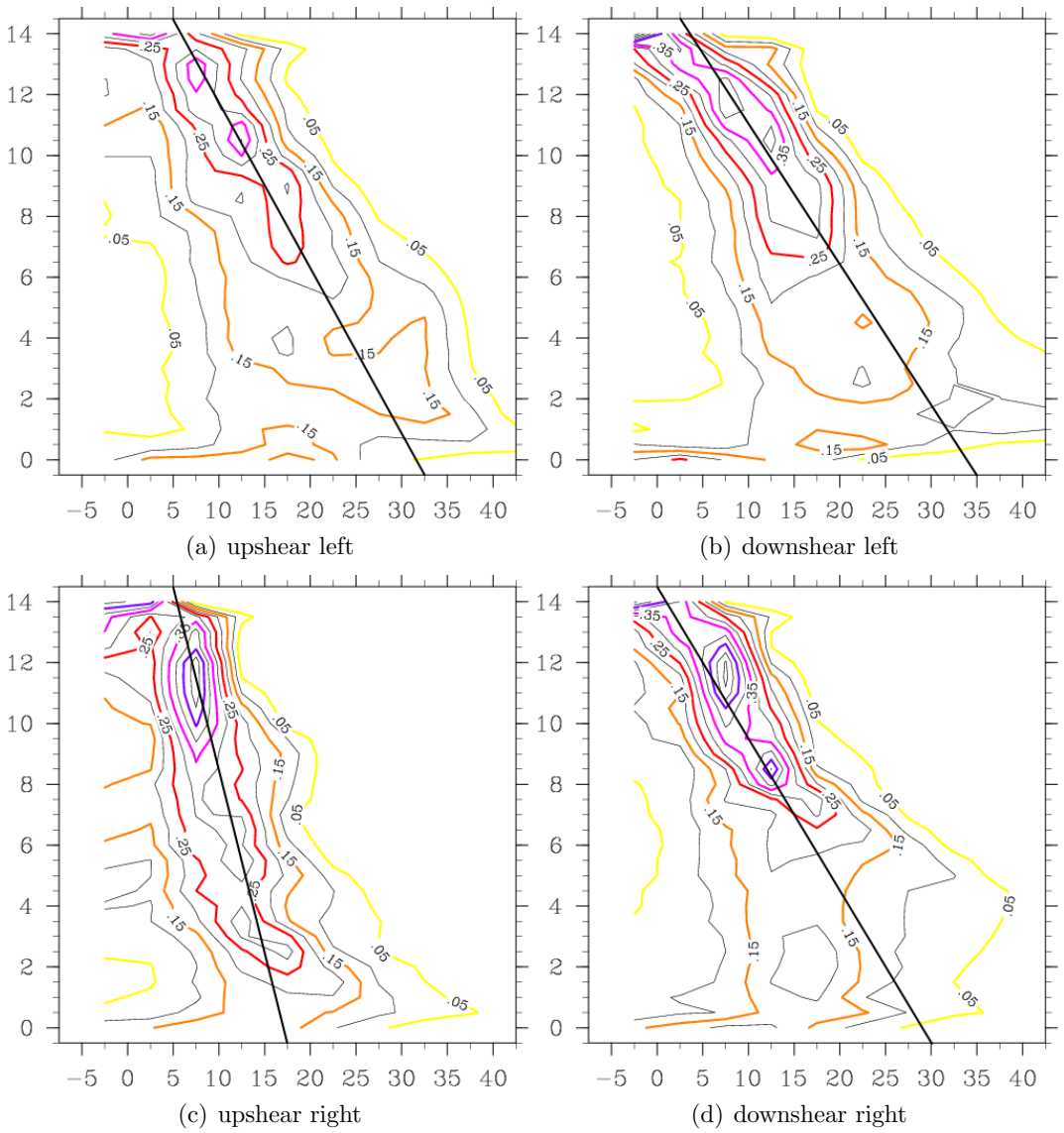

Figure 5.15: Contoured frequency by altitude diagrams for radar reflectivity for the four quadrants defined in Fig. 5.13. Bin width is 5 dBz. Contours are plotted every 5%, with colored contours marking 5% (yellow), 15% (orange), 25% (red), 35% (magenta) and 45% (purple). The black solid line indicates the subjectively estimated slope of the distribution.

low as 35 dBz. This appearance is more or less constant in the lowest 4 km in this quadrant. Thus, in this quadrant there is a lack of high reflectivities in the lowest 4 km, which is due to the gap in reflectivity to the southeast of the center in the horizontal cross sections. In the upshear right quadrant the most common values are

also between 10 and 20 dBz as in the downshear right quadrant, but even decrease with decreasing height. Furthermore, the distribution in this quadrant is the narrowest of all four quadrants at lower levels, even reaching frequencies of 0.3. Thus, at lower levels the quadrants to the left of the shear vector exhibit higher reflectivity values than the quadrants to the right of the shear vector. This is manifested in the 0.05 isoline as well as in the broadness of the distribution.

At upper levels the distributions in the quadrants to the right exhibit very narrow distributions with maximum frequencies of 0.5 in the range from 5 to 10 m s^{-1}. The 0.05 isoline at 11 km in the upshear right quadrant is located at 15 dBz, and in the downshear right quadrant at 17.5 dBz. In the quadrants to the left of the shear vector the maximum frequencies are 0.35 and 0.4 respectively, with the most likely reflectivity interval being 10 to 15 dBz at 11 km. The 0.05 isoline at 11 km is located at 20 dBz in both quadrants. Hence, both the maximum frequency and the 0.05 isoline at higher levels are shifted to higher values in the quadrants to the left of the shear vector in comparison to the quadrants to the right of it.

At midlevels the minimum reflectivities, represented by the location of the 0.05 isoline to the left of the maximum, is interesting. In the upshear left quadrant it is located between 0 and 5 dBz from 1 km altitude up to 7 km, in the downshear left quadrant even reaching up to 10 km. In the downshear right quadrant the 0.05 isoline is always below 0 dBz and in the upshear right quadrant it is only visible at 1 and 2 km height. Thus, the reflectivities at midlevels in the quadrants left of the shear vector exhibit a near absence of lower reflectivities, which points indicates active regions.

Another way to estimate the convective activity is to look at the slope of the distribution with height, because strong updrafts support the particle growth and thus the slope of both maximum frequency and general distribution is not that steep. The subjectively estimated slopes are represented by the solid black lines in Fig. 5.15. The downshear left quadrant exhibits the weakest slope with 2.2 dBz km^{-1} and thus the largest particle growth rate. The upshear right quadrant has a similar but slightly steeper slope with a value of 1.8 dBz km^{-1}, also indicating that it contains convectively active regions. In contrast, the upshear right quadrant's slope is very steep with 0.8 dBz km^{-1}, suggesting that in this quadrant there is no strong convection present. The downshear right quadrant is hard to describe with only one slope value, because of the lack of high reflectivity values at the bottom. For level from 1 to 5 km height the distribution is nearly constant with height and above the distribution is sloping with a value of 2.0 dBz km^{-1}. Thus, at lower levels particles

don't grow significantly while falling, but at higher levels the distribution's slope has a value that has the same magnitude as the quadrants left of the shear vector. Thus, the slopes of the reflectivity CFADs indicate that active convection is located at upper levels in the downshear right quadrant and in the quadrants to the left of the shear vector.
Noteworthy is also that in all quadrants the 0.1 isoline to the right of the maximum shows a peak between 4 and 6 km height. This is the range of height, where the temperature measurements of the dropsondes released by the C-130 showed the zero degree level. Thus, these peaks in the 0.1 isoline could indicate the location of the melting layer.

After examining the structure of the core region of Sinlaku with regard to the reflectivity distribution in the four quadrants, now the corresponding vertical velocity distributions are investigated. The maximum updraft regions are examined by looking at the structure of the 0.05 isoline. In the upshear right quadrant at lower levels up to 3 km there are only weak updrafts of 1.5 m s^{-1}, and above, they are slightly higher, reaching 2.5 m s^{-1}. Apart from this change between 3 and 4 km, the distribution is rather constant with height and there is no level, at which the isoline peaks and would indicate a level of enhanced convection. In the upshear left quadrant the 0.05 isoline is shifted to higher values up to 3 m s^{-1} and the distribution peaks at midlevels. Even higher values of vertical velocity are reached in the downshear left quadrant with the 0.05 isoline being located at 3.5 m s^{-1}, peaking between 5 and 6 km height. Hence, the strongest updrafts are located to the left of the shear vector at midlevels. The highest values of vertical velocity occur in the downshear right quadrant, peaking also at midlevels and exceeding values of 4 m s^{-1}. So the most vigorous convection takes place in the downshear right quadrant at midlevels. Thus, this is consistent with Hence and Houze (2011), who found that the triggering of convective updrafts occurs in the downshear-right quadrant.
The structure of the maximum downdrafts can analogously be investigated by the 0.05 isoline to the left of the maximum frequency. In the upshear right quadrant the maximum downdrafts occur at levels below 9 km, with the highest values of -2.5 m s^{-1} at 5 to 6 km. The upshear left quadrant exhibits similar magnitudes of downdrafts of about -2 m s^{-1}, but located at higher levels, namely from 5 to 11 km height. In the downshear left quadrant there is hardly any downward motion at all. Between 4 and 12 km height the maximum values are -1 m s^{-1}. The downshear right quadrant also consist mainly of updrafts, but has downdrafts throughout the

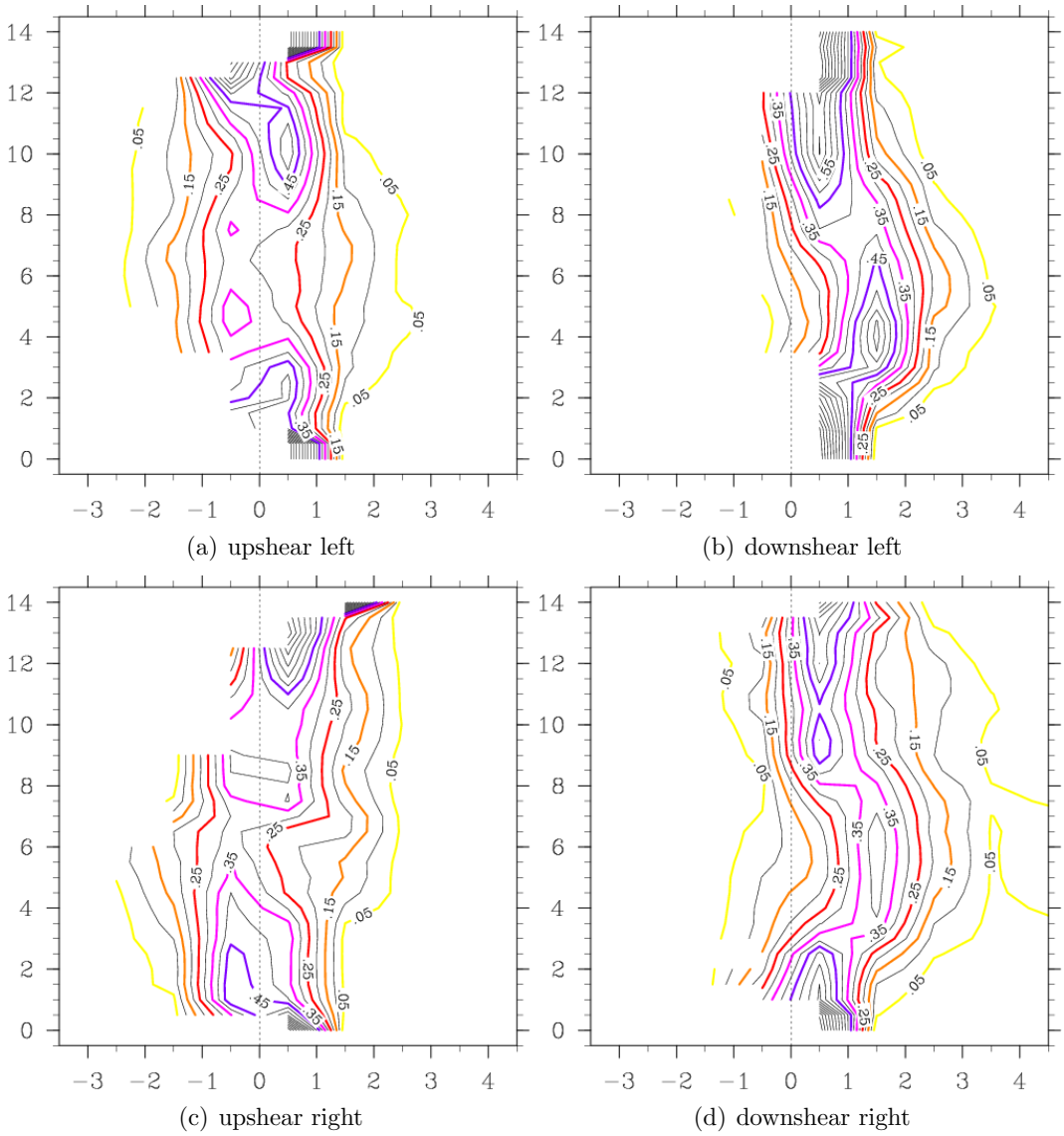

(a) upshear left (b) downshear left

(c) upshear right (d) downshear right

Figure 5.16: Contoured frequency by altitude diagrams for vertical velocity for the four quadrants defined in Fig. 5.13. Bin width is 1 m s^{-1}. Contours are plotted every 5%, with colored contours marking 5% (yellow), 15% (orange), 25% (red), 35% (magenta) and 45% (purple). The dashed black vertical line denotes the vertical velocity of 0 m s^{-1}.

whole vertical extent with the 0.05 isoline being located between -1.5 and 0.5 m s^{-1}. Hence, the upshear quadrants display downdrafts, the left one at upper levels and the right one at lower levels. The downshear quadrants have significantly less downdrafts and the ones that exist are less pronounced.

After investigating the variability of maximum ascent and descent between the different quadrants, the CFADs are examined in terms of the most frequent vertical motions. Therefore, the structure of the red 0.25 isolines is investigated. In the upshear right quadrant, the frequency distribution at levels up to 4 km is symmetric around zero vertical motion. Hence, there are approximately as many moderate updrafts as downdrafts. At 6 km height the distribution is shifted furthest towards negative vertical velocities. Above 6 km the distribution shifts back to more positive values. In the upshear left quadrant the frequency distribution in general is symmetric around zero vertical motion, with deviations to negative values at around 6 km and to positive values at 10 km. Thus, this quadrant exhibits both up- and downdrafts at all levels. In the downshear left quadrant the left of the two 0.25 isolines crosses zero at 7 km height. Beneath this level the maximum frequencies are all located in the ascent region. At levels above 7 km, also downdrafts occur more frequently, but updrafts still dominate. Between 3 and 6 km height the distribution is shifted furthest to positive values, with the vertical velocities between 1 and 2 m s^{-1} occurring most frequently. Hence, this quadrant is dominated by updrafts, the highest values being located at midlevels. The downshear right quadrant exhibits a structure similar to that in the downshear left quadrant. The 0.25 isolines are shifted furthest to positive values, with the left isoline crossing the zero at 3 and 8 km height. Below 3 km there are also moderate downdrafts present, but in general this quadrant is also dominated by upward motion.
In summary, the most vigorous updrafts occur in the downshear right quadrant at midlevels, the downshear quadrants are dominated by updrafts and downward motion takes predominantly place in the upshear quadrants.

To further elucidate the differences of the vertical motion in the four quadrants, the cumulative area coverage of vertical velocity as a function of height is plotted (Fig. 5.17), following Yuter and Houze (1995). The red line, labeled with value zero, for example separates the plot into the area percentage which has upward motion from the area percentage which has downward motion. So in the downshear right quadrant at 2 km height the red line has a value of 20%. This means that 20% of the area in the downshear right quadrant at 2 km exhibit downward motion, and 80% exhibit upward motion. Moving two contour lines up to higher values, the plot shows that about 80% of the area are covered with vertical velocities lower than 1.0 m s^{-1} and subsequently 20% greater than 1.0 m s^{-1}.
Distinct differences between the four quadrants can be seen in the area coverage

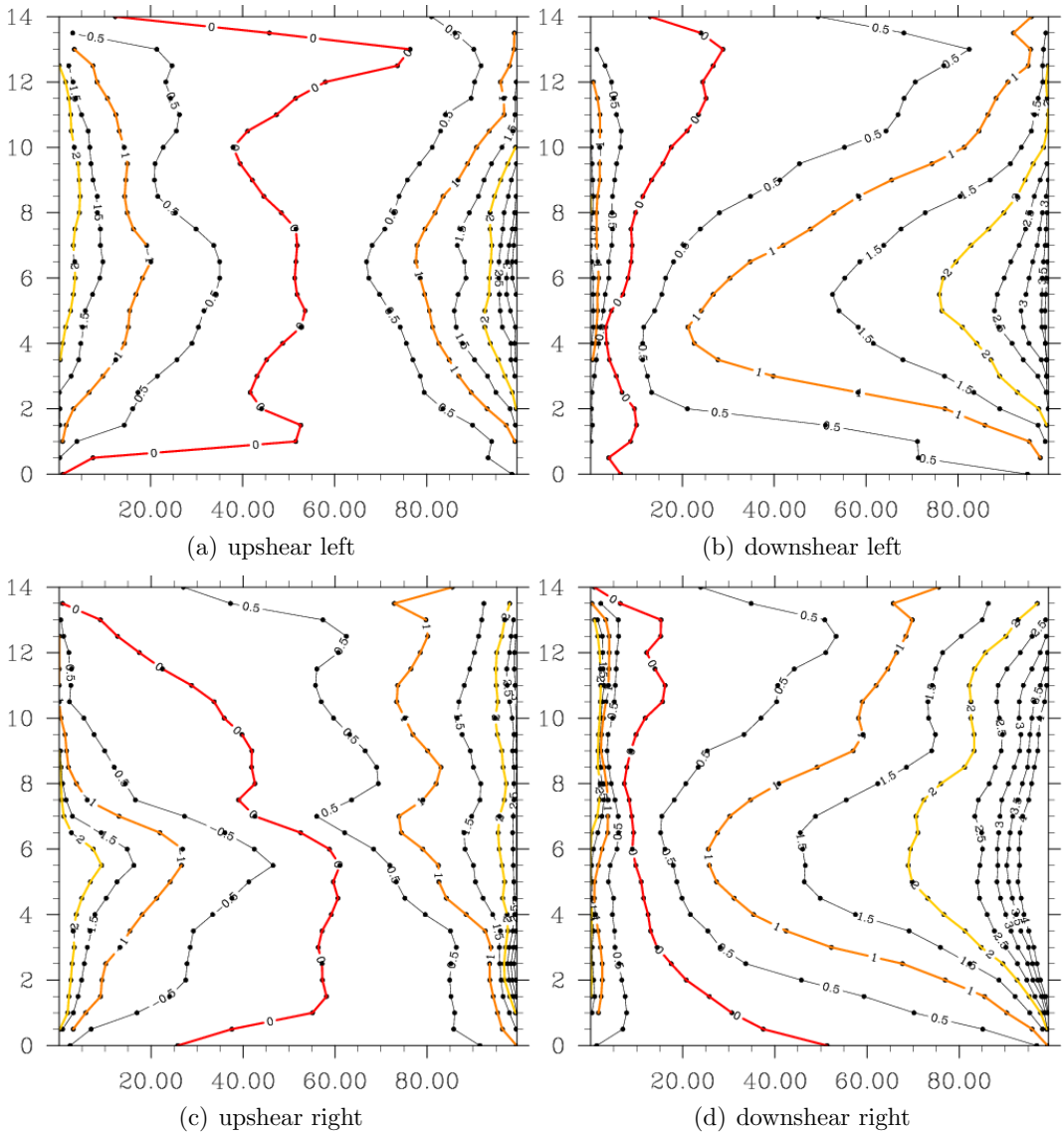

(a) upshear left (b) downshear left

(c) upshear right (d) downshear right

Figure 5.17: Cumulative area coverage of vertical velocity as a function of height. Each curve shows the percentage of area at a given height less than the indicated threshold value. The threshold values are spaced in intervals of 0.5 m s^{-1}, with the absolute values of 2 m s^{-1} (yellow), 1 m s^{-1} (orange) and 0 m s^{-1} (red) highlighted in colors.

of ascent and descent. In the downshear right quadrant the highest percentage of downward motion is located at the lowest levels, but decreases to 15% at a height of 3 km. At 10 to 13 km height the area covered by downward motion increases slightly, but this also only reaches about 15%. So above 3 km at least 85% of the

area is covered with ascent. In the downshear left quadrant the picture is similar. The increased percentage of downward motion at lower levels is missing, in contrast levels higher than 10 km exhibit a fraction of downward motion that is greater than 15 %. But otherwise the upward motion at all other levels amounts to at least 85%, which is the same as in the downshear right quadrant. The upshear left quadrant displays an almost equal area covered by ascent and descent. Except for the levels below 1 km and above 12 km, the red 0 m s^{-1} line is always located between 40 and 60%. In the upshear right quadrant the percentage of upward motion is higher than 60% at levels higher than 7 km, and increases with height. Between 1 and 6 km the vertical velocity is predominantly negative. The increased percentage of downward moving air at low levels in the downshear right quadrant is most likely a continuation of this downward motion.

The cumulative area coverage plots also shed light on the percentage of strong updrafts. In the downshear quadrants at levels around 6 km height, the vertical velocities reach high values, with over 60% of the area covered with updrafts stronger than 1 m s^{-1}. In the downshear right quadrant, there is even a significant fraction of updrafts exceeding 4 m s^{-1} up to heights of 10 km. The upshear left quadrant not only exhibits a balanced ratio regarding up- and downdrafts, but also looks symmetric in respect to the maximum values of vertical velocities. Maximum up- and downdrafts both occur at midlevels. For example at 7 km, 20% of the area is covered by downdrafts stronger than 1 m s^{-1} and 20% of the area is covered by updrafts stronger than 1 m s^{-1}. At higher and lower levels the fraction of high velocity values diminishes and values between -0.5 and 0.5 m s^{-1} are most common. In the upshear right quadrant the strongest updrafts are located just above the level of strongest downdrafts at around 6 km. At 5 to 6 km height the highest percentage of strong downdrafts occurs, exceeding 2 m s^{-1}.

These results support and extend the findings of the vertical velocity CFADs. The downshear side is dominated by upward motion, the upshear left quadrant has a well-balanced ratio of upward and downward motion and the mid- to low levels of the upshear right quadrant exhibit more descent than ascent.

5.2.3 Intrusion of environmental air

In section 5.1 the cross section to the west-southwest of the center suggested some kind of inflow in a layer around 7 km. Moreover, in the horizontal divergence plots a band of convergence coinciding with the location of a band of descent was found to the west-southwest. To further elucidate this region, thermodynamic properties both in and around it will be examined using dropsonde profiles. The C-130 flew at a height of around 9.3 km, which corresponds to a pressure level of approximately 350 hPa. and thus provides dropsonde data in a large vertical range. In Fig. 5.18 the flight tracks and the drop release positions are plotted. It shows that three C-130 dropsondes were released in the SAMURAI analysis domain and another three dropsondes in the near vicinity. The C-130 skew-T plots are compared with the ECMWF operational analysis data for 06 UTC on 19 September (Fig. 5.19).
Starting with the dropsonde furthest to the west (Fig. 5.19(a)), it can be seen that the course of the temperature curve, in general, is approximately neutral and there is no height level where the air is completely saturated, but at levels up to 500 hPa the dewpoint depression is very small and thus the air very moist. The most

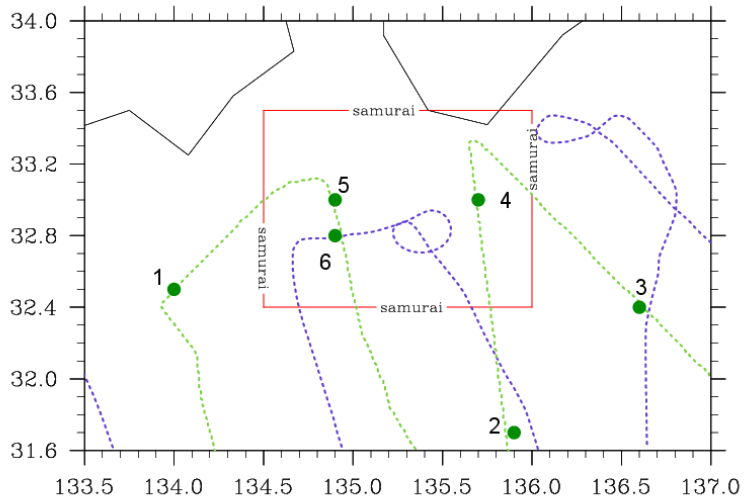

Figure 5.18: Location of the C-130 dropsondes marked with green circles. The numbers correspond to the skew-T plots in Fig. 5.19. The flight track of the C-130 is denoted by the dashed green line, the flight track of the P-3 by the blue line and the SAMURAI analysis domain by the red box.

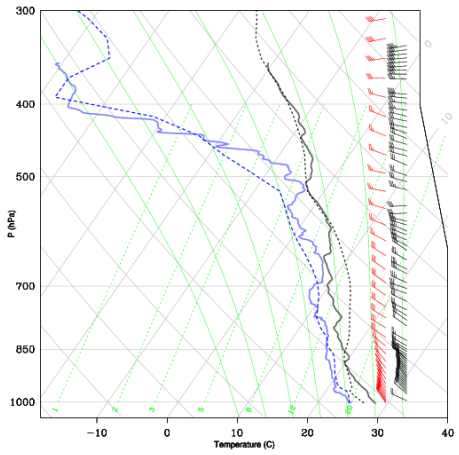

(a) C130 04.49 UTC, dropsonde 1

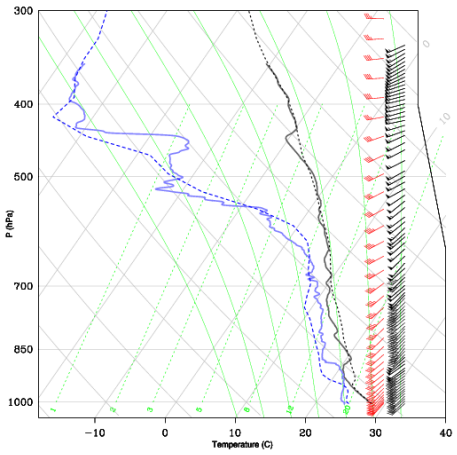

(b) C130 03.46 UTC, dropsonde 2

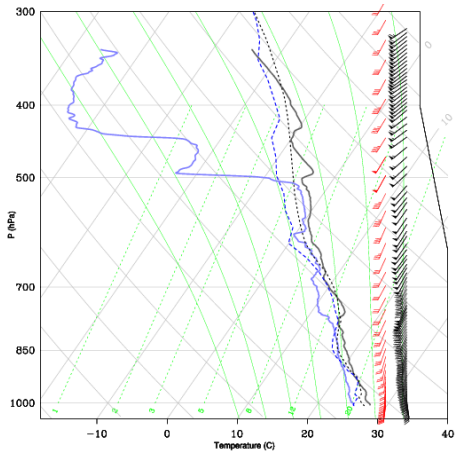

(c) C130 03.06 UTC, dropsonde 3

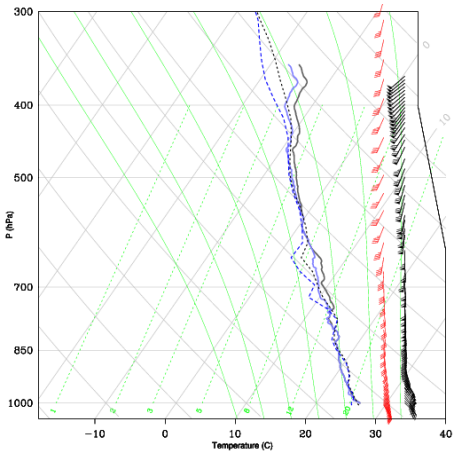

(d) C130 03.28 UTC, dropsonde 4

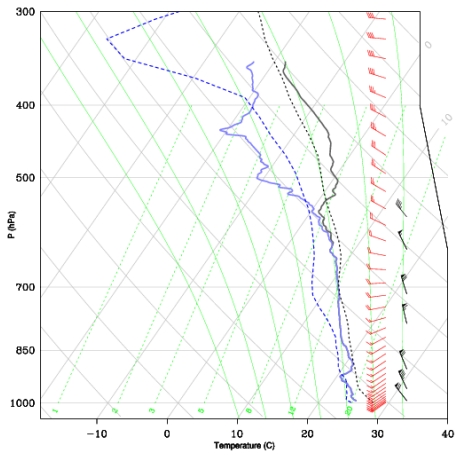

(e) C130 04.36 UTC, dropsonde 5

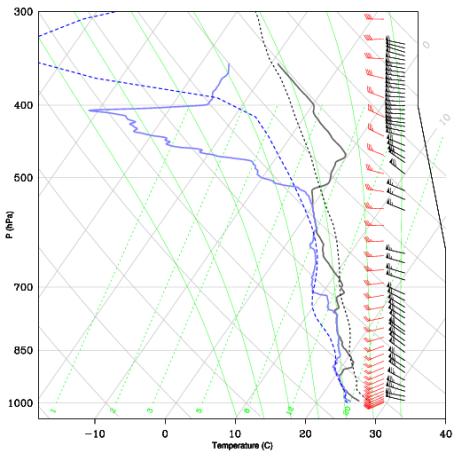

(f) C130 04.32 UTC, dropsonde 6

Figure 5.19: Skew-T plots for six C-130 dropsondes. The solid lines correspond to the dropsonde data, the dashed lines to the ECMWF operational analysis data for 06 UTC on 19 September, which were averaged in a square of 1˚x1˚, centered ground the grid point closest to the release position of the dropsonde. Blue lines indicate dewpoint temperature, black lines temperature. Red wind barbs denote the horizontal dropsonde winds, black wind barbs denote analysis winds. The location of the dropsondes is marked in Fig. 5.18.

significant feature in the diagram is the strong decrease in dewpoint temperature at levels above 500 hPa, with a minimum at around 400 hPa. Thus, this layer contains very dry air in contrast to the almost saturated levels below. The ECMWF analysis represents the temperature and dewpoint temperature distributions of the dropsonde quite well. The dropsonde winds are also captured well both in direction and magnitude by the operational analysis.
Dropsonde 2 is located to the south of the SAMURAI analysis domain. It also exhibits a minimum in dewpoint temperature at 400 hPa, but the dry layer stretches further down to about 600 hPa. The wind direction of analysis and dropsonde both show southwesterly to westerly flow, but the analysis underestimates the wind speeds significantly. At levels from 450 to 500 hPa the temperature curve runs parallel to the dry adiabats, which could be an indication of subsiding air.
The third dropsonde located outside the SAMURAI analysis domain is shown in Fig. 5.19(c). It exhibits approximately neutral stratification and a dry layer centered around 400 hPa also. At this location, however, the ECMWF analysis does not capture the dry layer, but instead has an almost saturated profile. Moreover, the analysis again underestimates the wind speeds and the analyzed wind direction at levels above 700 hPa is southwesterly, in contrast to the west-southwesterly flow in the dropsondes. This wind shift is most likely due to the representation of Sinlaku in the EC analysis being too weak and too broad. In summary, the eyewall of Sinlaku is surrounded to the south by a dry environmental layer centered around 400 hPa. At the location of the dropsondes 1 and 3, this layer of dry air stretches down to 500 hPa. At the location of dropsonde 2, which is located furthest to the south, it extends down to about 600 hPa. The vertical extent of the dry layer above 400 hPa can not be identified from dropsonde data, because it is only available for levels up to 350 hPa. In height coordinates, the dry layer is centered around a height of 7.6 km, extending downward to 5.9 to 4.4 km and upward to at least 8.6 km. This dry layer is well represented both in height and magnitude in the ECMWF at the locations of dropsonde 1 and 2, but not at the location of dropsonde 3. There, the analysis shows an almost saturated profile at all levels and the wind direction at upper levels does not match the sounding either.
Now the dropsondes inside the SAMURAI analysis domain, more precisely in the eyewall region of Sinlaku are examined. Dropsonde 4 (Fig. 5.19(d)) is located in the eastern part of the eyewall and shows a saturated profile and neutral stratification throughout the depth of the measurement with a slight increase in stability at levels above 450 hPa. This is what would be expected in the presence of eyewall

convection. Moreover, the low-level wind barbs display a southeasterly flow in the lowest 100 hPa, indicating the inflow layer. The winds then shift first to southerlies and then to southwesterlies with height, so that vertical shear is apparent. The ECMWF analysis shows a vertical wind shear as well, but misses out on the inflow layer, underestimates the wind speeds significantly and has more southerly than westerly flow at upper levels.

Dropsonde 5 is located in the western part of the eyewall. The lower levels up to 600 hPa are completely saturated and neutraly stratified. Between 550 and 350 hPa there is a dewpoint depression at the same height as the dry layer surrounding the eyewall, but not as pronounced. The temperature curve around 400 hPa is almost parallel to the dry adiabats indicating subsidence. The wind barbs show very high values, which is consistent with the eyewall location of the dropsonde, and exhibit a vertical wind shear, with inflow at lower levels and northerly to westerlies at higher levels. The ECMWF analysis does not match the dropsonde data very well. The winds are too weak and consist of westerlies at all levels and the saturation at lower to mid-levels is not represented. There is a layer of dry air in the analysis but at 350 hPa and not between 400 and 500 hPa as in the dropsondes.

Dropsonde 6 is also located in the western part of the eyewall, just to the south of dropsonde 5. It can be seen that in this case the wind direction of analysis and dropsonde data match quite well, both have westerlies at all levels. At lower levels the analysis winds have a small southerly component and the dropsonde winds have a small northerly component, but otherwise the direction is similar. The dropsonde has wind speed magnitudes that are approximately twice as high as the analysis values, but, as mentioned previously, the analysis is not expected to represent the intensity of a tropical cyclone correctly. The temperature and dewpoint profiles are similar to those of dropsonde 5. There is a dewpoint depression at levels between 400 and 500 hPa and the temperature curve runs parallel to the dry adiabats above 400 hPa, indicating downward motion. But the dewpoint depression is larger for this dropsonde than for dropsonde 5 and the levels below this dry layer are not all saturated. Around 700 and 850 hPa there are drier regions. The analysis again locates the dry layer at too high levels.

Thus, the dropsondes in the western part of the eyewall have significantly different characteristics to those on the eastern side. They do not show saturation at all heights, but have drier air at levels around 400 hPa, just as the dropsondes outside the SAMURAI analysis domain. This suggests that Sinlaku was not able to encapsulate its circulation from the environment and that dry air being advected from the

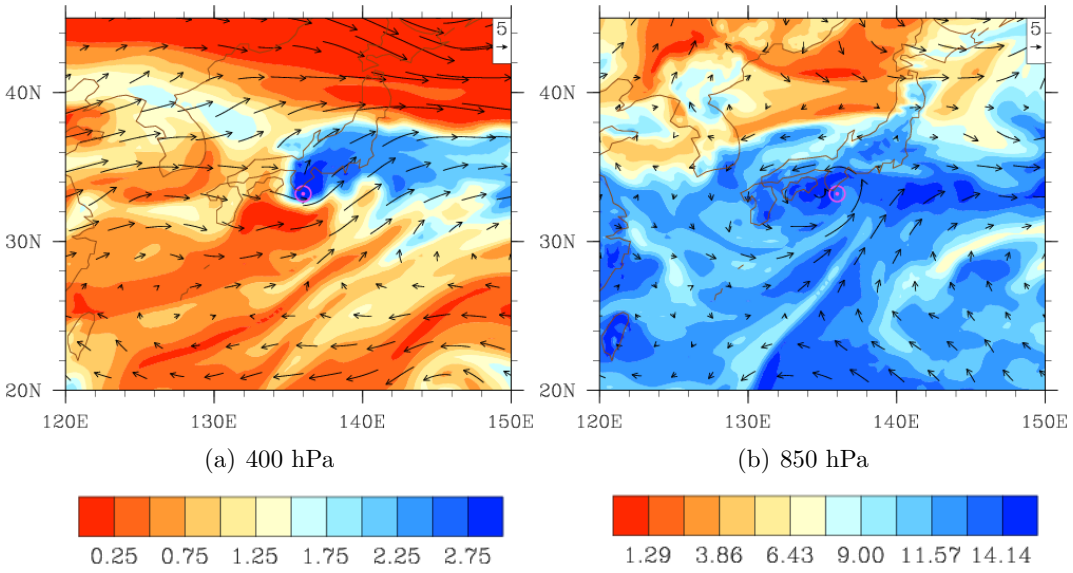

(a) 400 hPa (b) 850 hPa

Figure 5.20: Specific humidity in g km^{-1} (shaded) and horizontal wind vectors at 400 and 850 hPa from the ECMWF operational analysis data at 06 UTC, 19 September 2008. The reference vector is in m s^{-1}. The best track position of Sinlaku is denoted by the pink circle.

west was able to penetrate at the western to southwestern side of Sinlaku.

The consistency of the ECMWF operational analysis with the dropsonde data varies considerably for the different dropsondes. The temperature and dewpoint profiles of dropsonde 1,2 and 4 were captured well in the analysis, for dropsonde 5 and 6 the location of the dry layer was too high and for dropsonde 3 the dry layer was missing completely. Hence, the analysis represents the overall structure quite well but is not able to capture the interaction of the environmental air with the cyclone's circulation.

In horizontal cross sections of specific humidity of the ECMWF analysis (Fig. 5.20), it can be seen that at 850 hPa the air surrounding Sinlaku is relatively moist. This matches with the dropsonde data, in which the lower levels are always near saturation. It indicates that no weakening of Sinlaku is expected due to dry air at the inflow level. In the dropsonde data the largest dewpoint depression was located at 400 hPa. At this level, the analysis shows that Sinlaku is surrounded by dry air. Only the region northeast of Sinlaku has higher values of specific humidity with could be a result of the tropical cyclone's outflow itself. Since at the location of dropsonde 3 the dry layer was not depicted in the analysis, it is likely that the dry air at 400 hPa is located even more closely to Sinlaku's center or wraps around it in

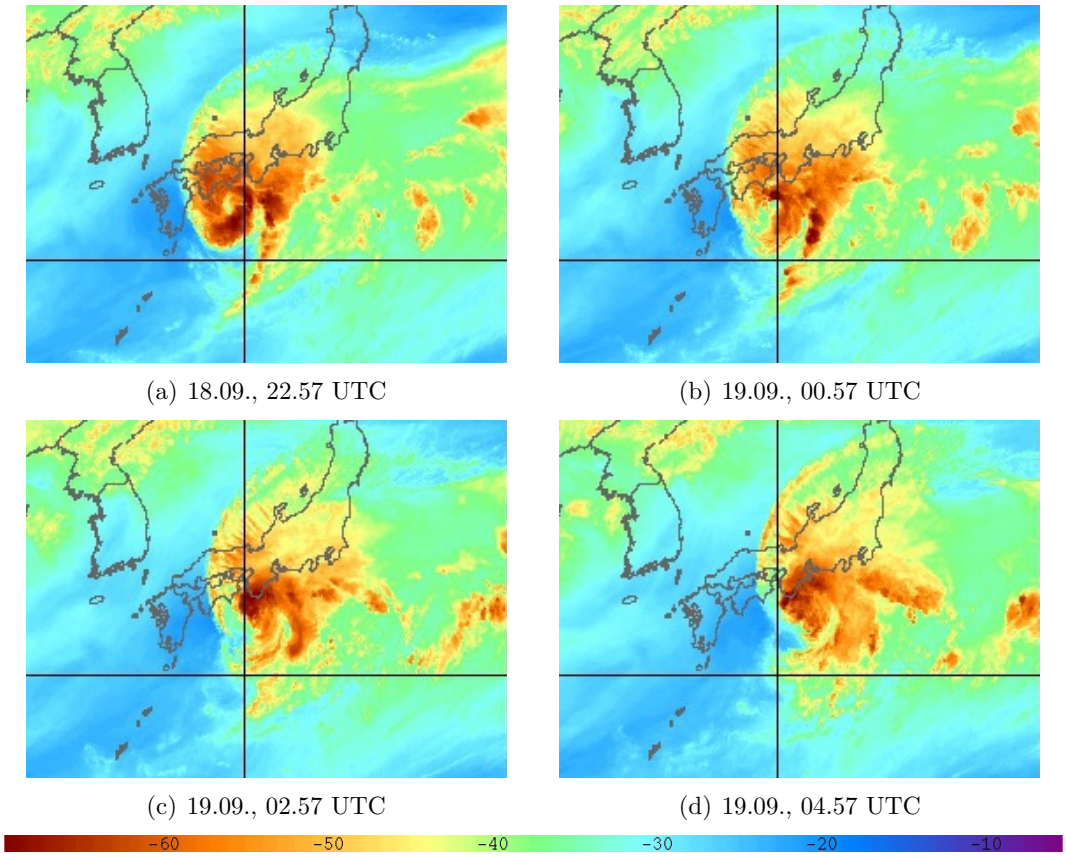

(a) 18.09., 22.57 UTC

(b) 19.09., 00.57 UTC

(c) 19.09., 02.57 UTC

(d) 19.09., 04.57 UTC

Figure 5.21: Water vapor imagery provided by the Naval Research Laboratory via the T-PARC field catalog. The plots cover an area of from 122°E to 145°E and from 25°N to 42°N.

the east as is shown in Fig. 5.20(a). In general the analysis data show that Sinlaku is embedded in a dry environment at upper levels and thus an intrusion of dry air from the west is possible. This finding is supported by the water vapor imagery (Fig. 5.21). To the west of Sinlaku the water vapor values are very low, resulting in a large gradient to the eyewall region with high water vapor values. At 22.57 UTC on 18 September the cyclonic structure of Sinlaku can be clearly seen. The eye with lower values is surrounded entirely by higher values due to the eyewall convection. At 00.57 UTC on 19 September, the ring of higher values breaks up in the southwest and the gradient in water vapor decreases over time, which could indicate mixing or subsidence. At 04.57 UTC, there is a region of drier air at the southwestern to southern edge of Sinlaku, which could indicate a dry intrusion of environmental air from the west into the circulation of Sinlaku.

The extent to which the dry environmental air could penetrate toward the center of Sinlaku could be dependent on the vertical wind shear, that had a strongly westerly component at upper levels. The dry air then subsides because of its higher density, suppresses the convection in the southwestern part of the eyewall and thus results in a weakening of the tropical cyclone. In the dropsondes 5 and 6, which are located

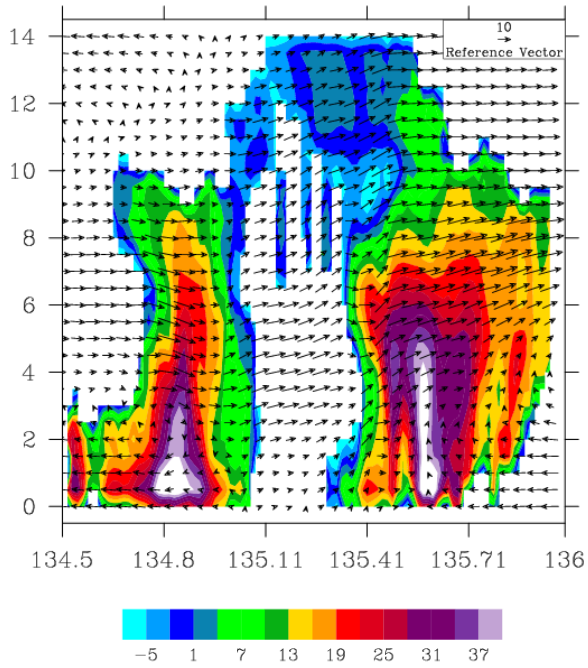

Figure 5.22: West-east cross sections of reflectivity in dBz (shaded) and wind vectors composed of vertical velocity and the in-plane component of horizontal velocity. The reference vector is in m s^{-1}. The horizontal resolution of the analysis is 1 km. The wind field is not masked.

in the western part of the eyewall, the dry air occurs at around 400 hPa, which corresponds to a height of 7.6 km. A cross section of reflectivity and velocity in this region (lefthand side of Fig. 5.22) shows descent at levels from 4 to 8 km height above a region of higher reflectivities. This fits in the picture of sinking dry air, that suppresses convection. Hence, there are several hints that dry air at midlevels was able to penetrate the western part of the eyewall.

6 Summary and Outlook

The structure and intensity of tropical cyclones is influenced by many factors, such as the ocean heat content, the environmental flow pattern and the interaction with other weather systems. The complexity of the environment increases as the tropical cyclone moves toward the midlatitudes and thus the prediction of the behavior of the tropical cyclone at this time of its life cycle is very challenging. One key component to a better forecast is to improve the understanding of the underlying physical processes that influence the structure of the tropical cyclone.

This improved understanding was one of the main goals of T-PARC. In the framework of this campaign, the evolution of Typhoon Sinlaku was investigated intensively. To be able to identify the physical mechanisms that determine the evolution of Sinlaku, first the structure of the typhoon has to examined in detail. Such a structural analysis is carried out in this thesis for a time late in Sinlaku's life cycle, more precisely, after an unexpected reintensification that interrupted its extratropical transition. The study presented here focuses on the core region of Sinlaku and is mostly based on data from an airborne Doppler radar, supplemented by dropsonde, flight level, satellite and ECMWF operational analysis data. This data set enables an unprecedented view of the inner core structure of the typhoon after the unexpected reintensification, but was very challenging to analyze also. In particular, the errors that were introduced in the vertical velocity because of the strong curvature of the flight track of the aircraft carrying the Doppler radar, had to be overcome. The data were assimilated on a regular grid by using a recently developed assimilation technique named SAMURAI (Bell et al., 2012). The resulting analysis showed marked asymmetries in the structure of the core region of Sinlaku. The radar reflectivity and the wind field exhibit very different characteristics depending on their location in the eyewall.

In the northeastern quadrant of the eyewall, the highest values of radar reflectivities were found and all heights were strongly dominated by ascent. A typical flow pattern with inflow at the lowest levels, ascent in the eyewall and strong outflow at higher levels was evident. To the northwest high radar reflectivities were found

also, but instead of strong outflow, there was a pronounced region of descent located at the inner edge of the eyewall. To the south and west of the center, there were pronounced gaps apparent in the eyewall. To explain these asymmetries, there are different mechanisms, that are likely to play a role. One possibility, that has been investigated in many studies is that the poleward moving tropical cyclone interacts with an existing midlatitude trough and, as a consequence of the interaction, intensifies rapidly. In the case of Sinlaku the main contribution of the midlatitude flow is considered to be restricted to the increasing shear during Sinlaku's life cycle. The midlatitude flow does not appear to interact directly with the cyclone's circulation. Thus, the shear is believed to be the main factor, determining the structure of Sinlaku, and the structure of Sinlaku is examined with respect to possible shear-induced characteristics.

The tilt of the tropical cyclone was established by identifying both wind and circulation center and it was found that the tilt is located to the left of the west-southwesterly shear, in agreement with previous studies. The investigation of radar reflectivity and vertical velocity with CFADs revealed that the main updraft regions were located in the downshear quadrants and downdrafts occurred mostly in the upshear regions. The regions with highest reflectivity values at low levels are located to the left of the shear vector, which is in accordance with the expectation that the regions of highest reflectivities are shifted slightly cyclonically relative to the regions of the strongest upward motion. These findings are again consistent with previous observations and model studies.

The dropsondes that investigated both the core region and the nearby environment of the eyewall suggest that Sinlaku interacted with dry environmental air at midlevels. This dry air intruded into the cyclone's circulation in the western part of the eyewall and could be responsible also for the relatively weak convection in the upshear right quadrant. It could have been made possible by the west-southwesterly shear. In conclusion, the structure of Sinlaku is supposed to be determined mainly by the vertical wind shear.

This study can identify the physical mechanisms that could account for the structure of Sinlaku. As the structure was examined for only one instant of time, it is difficult to determine the role of these mechanisms precisely. Further quantification of the mechanisms could be achieved by extending the work as part of a model study. Such an approach could shed light on the physical mechanisms and perhaps also elucidate the sensitivity of the cyclone's structure to individual features of its environment.

References

Anwender, D., P. A. Harr, and S. C. Jones, 2008: Pretictability associated with the downstream impacts of the extratropical transition of tropical cyclones: Case studies. *Mon. Wea. Rev.*, **136**, 3326–3247.

Atlas, D., R. C. Srivastava, and R. S. Sekhon, 1973: Doppler radar characteristics of precipitation at vertical incidence. *Rev. Geophys. Space Phys.*, **11**, 1–35.

Bell, M. M., 2010: Air-sea enthalpy and momentum exchange at major hurricane wind speeds. Ph.D. thesis, Naval Postgraduate School, Monterey, California.

Bell, M. M., M. T. Montgomery, and K. E. Emanuel, 2012: Air-sea enthalpy and momentum exchange at major hurricane wind speeds observed during CBLAST. *J. Atmos. Sci., submitted*.

Bosart, B. L., W.-C. Lee, and R. M. Wakimoto, 2002: Procedures to improve the accuracy of airborne Doppler radar data. *J. Atmos. Oceanic Technol.*, **19**, 322–339.

Bosart, L. F. and G. M. Lackmann, 1995: Post-landfall tropical cyclone reintensification in a weakly baroclinic environment: A case study of Hurricane David (September 1979). *Mon. Wea. Rev.*, **123**, 3268–3291.

Chan, J. C. L. and J. D. Kepert, 2010: *Global perspectives on tropical cyclones*. Vol. 4, World Scientific Publishing Co. Pte. Ltd.

Davis, C. A., S. C. Jones, and M. Riemer, 2008: Hurricane vortex dynamics during atlantic extratropical transition. *J. Atmos. Sci.*, **65**, 714–736.

Dunion, J. P., 2011: Rewriting the climatology of the tropical North Atlantic and Caribbean Sea atmosphere. *J. Climate*, **24**, 893–908.

Emanuel, K. A., C. DesAutels, C. Holloway, and R. Korty, 2004: Environmental control of tropical cyclone intensity. *J. Atmos. Sci.*, **61**, 843–858.

Frank, W. M. and E. A. Ritchie, 1999: Effects of environmental flow upon tropical cyclone structure. *Mon. Wea. Rev.*, **127**, 2044–2061.

Frank, W. M. and E. A. Ritchie, 2001: Effects of vertical wind shear on the intensity and structure of numerically simulated hurricanes. *Mon. Wea. Rev.*, **129**, 2249–2269.

Gallina, G. M. and C. S. Velden, 2002: Environmental vertical wind shear and tropical cyclone intensity change utilizing enhanced satellite derived wind information. *Extended abstracts, 25th Conference on Hurricanes and Tropical Meteorology*, 172–173.

Gao, J., M. Xue, K. Brewster, and K. K. Droegemeier, 2004: A three-dimensional variational data analysis method with recursive filter for doppler radars. *J. Atmos. Oceanic Technol.*, **21**, 457–469.

Gray, W. M., 1968: Global view of the origin of tropical disturbances and storms. *Mon. Wea. Rev.*, **96**, 669–700.

Handwerker, J. and K. D. Beheng, 2010: Vorlesung radarmeteorologie 2010/2011.

Harr, P. A., D. Anwender, and S. C. Jones, 2008: Predictability associated with the downstream impacts of the extratropical transition of tropical cyclones: methodology and a case study of Typhoon Nabi (2005). *Mon. Wea. Rev.*, **136**, 3205–3225.

Harr, P. A. and R. L. Elsberry, 2000: Extratropical transition of tropical cyclones over the western North Pacific. Part I: Evolution of structural characteristics during the transition process. *Mon. Wea. Rev.*, **128**, 2613–2633.

Hart, R. E. and J. L. Evans, 2001: A climatology of extratropical transition of Atlantic tropical cyclones. *J. Climate*, **14**, 546–564.

Hence, D. A. and R. A. Houze, 2011: Vertical structure of hurricane eyewalls as seen by TRMM precipitation radar. *J. Atmos. Sci.*, **68**, 1637–1652.

Hildebrand, P. H., et al., 1996: The ELDORA/ASTRAIA Airborne Doppler Weather Radar: High-Resolution Observations from TOGA COARE. *Bull. Amer. Meteor. Soc.*, **77**, 213–232.

Hoskins, B. J., M. E. McIntyre, and A. W. Robertson, 1985: On the use and significance of isentropic potential vorticity maps. *Q. J. R. Meteorol. Soc.*, **111**, 877–946.

Jones, S. C., 1995: The evolution of vortices in vertical shear. I: Initially barotropic vortices. *Q. J. R. Meteorol. Soc.*, **121**, 821–851.

Jones, S. C., 2000: The evolution of vortices in vertical shear. III: Baroclinic vortices. *Q. J. R. Meteorol. Soc.*, **126**, 3161–3186.

Jones, S. C., et al., 2003: The extratropical transition of tropical cyclones: forecast challenges, current understanding, and future directions. *Weather and Forecasting*, **18**, 1052–1092.

Joss, J. and A. Waldvogel, 1970: A method to improve the accuracy of radar measured amounts of precipitation. *Preprints*, 14th Conf. on Radar Meteorology, Tucson, AZ, Amer. Meteor. Soc., 237–238.

KITAMOTO Asanobu / National Institute of Informatics, 2011: Digital typhoon. http://agora.ex.nii.ac.jp/digital-typhoon/summary/wnp/s/200813.html.en.

Klein, P. M., P. A. Harr, and R. L. Elsberry, 2000: Extratropical transition of western north pacific tropical cyclones: an overview and conceptual model of the transformation stage. *Weather and Forecasting*, **15**, 373–395.

Klein, P. M., P. A. Harr, and R. L. Elsberry, 2002: Extratropical transition of western North Pacific tropical cyclones: Midlatitude and tropical cyclone contributions to reintensification. *Mon. Wea. Rev.*, **130**, 2240–2259.

Laing, A. and J.-L. Evans, 2010: *Introduction to tropical meteorology, a comprehensive online and print textbook*. Second Edition, Version 2.a, COMET Program, Unversity Corporation for Atmospheric Research.

Lee, W.-C. and F. D. Marks, 2000: Tropical cyclone kinematic structure retrieved from single-Doppler radar observations. Part II: The GBVTD-simplex center finding algorithm. *Mon. Wea. Rev.*, **128**, 1925–1936.

Marks, F. D., R. A. Houze, and J. F. Gamache, 1992: Dual-aircraft investigation of the inner core of Hurricane Norbert. Part I: Kinematic Structure. *J. Atmos. Sci.*, **49**, 919–942.

MetEd, operated by The COMET Program, 2011: Microwave remote sensing: Clouds, precipitation and water vapor. The University Corporation for Atmospheric Research,

http://www.meted.ucar.edu/npoess/microwave_topics/clouds_precip_water_vapor/navmenu.htm.

Mohr, C. G., 1988: Cedric - cartesian space data processor. Technical Report, National Center for Atmospheric Research, Boulder, CO, 78 pp.

Morgan, M. C. and J. W. Nielson-Gammon, 1998: Using tropopause maps to diagnose midlatitude weather systems. *Mon. Wea. Rev.*, **126**, 2555–2579.

NCAR Earth Observing Laboratory, 2010: Eldora user's guide. http://www.eol.ucar.edu/instrumentation/airborne-instruments/eldora/eldora-help-center/manual/users-guide.

Nelder, J. A. and R. Mead, 1965: A simplex method for function minimization. *Comput. J.*, **7**, 308–313.

NOAA Hurricane Research Division, 2009: Frequently asked questions. www.aoml.noaa.gov/hrd/tcfaq/E5.html.

Ooyama, K. V., 2002: The cubic-spline transform method: basic definitions and test in a 1D single domain. *Mon. Wea. Rev.*, **130**, 2392–2415.

Purser, R. J., D. P. W.-S. Wu, and N. M. Roberts, 2003: Numerical aspects of the application of recursive lters to variational statistical analysis. Part I: Spatially homogeneous and isotropic Gaussian covariances. *Mon. Wea. Rev.*, **131**, 1524 –1535.

Reasor, P. D., M. D. Eastin, and J. F. Gamache, 2009: Rapidly Intensifying Hurricane Guillermo (1997). Part I: Low-Wavenumber Structure and Evolution. *Mon. Wea. Rev.*, **137**, 603–631.

Reasor, P. D., M. T. Montgomery, F. D. Marks, and J. F. Gamache, 2000: Low-wavenumber structure and evolution of the hurricane inner core observed by airborne dual-Doppler radar. *Mon. Wea. Rev.*, **128**, 1653–1680.

Riemer, M. and M. T. Montgomery, 2011: Simple kinematic models for the environmental interaction of tropical cyclones in vertical wind shear. *Atmos. Chem. Phys.*, **11**, 9395–9414.

Ritchie, E. A. and R. L. Elsberry, 2007: Simulations of the extratropical transition of tropical cyclones: Phasing between the upper-level trough and tropical cyclone. *Mon. Wea. Rev.*, **135**, 862–876.

Sanabia, E. R., 2010: The re-intensification of Typhoon Sinlaku (2008). Ph.D. thesis, Naval Postgraduate School, Monterey, California.

Sauvageot, H., 1992: *Radar Meteorology.* Artech House, Inc., Boston.

Testud, J., P. H. Hildebrand, and W.-C. Lee, 1995: A procedure to correct airborne doppler radar data for navigation errors using the echo returned from the earth's surface. *J. Atmos. Oceanic Technol.*, **12**, 800–820.

Velden, C., et al., 2005: Recent innovations in deriving tropospheric winds from meteorological satellites. *Bulletin of the American Meteorological Society*, **86 (2)**, 205–223.

Velden, C. S., 1996: Winds derived from geostationary satellite moisture channel observations: Applications and impact on numerical weather prediction. *Meteorology and Atmospheric Physics*, **60**, 37–46.

Velden, C. S., C. M. Hayden, S. J. Nieman, W. P. Menzel, S. Wanzong, and J. S. Goerss, 1997: Upper-tropospheric winds derived from geostationary satellite water vapor observations. *Bulletin of the American Meteorological Society*, **78 (2)**, 173–195.

Wang, Y. and G. J. Holland, 1996: Tropical cyclone motion and evolution in vertical shear. *J. Atmos. Sci.*, **53**, 3313–3352.

WMO, 2005: Standard terminology. http://severe.worldweather.wmo.int/tc/cgn/acronyms.html#GTC.

Yuter, S. E. and R. A. Houze, 1995: Three-dimensional kinematic and microphysical evolution of Florida Cumulonimbus. Part II: Frequency distributions of vertical velocity, reflectivity, and differential reflectivity. *Mon. Wea. Rev.*, **123**, 1941–1963.

Acknowledgments

To my advisor, Prof. Dr. Sarah Jones, many thanks for giving me the opportunity to work on this interesting topic and for the supervision. In particular, I want to thank you for giving me the chance to work at NPS for two month and for establishing the contacts to the many people that contributed to this thesis.
To Prof. K. D. Beheng, thanks for patiently answering all questions about microphysics and for reviewing this thesis.
To Prof. Pat Harr, thank you for the invitation to NPS, for the supervision, the help with the interpretation, and the great stay in general.
To Dr. Michael Bell, sincerest thanks for the guidance through the process of getting from raw radar data to a sensible 3D analysis. Thanks for your assistance, ranging from the everyday help of e.g. finding missing withspaces in the command line up to the interpretation of the results and proofreading parts of the thesis.
To Dr. Chris Davis, thanks for the helpful discussions and suggestions.
To Bob and Dick, thanks for making the stay at NPS so wonderful.
To the Helmholtz Association, for funding the visit of NPS under the Helmholtz ATMO Program.
To the members of my research group, thanks for answering my many questions and for the assistance with data supply and coding problems.
To Julian, many thanks for the countless fruitful discussions, the many lines of shared code and the great time in and around Monterey.
To all the others in the "Diplomandenraum", namely Marie, Janina, Petra, Joris, Gerrit, Andrea and Sanni, thanks for making everyday life so enjoyable.
To Flo, thanks for proofreading parts of this thesis and for the recreating coffee breaks.
To my family, thanks for supporting me in every way.
To Michi, thanks for motivating and supporting me every day.

Erklärung

Hiermit erkläre ich, dass ich die vorliegende Arbeit selbstständig verfasst und keine anderen als die angegebenen Quellen und Hilfsmittel verwendet habe.

Ich bin damit einverstanden, dass die Arbeit in die Bibliothek eingestellt wird.

Karlsruhe, den 17. Oktober 2011

Annette Förster